Single spin magnetometry with nitrogen-vacancy centers in diamond

Single spin magnetometry with nitrogen-vacancy centers in diamond

A thesis presented

by

Nicholas Edward Kennedy Chisholm

to

The School of Engineering and Applied Sciences

in partial fulfillment of the requirements

for the degree of

Doctor of Philosophy

in the subject of

Applied Physics

Harvard University

Cambridge, Massachusetts

April 2015

Thesis advisor

Mikhail D. Lukin

Author

Nicholas Edward Kennedy Chisholm

Single spin magnetometry with nitrogen-vacancy centers in diamond

Abstract

The nitrogen-vacancy (NV) center in diamond is a solid-state point defect with an electronic spin that has accessible quantum mechanical properties. At room temperature, the electronic ground state sub-levels of the NV center can be initialized and read out using optical pumping, as well as coherently controlled using microwave frequency fields. This thesis focuses on using the spin state of the NV center for highly-sensitive magnetometry under ambient conditions. In particular, when the diamond surface is properly prepared, we demonstrate that NV centers can be used to measure the magnetic fluctuations stemming from individual molecules and ions attached or adsorbed to the surface.

This thesis begins by introducing the physical and electronic structure of the NV center at room temperature, followed by the fundamental measurements that allow us to use the NV center as a sensitive magnetometer. Combining our sensitive NV center magnetometer with techniques from chemistry and atomic force microscopy (AFM), we demonstrate the all-optical detection of a single-molecule electron spin at room temperature. Finally, we discuss the time-resolved detection of individual electron spins adsorbing onto the surface of nano-diamonds. By extending our techniques to nano-diamonds, we move closer towards *in vitro* magnetic field sensing that could be

pivotal for better disease diagnosis and drug development.

Contents

Title Page i
Abstract iii
Table of Contents v
Table of Contents v
Citations to previously published work viii
Acknowledgments ix
Dedication xiv

1 Introduction **1**
1.1 Background 1
1.2 Overview of thesis 4
1.2.1 Room temperature structure and properties of the NV center . 5
1.2.2 All-optical sensing of a single-molecule electron spin 5
1.2.3 Time-resolved single electron spin detection with nano-diamonds in solution 6

2 Structure and properties of the NV center **7**
2.1 Introduction 7
2.2 Structure of the NV center 8
2.2.1 Physical structure 8
2.2.2 Electronic structure 9
2.3 Experimental methods 10
2.3.1 Diamond samples 10
2.3.2 Experimental setup 11
2.3.3 Electronic spin ground state readout and manipulation 13
2.4 Conclusion 17

3 All-optical sensing of a single-molecule electron spin **19**
3.1 Introduction 19
3.2 Measurement setup and sample preparation 21
3.3 Co-localization of a single shallow NV center and a Gd^{3+} molecule . . 22

3.4 Measurement of magnetic noise from a single Gd^{3+} molecule attached to a diamond surface using a single shallow NV center 25
3.5 Magnetic noise measurements in the single Gd^{3+} molecule sensing regime 27
3.6 Conclusions and outlook 30

4 Time-resolved detection of single electronic spins in solution 32
4.1 Introduction 32
4.2 Measurement of magnetic noise from Gd^{3+} ions attached to the nano-diamond surface 33
4.3 Time-resolved sensing of the adsorption of single Gd^{3+} ions onto the nano-diamond surface 37
4.4 Conclusions and outlook 39

5 Conclusions and outlook 40

A Supporting material for Chapter 3 45
A.1 Materials and methods 45
A.1.1 Diamond samples 45
A.1.2 Optical setup 46
A.2 Sample preparation 47
A.2.1 Diamond surface cleaning procedure 47
A.2.2 Gd^{3+}-molecule attachment procedure 47
A.2.3 Gd^{3+}-molecule removal procedure 48
A.3 Determination of Gd^{3+}-molecule surface density 48
A.3.1 Atomic force microscopy 48
A.4 Co-localization procedure 51
A.4.1 AFM drift correction 51
A.4.2 Co-localization steps 52
A.4.3 Co-localization uncertainty 52
A.5 Derivation of $\Gamma_{induced}$ 53
A.6 Co-localization simulation 57
A.7 Detecting Gd^{3+}-molecules by measuring NV center relaxation 58
A.7.1 Range of parameters consistent with experimental data 58
A.7.2 Experimental data uncertainty analysis 60
A.7.3 Photon shot noise-limited detection sensitivity 60
A.8 Control experiments with La^{3+} containing molecules and bare ligand molecules 61

B Supporting material for Chapter 4 63
B.1 Materials and Methods 63
B.1.1 Nano-diamond samples 63
B.1.2 Optical setup 65

B.1.3 Microwave setup . . . 66
B.1.4 Coplanar waveguide fabrication . . . 66
B.1.5 Distinguishing single NV centers . . . 67
B.1.6 $GdCl_3$ and $LaCl_3$ solutions . . . 68
B.2 Additional Single Gd^{3+} Detection Result . . . 69

C Magnetic resonance detection of individual proton spins using quantum reporters 70
C.1 Introduction . . . 70
C.2 Characterization of the surface quantum reporter spin network . . . 71
C.3 Coherent control and dynamics of the reporter spins . . . 74
C.4 Detection of the magnetic field created by protons using reporter spins 76
C.5 Coherent dynamics between individual reporter and proton spins . . . 77
C.6 Conclusions and outlook . . . 81

D Supporting material for Appendix C 84
D.1 Materials and measurement apparatus . . . 84
D.1.1 Diamond sample . . . 84
D.1.2 Optical setup . . . 85
D.1.3 RF setup . . . 86
D.2 NV centers and depth measurements . . . 86
D.3 Localizing reporter spins on the diamond surface . . . 88
D.3.1 The double electron-electron resonance experiment . . . 88
D.3.2 Localizing the reporter spins with DEER at several magnetic field directions . . . 89
D.3.3 Limits on the separation between surface reporter spins from their population relaxation . . . 92
D.4 The reporter pulse sequence . . . 93
D.5 Sensing nuclear spins using the reporter echo sequence . . . 95
D.5.1 Semiclassical spin bath . . . 95
D.5.2 Coherent hyperfine coupling to individual nuclear spins . . . 96
D.5.3 Fitting experimental data . . . 97
D.6 Control experiment: acid-cleaning the diamond surface . . . 99

Bibliography 101

Citations to previously published work

Parts of Chapter 2 have been prepared for publication as:

> "Time-resolved detection of single electronic spins in solution," N. Chisholm, I. Lovchinsky, A. O. Sushkov, H. Park, and M. D. Lukin, in preparation (2015).

Chapter 3 and Appendix A, in their entirety, have been published as:

> "All-optical sensing of a single-molecule electron spin", A. O. Sushkov*, N. Chisholm*, I. Lovchinsky*, M. Kubo, P. K. Lo, S. D. Bennett, D. Hunger, A. Akimov, R. L. Walsworth, H. Park, and M. D. Lukin, Nano Letters **14**, 6443-6448 (2014).

Chapter 4 and Appendix B, in their entirety, are being prepared for publication as:

> "Time-resolved detection of single electronic spins in solution," N. Chisholm, I. Lovchinsky, A. O. Sushkov, H. Park, and M. D. Lukin, in preparation (2015).

Appendix C and D, in their entirety, have been published as:

> "Magnetic resonance detection of individual proton spins using a quantum reporter network," A. O. Sushkov, I. Lovchinsky, N. Chisholm, R. L. Walsworth, H. Park, and M. D. Lukin, Physical Review Letters **113**, 197601 (2014).

* These authors contributed equally to this work.

Acknowledgments

First and foremost, I would like to thank my research advisor, Prof. Mikhail Lukin. Ever since the first day I walked into his office, Misha has always shown confidence in my abilities as a scientist and compassion for me as a person. When I decided I wanted my career to take a different path, in particular towards more biologically and medically relevant research, he not only enabled and encouraged me to explore my interests, but also came up with innovative and courageous ideas to help me fulfill my goals. I cannot thank Misha enough for all of his support in my career.

I would also like to thank my other dissertation committee members: Profs. Marko Ločar and Amir Yacoby. Prof. Marko Lončar was kind enough to be my SEAS co-advisor so that I could work with Misha, and also has been supportive in all of my pursuits. Prof. Amir Yacoby was kind enough to agree to be on my committee last-minute, and for that I am very appreciative, along with the knowledge that I have exchanged with his exceptional group over the past six years.

Prof. Hongkun Park has been a wonderful collaborator and certainly provided pivotal ideas to our research. We really would not have progressed far without his constant insights. His support during the toughest parts of my Ph.D. research was very encouraging.

Igor Lovchinsky has been my better half in the lab since May 2011, and I honestly could not have asked for a better work husband. Our complementary approaches to science made it exciting to come to lab and work with him. Outside of the lab, Igor has been one of my best friends at Harvard, even asking me (despite my advice) to sing at his “wallaby" (also known as a wedding to the rest of the world). I was

truly lucky to meet and work with such a great physicist and person. Oh, and many thanks for always editing and revising my writing, be it for papers or this thesis.

Yiwen Chu, another member of the Lukin group, has been a constant supporter and ally of mine. I am really unsure I would have stayed sane without our lunches and dinners. I am still in awe of Yiwen's work ethic and ability to maintain composure under the toughest of circumstances. I am very grateful to have been able to call you a colleague, and I will always call you a friend.

I have been very fortunate to have exceptional mentors during my time in academia thus far. Prof. Reza Nejat taught my first and last physics class at McMaster University, and has been a constant mentor and friend. Prof. Duncan O'Dell provided me with the opportunity to complete an undergraduate thesis, and in the process, helped engage me in physics in a way I never thought I would: theoretically. Prof. Aephraim Steinberg provided me with a rich and diverse exposure to experimental physics, and to Toronto in general. It was an absolute pleasure to work in his group for two summers, and those summers ultimately persuaded me to pursue my Ph.D. Prof. Brian King was always an avid supporter and took time out of his own life to mentor me, for which I am forever grateful. He truly gave me my first exposure to experimental physics.

I would also like to acknowledge the following scientists for their great contributions to my scientific, and in some cases, personal life: Alexey Akimov, Steve Bennett, Eric Bersin, Prof. Ignacio Cirac, Faiyaz Hasan, Prof. Ed Hinds, David Hunger, Liang Jiang, Georg Kucsko, Minako Kubo, Christian Latta, Ian Linington, Peggy Lo, Peter Maurer, Matthew Markham, Nick Miladinovic, Fernando Pastawski, Alex Sushkov,

Daniel Twitchen, and Prof. Ron Walsworth. Of course, I would like to thank the Lukin, Park, and Yacoby groups in general for great discussions and collaborations.

I have been extremely fortunate to be a resident tutor at Lowell House since July 2012, providing me with both a house and a community that I have been proud to call home for the past three years. The acknowledgements have to begin with the blocking group that kindly adopted me as one of their own: Dan Dou, Matthew Harvey, Karl Krehbiel (and of course his amazing wife, Carolyn Krehbiel), Richard Lopez, Bryan Padilla, and David Tang-Quan. I never thought my students (or, as I affectionally call them, my "children") would have such a profound influence on me and my life. You seven have constantly challenged my views on life, and provided me with love and support that truly leaves me dumbfounded. I am so very proud to call you my friends, and I can't wait to see how you change the world in the future. It goes without saying that I must thank House Masters Diana Eck and Dorothy Austin for hiring, and thus taking a chance on, me. I hope that I have met your expectations over the past three years, having (hopefully) permeated throughout the House the same love and support you have provided me. Resident Dean Caitlin Casey has been more supportive than any supervisor ever needs to be. I have been overwhelmed by her constant support and encouragement. I'm thrilled to call both her and her husband, Daniel Peterson, my friends. Thanks to Haley Mendez for teaching me how to play squash. A special thanks to Michael Slovenski and George Mills for featuring me in their band, allowing me to live out my dream of being a rock star (if only for a few songs). There have been a myriad of college students that have provided unwavering support and encouragement during the course of my Ph.D., too many to

mention here. Special thanks, however, must go to Gillian Farrell, Michael Landry, Marina Lehner, Nicholas Rinehart, Ariana Saxby, and Chris Stock. Of course, many thanks to the men I had the privilege of singing with in the Harvard Glee Club and playing baseball with on the Harvard Club Baseball team.

I am lucky enough to say that I have two best friends: Ryan Lum-Tai (whom I met in high school) and Martin Muñoz (whom I met during my time at McMaster University). Ryan has been with me through thick and thin, and I'm so lucky to be able to say that I have grown up with such an amazing person. To have someone to turn to during those high school years that were so very difficult was priceless. At the same time, our competitive streaks helped me improve as a saxophonist and student in a way that I think made it possible for me to even get into college. But let's be honest: I'm only really saying all this because I want free dental care once he graduates. Martin was my math half when we were both math and physics majors at McMaster. I don't think I ever told you, but after we graduated, I was told that people were jealous of us. Perhaps they meant they were jealous of our collaboration on problem sets, but I think they were just jealous of our love (too bad Lara got in the way). College would have been an absolute bore without Martin's constant wit and, quite frankly, genius. I hope you both realize that I am unbelievably proud to call you my friends, and that I love you both more than I could ever admit.

My late grandmother, Thelma Kennedy, had one of the greatest impacts on my life. Aside from moving in and helping take care of our family (namely cooking and being a laundry goddess), she was a source of inspiration and support that I never fully appreciated. Weeks after she passed away following a 40-year battle with

cancer(s), I was diagnosed with cancer. Her brave and unwavering fight against her multiple diagnoses provided with me with a source of inspiration against my fight. She was also probably the only person in my life that has ever completely trusted me with everything I did. Frequently in moments of weakness I think back to things she said or did when she was alive, and I realize that I am still learning from her to this day.

My brother, Benjamin Chisholm, probably has no idea how much our relationship means to me. I know that when I really need him, my big brother will always be there for me. We're even beginning to agree on most things to do with baseball. My late sister, Molly Chisholm, was more than just a pet: the puppy that never grew up was a meaningful part of our family. I can safely say there wasn't another creature, human or otherwise, more excited to see or hug me when I visited home.

I am forever indebted to my parents, Michael Chisholm and Linda Kennedy, for all of the love, encouragement, and support they have provided me throughout my life. They put up with me in their home for the first 21 years of my life, always supporting me and quite honestly going completely out of their way to make sure I was happy. More defining than that, though, was the example they each set for me. My father constantly supported all of my goals, realistic or not, and also showed me the power of hard work and determination in all aspects of life. My mother is my life raft: I honestly don't think I would have survived my Ph.D. without her love and unwavering support. She taught me that integrity and being a good person are more important than anything else.

To my parents

Chapter 1

Introduction

1.1 Background

Over the past century, quantum mechanics has led a technological revolution that has dramatically altered the way we interact with the world. For example, the laser has had applications in optical disk drives [1], optical communication [2], cutting [3] and welding [4], surgery [5–7], and even quantum mechanics research itself [8, 9], to name just a few. Magnetic resonance imaging (commonly referred to as MRI) has had tremendous impacts in healthcare, completely changing the way we treat and diagnose patients [10]. The transistor has become the fundamental building block for modern electronics, shaping the way we work and connect with each other [11]. There are ongoing efforts to continue this unprecedented advance in modern technology, where quantum communication offers the promise of perfectly secure communication [12], quantum computing offers the potential for exponential speed-up for solving some important problems [13], and quantum metrology could

offer increased sensitivity for physical and biomedical applications [14]. Despite all of these remarkable achievements and goals, there remain important challenges that physicists must overcome to continue to push the boundaries of quantum mechanics' role in our everyday lives.

One of the key challenges of applying fundamental knowledge to important problems is being able to fully understand and control the system one is working with. In order for quantum mechanics to be useful for the applications described above, there must be a way to control the quantum mechanical state of the system being used. This, of course, requires controlled interaction with the external environment. Despite the necessity of interaction with the external environment, there also is the requirement of maintaining quantum states. This, paradoxically, requires that the quantum state be well-isolated from the noise often stemming from interactions with the environment. Therein lies the key requirement for quantum technology: the ability to strongly couple to control fields while at the same time maintaining isolation from uncontrolled sources of noise in the external environment.

There have been dramatic advances towards this goal. Neutral atoms and ions have been cooled and trapped using magneto-optical traps, unlocking their quantum mechanical properties [15, 16]. They have been coherently manipulated and probed with light in order to perform quantum gate operations, one of the necessary building blocks of quantum computing [17]. Moreover, the trapped ion community has made significant progress towards scaling up these technologies while still maintaining isolation from external noise [18, 19]. In the field of quantum communication, entangled photons have proved to be very useful due to their ability to propagate freely over

long distances without loss of information, while using the measurement process to effectively distribute information [20]. Magnetic resonance force microscopy offered the first single electron spin detection [21,22], while other systems including superconducting quantum interference devices [23], the Hall effect in semiconductors [24], and spin-exchange relaxation-free atomic magnetometers [25] have also shown incredible magnetic sensitivity. All of these examples have required a deep understanding of the system being manipulated and probed, while at the same time minimizing noise from the environment.

More recently, there has been tremendous interest in a solid-state defect that provides the advantages of quantum mechanics while being able to operate under ambient conditions: the nitrogen-vacancy (NV) center in diamond, a point defect [26]. One of the key advantages of NV centers is their isolation from an unpredictable external environment via the diamond lattice. This allows for the maintenance of their quantum mechanical properties without the need for cooling, and their location is fixed, thus eliminating the need for trapping. Despite operating in ambient conditions, the NV center has been demonstrated or proposed to have great promise as a quantum mechanical resource, for example in quantum computing [27–29], quantum cryptography [30], quantum memory [31], clocks [32], electrometry [33], thermometry [34, 35], etc. It is important to note that other solid-state systems offer similar advantages, such as superconducting qubits (though these need to be cooled) [36–38] and quantum dots [39–41].

In this thesis, we discuss applications of the NV center in diamond to magnetometry. One of the biggest obstacles to performing precision magnetic field measure-

ments using NV centers is bringing the sample to be measured close enough to the surface of the diamond (or vice versa) so that the NV center can interact with the magnetic field of the sample being observed, while still maintaining its key properties. This again goes back to the main challenge of integrating quantum technologies: we must find a way to have the NV center interact with the environment in a manner that we can control such that noise does not negatively affect its magnetometry capabilities.

Due to its exceptionally small volume and ability to operate under ambient conditions, the NV center has the potential to unlock magnetometry applications unapproachable by any other state-of-the-art magnetometer. This explains the reasoning behind the great excitement about the potential of NV centers for a range of applications not only in magnetometry, but in all applications that benefit from harnessing the tools that quantum mechanics provides.

1.2 Overview of thesis

This thesis focuses on room temperature magnetometry using NV centers and is organized as follows. In Chapter 2, we introduce the room temperature structure and properties of the NV center. To this end, we develop the framework required to understand the experimental projects discussed in the rest of this thesis. Chapter 3 and Appendix A demonstrate the all-optical sensing of a single-molecule electron spin covalently attached to a bulk diamond surface. In Chapter 4 and Appendix B, we use NV centers in nano-diamonds to perform time-resolved sensing of single electron spins in solution, paving the way for *in vitro* biomedical applications. Finally, we conclude

with a discussion of the remaining challenges and future outlook for magnetometry using NV centers in diamond.

1.2.1 Room temperature structure and properties of the NV center

We begin with a description of the system that we use as our nanoscale magnetometer: the nitrogen-vacancy (NV) center in diamond at room temperature. In particular, Chapter 2 begins by discussing the physical and electronic structure of the NV center. We briefly discuss the diamond samples used in our experiments, as well as the experimental setup used to manipulate the electronic spin ground state of the NV center. Finally, we demonstrate our ability to read out and manipulate the electronic spin ground state of the NV center, exhibiting our ability to control our quantum system. Given its unique electronic ground state structure at room temperature, in particular its ability to be manipulated as an isolated spin qubit, it is evident that one can use the NV center as a sensitive magnetometer.

1.2.2 All-optical sensing of a single-molecule electron spin

In Chapter 3, we demonstrate that a single-molecule electron spin located outside the diamond substrate can be detected with nanometer precision. In particular, we use a single, isolated NV center in bulk diamond to measure single Gd^{3+} ligand molecules that are covalently attached to the diamond surface. We confirm the presence of a single Gd^{3+} molecule through the use of atomic force microscopy (AFM). The magnetic detection of the single spin is achieved by sensing the magnetic noise

created by the fast relaxation time of the Gd^{3+} molecules, which in turn causes the electronic ground state of the NV center to relax at a faster rate. This demonstrates the ability of NV centers in diamond to measure single electron spins outside the diamond substrate, thus bringing us closer to realizing the detection of single spins in biological systems.

1.2.3 Time-resolved single electron spin detection with nano-diamonds in solution

To be useful for *in vitro* biomedical applications, however, our sensor must be able detect electronic spins in solution within a cell. In Chapter 4, we extend NV magnetometry to time-resolved sensing of single electronic spins at room temperature using nano-diamonds. We immerse carefully prepared NV-containing nano-diamonds in different solutions of $GdCl_3$ to demonstrate their ability to sense Gd^{3+} ions, sensing the effect their magnetic noise has on the relaxation rate of the NV centers. In particular, we notice the Gd^{3+} ions adsorb onto the nano-diamond surface, and that the adsorption rate is strongly dependent on $GdCl_3$ concentration. By measuring the relaxation rate of the NV centers at one specific delay time as opposed to measuring the full relaxation curve, we are able to detect discrete steps in the NV center relaxation rate that correspond to individual Gd^{3+} ions attaching to the diamond surface. This work paves the way for *in vitro* magnetic field detection with potential applications such as disease detection and drug development.

Chapter 2

Structure and properties of the NV center

2.1 Introduction

In this Chapter, we begin with a brief discussion of the physical and electronic structure of the NV center. We then discuss a method by which we can create NV centers in diamond, in particular for the magnetometry applications discussed in this thesis. Finally, we introduce the experimental methods which we use to image and manipulate the electronic ground state of NV centers in diamond. These methods provide the foundation on which the experiments described in the rest of this thesis are built.

2.2 Structure of the NV center

2.2.1 Physical structure

The NV center is a point defect in diamond. In particular, it consists of one carbon atom in the lattice replaced by one nitrogen atom, and a missing carbon atom (a vacancy) in one of the four neighboring lattice sites (see Fig. 2.1A). The NV center exhibits C_{3v} symmetry about the nitrogen-vacancy axis, which is important in determining its electronic structure.

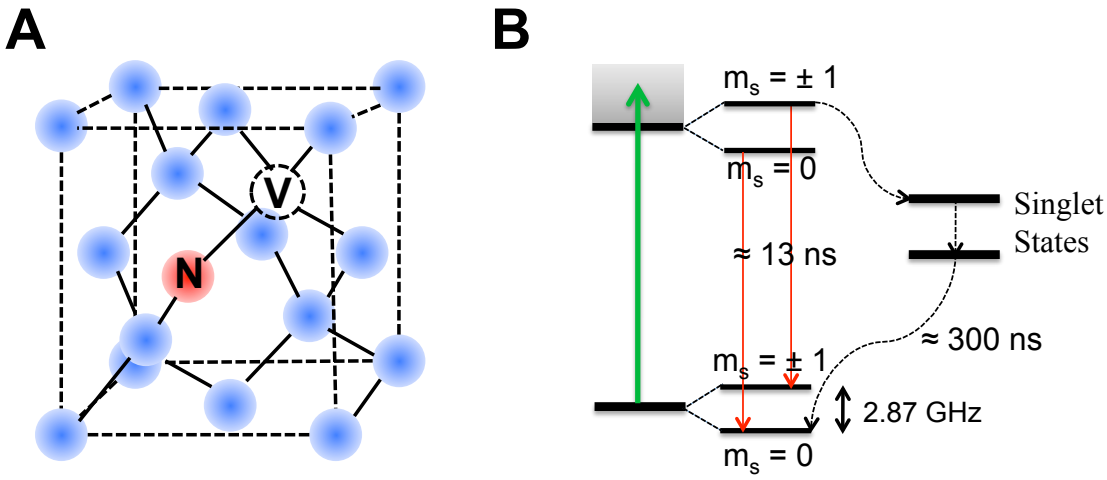

Figure 2.1: Physical and electronic structure of the NV center. (A) Physical structure of the NV center. Dashed lines represent a cube, while solid lines depict covalent bonds. Blue spheres represent carbon, the red sphere (labeled N) represents nitrogen, and the hollow sphere with dashed outline (labeled V) represents a vacancy. (B) Electronic structure of the NV center. $|g\rangle$ represents the electronic ground state and $|e\rangle$ represents the excited state. Solid lines are radiative transitions, whereas dashed lines are non-radiative transitions. The solid green line represents the optical pumping beam, which typically is a green laser beam.

2.2.2 Electronic structure

The C_{3v} symmetry of the NV center gives rise to the NV center's electronic structure (see Fig. 2.1B). The electronic spin associated with the NV center comes from the lone electron pair of the nitrogen atom, along with the dangling bonds of the three carbon atoms adjacent to the vacancy [42]. In the case of NV^-, which is what we typically call an NV center (and this is the convention we use throughout this thesis), there is an additional electron spin that comes from the diamond lattice (possibly from a nearby substitutional nitrogen) [42]. This gives a total of 6 electron spins. The electronic spin ground state energy levels can be calculated using density function theory [43]. In particular, the NV center has an electronic ground state triplet, $|g\rangle$, that splits into $m_s = 0$ and $m_s = \pm 1$ sub-levels. At zero magnetic field, the $m_s = 0$ sub-level is split from the $m_s = \pm 1$ sub-levels by approximately 2.88 GHz, which is caused by a dipole-dipole interaction in the $m_s = \pm 1$ states due to a lack of inversion symmetry in the electron density of these states [42, 44]. The electronic excited state, $|e\rangle$, has a radiative lifetime of approximately 13 ns and a zero-phonon line (ZPL) at 637 nm [45]. At room temperature, vibronic bands exist in the electronic ground and excited states that allow for higher (lower) frequency in absorption (emission) [26, 46]. There is a significantly higher chance of the $m_s = \pm 1$ excited state, compared to the $m_s = 0$ sub-level, to decay along the non-radiative path through the singlet states [26]. For simplicity, we can assume that only the $m_s = \pm 1$ sub-levels enter the non-radiative path. This non-radiative path through singlet states, often referred to as an intersystem crossing, takes approximately 300 ns to non-radiatively decay back to the electronic ground state [26, 47]. The radiative

decay is mostly spin-preserving, whereas the non-radiative decay is not [26]. For the NV center community's current description of the electronic structure, see [26].

2.3 Experimental methods

2.3.1 Diamond samples

NV centers are naturally occurring defects in diamond. However, in order for these defects to be useful for magnetometry applications, we need the diamond to be free of unwanted defects (ex. anything other than ^{12}C atoms) and have NV centers located close to the diamond surface. To ensure the diamond is pure, it can be created by chemical vapor deposition [48]. To create NV centers close to the diamond surface, ion implantation can be performed [49]. In this approach, nitrogen atoms bombard the diamond lattice and create vacancies [49]. By implanting the nitrogen at a specific energy, we can make it so that the nitrogen ends-up within the first few nanometers of the surface. To find the correct energy, we use stopping range of ions in matter (SRIM) calculations [50]. By annealing the diamond above 800°C, some of the vacancies become mobile and reach a nitrogen to become a nitrogen-vacancy center [49,51]. This is possible because it is thermodynamically favorable for the vacancy to have nitrogen as one of its nearest neighbors. In this thesis, we use implanted bulk diamonds (Chapter 3 and Appendix C) as well as monocrystalline nano-diamonds (Chapter 4), the latter being small enough to only require the use of naturally occurring NV centers. More information about the diamond samples and how they were prepared for the experiments discussed in Chapters 3, 4, and Appendix

C can be found in Appendices A, B, and D, respectively.

2.3.2 Experimental setup

In order to probe NV centers in diamond, we use a scanning confocal microscope (see Fig. 2.2A). In particular, we first send a continuous-wave (CW) green (532 nm) laser through an acousto-optic modulator (AOM) in a double-pass configuration. By doing this, we create an ultrafast optical switch that we can use to make pulses of green light, as the AOM is switched on and off via TTL pulses from a computer. We couple the resulting green light into an optical fiber so that we can send it to the optical table that contains our setup. A collimated beam comes from the fiber coupler on the setup table and is sent through a scanning confocal microscope setup. The green probe light first reflects off a dichroic mirror (which reflects green light and transmits red light), then reflects off a galvanometer (controlled by a multifunction data acquisition (DAQ) device controlled by the computer) which is located one focal length away from the first of two lenses. Two focal lengths away is another lens, opposite of which there is an objective lens one focal length away. This optical path is designed so that as the galvanometer changes the angles of its mirrors (via voltage output from the DAQ) and the laser beam of light changes its path, the laser light will always reach the back of the microscope objective at the same point: the only thing that will change is the angle at which the light arrives. This allows us to scan an area of approximately 200 μm by 200 μm. The objective lens sits on a piezoelectric mount (controlled by the DAQ) that moves the objective up and down vertically by 100 μm. In the end, our scanning confocal microscope has a field of vision of 200 μm

by 200 μm by 100 μm. The NV center emits above 637 nm, therefore the fluorescence is collected by traversing the optical path in reverse and passing through the dichroic mirror that first reflected the green probe beam. This light is passed through a 637 nm long-pass filter and 532 nm notch filter, then coupled into an optical fiber, and collected by an avalanche photodetector (APD). The resulting counts are collected and sent to the DAQ, where the acquisition time windows are controlled using TTL pulses from the computer. We use an oil objective with a high numerical aperture specifically so that we can maximize our collection efficiency.

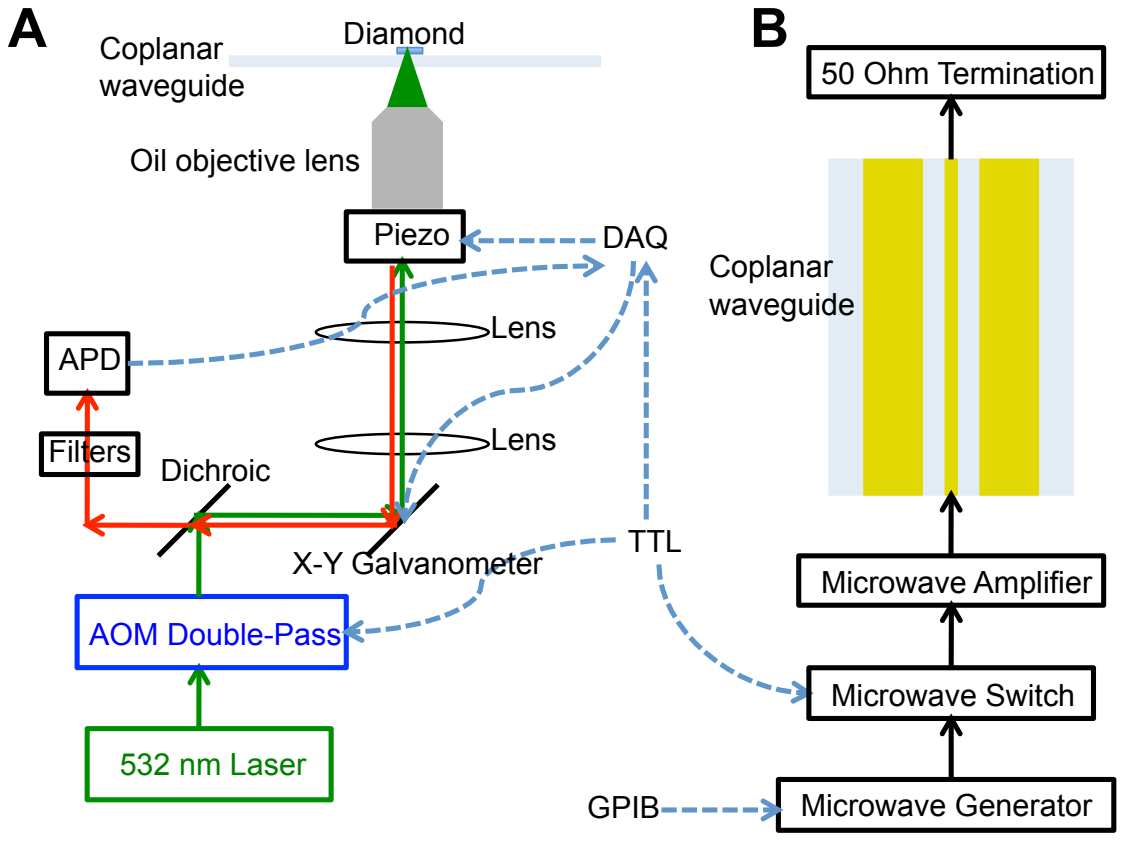

Figure 2.2: Experimental setup. (A) Scanning confocal microscope. (B) Microwave setup.

To coherently manipulate the electronic ground state of an NV center, we re-

quire the use of microwave-frequency fields (see Fig. 2.2B). We send the output of a microwave generator (controlled by GPIB from the computer) through a microwave switch. The switch, controlled by TTL pulses from the computer, allows us to make microwave pulses of different durations that are delivered to the diamond sample. After the switch, the microwaves are sent through an amplifier and then passed through a coplanar waveguide that has been fabricated onto a coverslip using optical lithography. This coplanar waveguide sits above the microscope objective of the confocal microscope. The diamond sample to be observed sits on top of the coplanar waveguide, with the side that contains the NV centers closest to the microscope objective. This allows the gap between the coverslip and the NV centers to be small enough such that we can use an oil objective lens.

More specific details about the optical and microwave setups used in the experiments discussed in Chapters 3, 4, and Appendix C can be found in Appendices A, B, and D, respectively.

2.3.3 Electronic spin ground state readout and manipulation

Now that we have established the physical and electronic structure of the NV center, along with the experimental setup that is used for our experiments, we can discuss how we manipulate and read out the electronic spin ground state of the NV center. At room temperature (i.e. in thermal equilibrium), the electronic spin of the NV center equally populates the three sub-levels associated with its electronic ground state. We can optically pump the electronic spin into the excited state using green light, which is a spin-conserving process [52, 53]. Electronic spin population

that was originally in the $m_s = 0$ sub-level predominately radiatively decays back into the $m_s = 0$ electronic ground state at the decay rate of 13 ns and emission at a wavelength greater than 637 nm. The $m_s = \pm 1$ sub-levels can also radiatively decay back to the $m_s = \pm 1$ electronic ground state sub-levels they originally populated, but a significant portion of the population also decays via the non-radiative intersystem crossing previously discussed [54]. When the spin decays out of the singlet states, it predominately decays into the $m_s = 0$ sub-level [54], thus polarizing the NV center [52, 53] (in practice, pulse lengths of 1 μs are typically used for polarization). The fact that the $m_s = 0$ and $m_s = \pm 1$ sub-levels have different fluorescence rates allows for fluorescent detection of the spin state [52, 53]. Of course, because polarization occurs, there is an optimal fluorescence detection time which has been found to be approximately 300 ns [47]. Thus, we have a method of optical polarization and fluorescent readout of our NV center spin ground state.

Now that we have a method of both polarizing and reading out the electronic ground state of the NV center, we can perform optically-detected magnetic resonance (ODMR) measurements [55]. To do this, we polarize the NV center, apply a microwave pulse of fixed duration, then read out the NV center's state (pulse sequence shown in the inset of Fig. 2.3A). By sweeping over the microwave frequency, we can determine the ODMR spectrum of the NV center (see Fig. 2.3A). By applying a small magnetic field, it is possible to see the Zeeman effect split the $m_s = \pm 1$ sub-levels. Finding the ODMR at low microwave power (to avoid power broadening) allows us to see the hyperfine structure associated with the electron-nitrogen coupling of the NV center. This can help determine whether an NV center is natural (^{14}N) or implanted

(^{15}N), which is important for magnetometry applications where we only want to use NV centers that are close to the diamond surface.

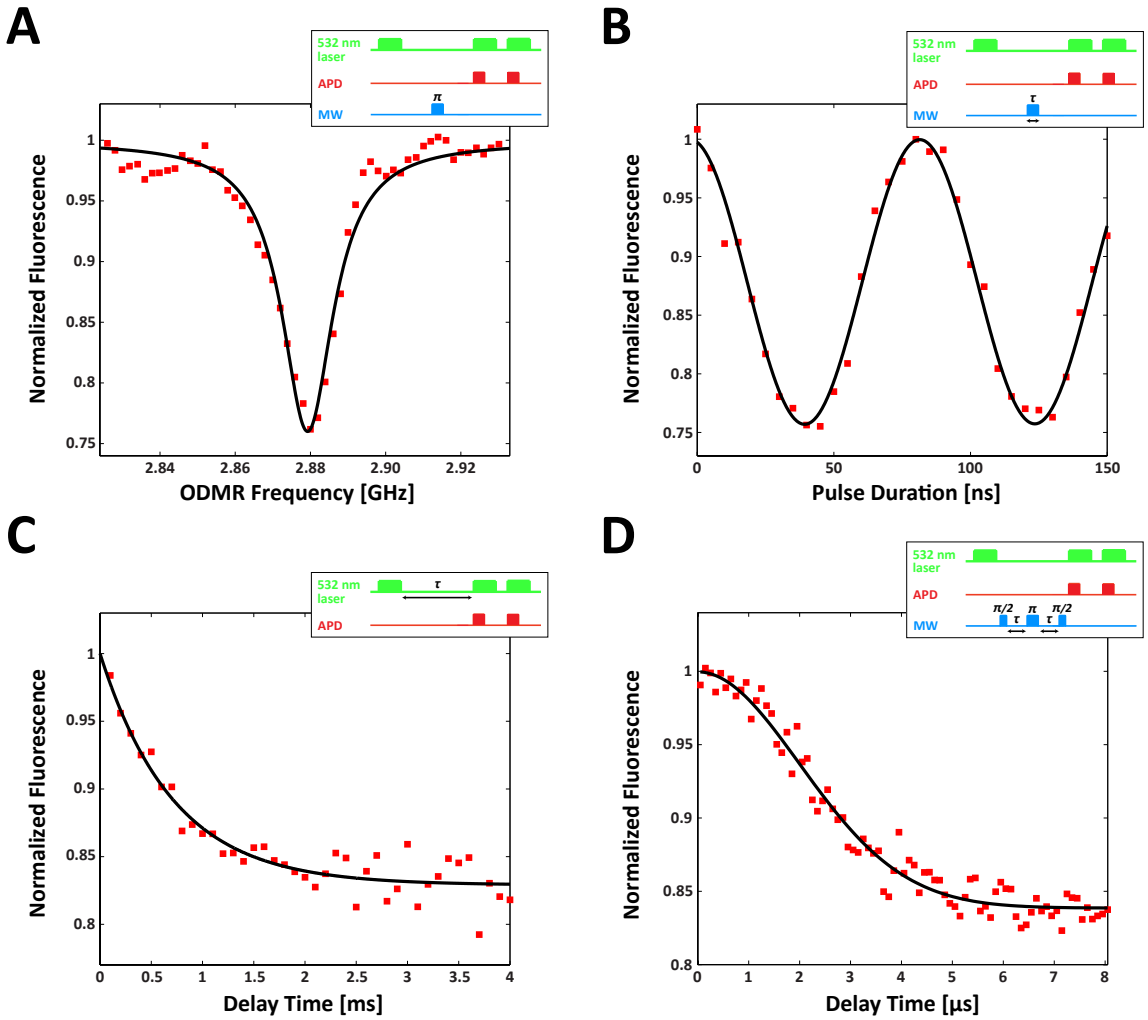

Figure 2.3: Electronic ground spin state manipulation. (A) Optically-detected magnetic resonance; inset: corresponding pulse sequence. (B) Rabi oscillations between the $m_s = 0$ and $m_s = -1$ sub-levels in the presence of an applied magnetic field; inset: corresponding pulse sequence. (C) T_1 measurement; inset: corresponding pulse sequence. (D) Spin echo measurement; inset: corresponding pulse sequence.

Given that we know the frequencies of the transitions between the $m_s = 0$ and $m_s = \pm 1$ sub-levels, and that the $m_s = \pm 1$ sub-levels can be separated by a magnetic field, we can perform Rabi oscillations [52]. To do this, we polarize the NV center, apply a microwave pulse at fixed frequency (corresponding to the transition frequency between the $m_s = 0$ and one of the $m_s = \pm 1$ sub-levels) but varying time duration, τ, and then read out the NV center's state (pulse sequence shown in the inset of Fig. 2.3B). This allows us to observe Rabi oscillations (see Fig. 2.3B), which demonstrates our ability to coherently manipulate the NV center's electronic ground spin state as we please.

One important measurement, in particular for the work done in Chapters 3 and 4, is the T_1 longitudinal relaxation time. To find the T_1 time, we polarize the NV center, wait for time τ, then read out the NV center's state (pulse sequence shown in the inset of Fig. 2.3C). This allows us to determine the population in the $m_s = 0$ sub-level at various times after polarization, and the fit to this curve gives us the T_1 time (see Fig.2.3C). Often, the relaxation rate ($1/T_1$) is reported instead of the T_1 since relaxation rates add linearly. The T_1 is the best resource at our disposal when trying to detect high-frequency magnetic noise, as discussed in Chapters 3 and 4. In principle, by changing the static magnetic field and thus the energy splitting of the electronic spin ground state sub-levels, we can map out the magnetic noise spectrum of the sample being observed.

Another important measurement, in particular for the work done in Appendix C, is the spin echo, which gives us the T_2 time (also known as the transverse relaxation time) [52]. To perform this measurement, we first apply a static magnetic field to

separate the $m_s = \pm 1$ sub-levels so that we have a spin qubit between $m_s = 0$ and one of the $m_s = \pm 1$ states. To find the T_2 time, we perform the following pulse sequence (as shown in the inset of Fig. 2.3D): we polarize the NV center, apply a $\pi/2$ microwave pulse, wait for time τ, apply a π refocusing microwave pulse, wait for time τ, apply a $\pi/2$ microwave pulse, then read out the state of the NV center. The refocusing π pulse allows us to cancel out the effect of static magnetic fields. With this pulse sequence, the NV population signal decays with the coherence time, T_2 (see Fig. 2.3D) [56]. When the refocusing pulse is not present, this is called a Ramsey experiment, and the resulting NV population signal decays with the electron spin dephasing time, T_2^* [56]. More details about these measurements, including complexities that arise from ^{13}C in the diamond lattice, can be found in [56]. Variations of spin echo measurements can be used to detect static and low-frequency magnetic fields created by electron and nuclear spins in the local environment, as demonstrated in Appendix C. It is important to note that the T_2 time can be further lengthened through the use of more complicated dynamical decoupling pulse sequences [57–60].

2.4 Conclusion

We began this Chapter discussing the physical and electronic structure of the NV center in diamond. We then discussed the diamond samples used throughout this thesis, and the creation of shallow NV centers in diamond. Capitalizing on the electronic structure of the NV center, we discussed our ability to manipulate the NV center by polarizing and reading out its electronic spin ground state. Finally, we demonstrated our ability manipulate the ground state sub-levels. This arms us with

the tools necessary for the experiments described in the rest of this thesis, namely in Chapters 3, 4, and Appendix C.

Chapter 3

All-optical sensing of a single-molecule electron spin

3.1 Introduction

Precision magnetic sensing is essential to a wide array of technologies such as magnetic resonance imaging (MRI), with important applications in both the physical and life sciences. In particular, in biology and medicine, functional magnetic resonance imaging (fMRI) has emerged as a primary workhorse for obtaining key physiological and pathological information noninvasively, such as blood and tissue oxygen level and redox status [10,61,62]. Developing nanoscale magnetic sensing applicable to individual molecules could enable revolutionary advances in the physical, biological, and medical sciences. Examples include determining the structure of single proteins and other biomolecules as well as *in vivo* measurements of small concentrations of reactive oxygen species that could lead to insights into cellular signaling, aging, mu-

tations, and death [63–66]. The practical realization of these ideas is extremely challenging, however, as it requires sensitive detection of weak magnetic fields associated with individual electronic or nuclear spins at nanometer scale resolution, often under ambient, room-temperature conditions. Many state-of-the-art magnetic sensors, including superconducting quantum interference devices (SQUIDs) [23], semiconductor Hall effect sensors [24], and spin exchange relaxation-free atomic magnetometers [25], offer outstanding sensitivity, but their macroscopic nature precludes individual spin sensing. Sensing ensembles of paramagnetic molecules in biological and medical systems is currently performed using bulk electron spin resonance (ESR), which has a limit of roughly 10^7 electron-spins [67]. Magnetic resonance force microscopy has been used to detect individual electronic spins, but at cryogenic, milliKelvin temperature [21, 22].

The nitrogen-vacancy (NV) center in diamond is a promising precision magnetic field sensor with nanoscale resolution [57, 68–70]. Ensembles of NV centers in bulk diamond have been used to sense paramagnetic molecules in solution [71], with sensitivity of $\sim 10^3$ statistically polarized spins and spatial resolution of approximately 450 nm; and NV centers in nanodiamonds have been used to sense paramagnetic ions covering the nanodiamond surface [72] and in a lipid bilayer formed around the nanodiamond surface [73]. Shallow NV centers have also been used to detect small ensembles of nuclear spins in samples covering the surface of a bulk diamond crystal [74, 75]. In this Chapter, we covalently attach target molecules to the diamond surface and demonstrate nanoscale localization and magnetic sensing of individual non-fluorescent paramagnetic molecules. This represents an important step towards

the development of nanoscale magnetic imaging of biomolecules under ambient conditions.

3.2 Measurement setup and sample preparation

In our approach, the target molecules are covalently attached to the diamond surface, and magnetic sensing of these molecules is performed under ambient conditions using a single shallow NV center as an all-optical nanoscale magnetometer (Fig. 3.1A). Importantly, the shallow NV center is close enough to the surface that it can detect the fluctuating magnetic field produced by the electronic spin of a single paramagnetic molecule, while maintaining good NV center spin coherence and optical properties. We apply this technique to detect a single paramagnetic molecule composed of a gadolinium ion (Gd^{3+}) chelated by an amine-terminated organic ligand (abbreviated as Gd^{3+} molecule below). Single-molecule sensing is confirmed by identifying NV centers that have only a single target molecule within the sensing area on the diamond surface.

Our scheme for covalently attaching molecules to the diamond surface relies on the coupling of the amine-functionalized Gd^{3+} molecule to the carboxylic group on the diamond surface: in order to improve this coupling efficiency, we activated the surface carboxylic group using a water-soluble mixture of 1-ethyl-3-(3-dimethylaminopropyl)-carbodiimide (EDC) and *N*-hydroxysulfosuccinimide (NHS) (Fig. 3.1B). This method yielded uniform surface coverage of molecules with little clumping (see Appendix A), and the surface density of molecules could be controlled by varying the concentration of the Gd^{3+} molecules during the reaction. This procedure can be used to cova-

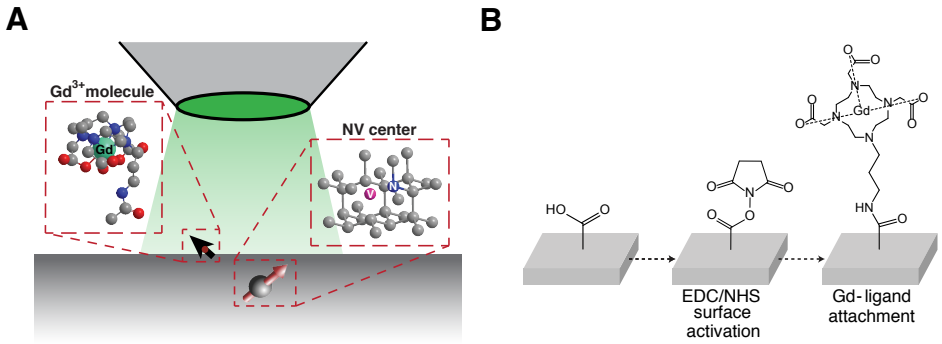

Figure 3.1: Schematic of measurement setup and sample preparation. (A) Single-molecule electron spin detection using a single shallow NV center in bulk diamond. Gd^{3+} molecules are attached to the surface of a bulk diamond crystal with widely separated NV centers located at a nominal depth of 6 nm below the diamond surface. NV center optical pumping and fluorescence detection is performed using a confocal microscope (objective shown). (B) Chemical procedure for attaching Gd^{3+} molecules to the diamond surface. EDC and NHS are used to activate carboxyl groups on the diamond surface so that they react readily with Gd^{3+} molecules functionalized with amine groups.

lently attach any water-soluble amine-terminated molecule to the diamond surface with controlled surface coverage. Since covalent attachment utilizes diamond surface carboxylic groups, the resulting molecular surface density was always less than a monolayer.

3.3 Co-localization of a single shallow NV center and a Gd^{3+} molecule

In our experiments, we used atomic force microscopy (AFM) to quantify the surface density of these molecules and to identify their proximity to a given shallow NV center. AFM measurements show that a clean diamond surface exhibits atomically-

smooth regions of typically a few square micrometers. When the Gd^{3+} molecules were attached, we observed circular features with mean height of 8 Å in the AFM scans. The heights, radii, and density of these features were consistent with single Gd^{3+} molecules covalently attached to the diamond surface (molecular dimensions were estimated from bond lengths and angles, see Appendix A). As an independent check of the surface molecule density, we added a single Cy3 dye molecule to each Gd^{3+} molecule and then attached the resulting molecule to the diamond surface using the same chemical procedure as before. We then performed surface fluorescence measurements to deduce the Cy3 surface density and compared the result to the density of the surface molecules measured using AFM. The results of these independent measurements were consistent with each other, providing strong evidence that the 8 Å-high AFM features are indeed single molecules (see Appendix A).

In order to determine the proximity of Gd^{3+} molecules to a given shallow NV center with nanoscale precision, we performed a three-step co-localization experiment (Fig. 3.2). First, we coated the diamond surface (via electrostatic attachment) with 100 nm diameter gold nanoparticles that fluoresce in the same spectral region as the NV centers and are optically resolvable individually. Second, we performed a fluorescence scan to determine the locations of individual NV centers and gold nanoparticles optically (Fig. 3.2A). Finally, we performed AFM topography measurements to determine the locations of gold nanoparticles and Gd^{3+} molecules (Fig. 3.2B). Because the nanoparticles appear in both optical and AFM images, we can use the locations of nanoparticles to combine the fluorescence and AFM measurements and deduce the lateral positions of Gd^{3+} molecules relative to an NV center with uncertainty of

approximately 15 nm (see Appendix A). Figure 3.2C shows an example of this co-localization experiment: an AFM image of Gd^{3+} molecules together with the position of a single shallow NV center, marked by a cross (the circle shows the NV center position uncertainty at one standard deviation). When the Gd^{3+} molecules were removed from the diamond surface, the AFM scan of the same region showed the absence of 8 Å-high features, confirming the successful removal of molecules (Fig. 3.2D).

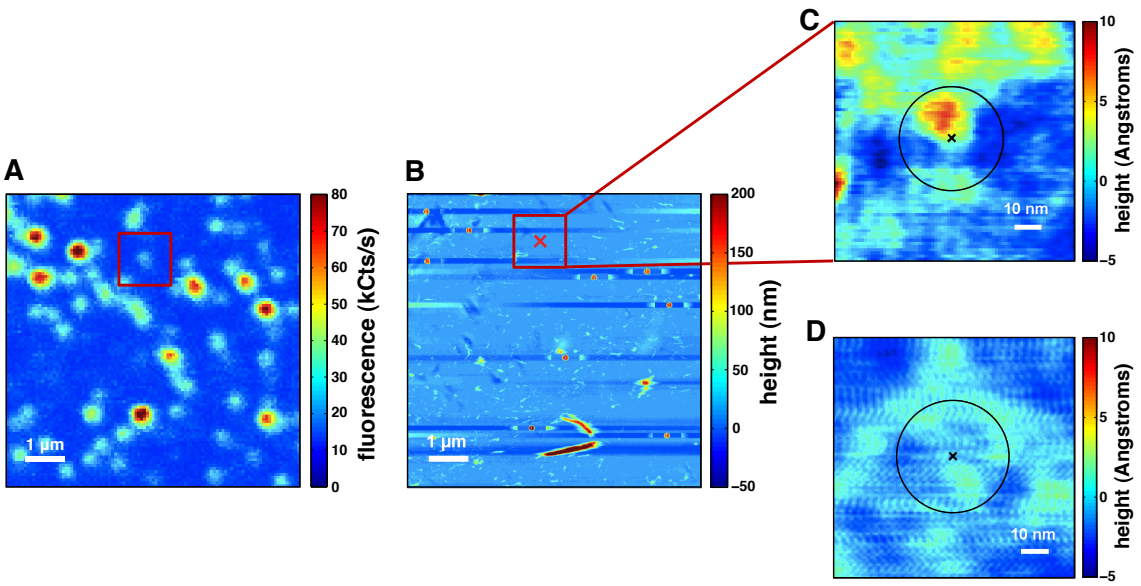

Figure 3.2: Co-localization of a single shallow NV center and a Gd^{3+} molecule. (A) Fluorescence image of a 7.5 μm × 7.5 μm area of the diamond crystal, showing several gold nanoparticles (bright spots), and NV centers (less intense spots). Location of a single NV center, marked by a red square, was determined in relation to the gold nanoparticles. (B) AFM image of the same region of the diamond surface, showing gold nanoparticles (red dots). The red cross marks the location of the NV center, deduced from the fluorescence image. (C) AFM image of the 100 nm × 100 nm region of the diamond surface centered at the location of the NV center (marked by a black cross). The black circle shows the one standard deviation uncertainty in the NV center position, with a single Gd^{3+} molecule present within the circle (bright spot). (D) AFM image of the same area as in (C), after Gd^{3+} molecules were removed from the diamond surface.

3.4 Measurement of magnetic noise from a single Gd^{3+} molecule attached to a diamond surface using a single shallow NV center

Once we located a single Gd^{3+} molecule with a nearby NV center, we performed all-optical magnetic sensing of this molecule. At room temperature, the $S = 7/2$ electron spin of the Gd^{3+} ion fluctuates with a relaxation rate (γ_{Gd}) on the order of 10 GHz [76,77]. These spin-flips give rise to a fluctuating magnetic field at the location of the NV center, with a Fourier spectrum of width $\approx \gamma_{Gd}$. The Fourier component of this fluctuating magnetic field at the frequency corresponding to the zero-field splitting of the NV center ground state spin manifold (S = 1) drives magnetic dipole transitions between these sublevels (Fig. 3.3A). We detected these transitions by first optically pumping the NV center into the $m_s = 0$ sublevel, and then measuring its spin-state-dependent fluorescence after a variable delay time τ (Fig. 3.3B, inset). In the absence of Gd^{3+} molecules, the NV spin-state population difference decayed with rate $\Gamma_{intrinsic}$ due to spin-lattice relaxation. However, when the NV center was in proximity to a Gd^{3+} molecule, the measured NV population relaxation rate increased to $\Gamma_{total} = \Gamma_{intrinsic} + \Gamma_{induced}$ (see Appendix A), which constitutes magnetic sensing of single-molecule electron spin. For example, the red circles in Fig. 3.3B show the result of the NV spin-state relaxation measurements for the NV-Gd^{3+} molecule pair displayed in Fig. 3.2C (the red line is an exponential fit); the blue squares in Fig. 3.3B illustrate the spin-state relaxation rate of the same NV center prior to attachment of the Gd^{3+} molecule. The comparison of these measurements clearly shows a dramatic

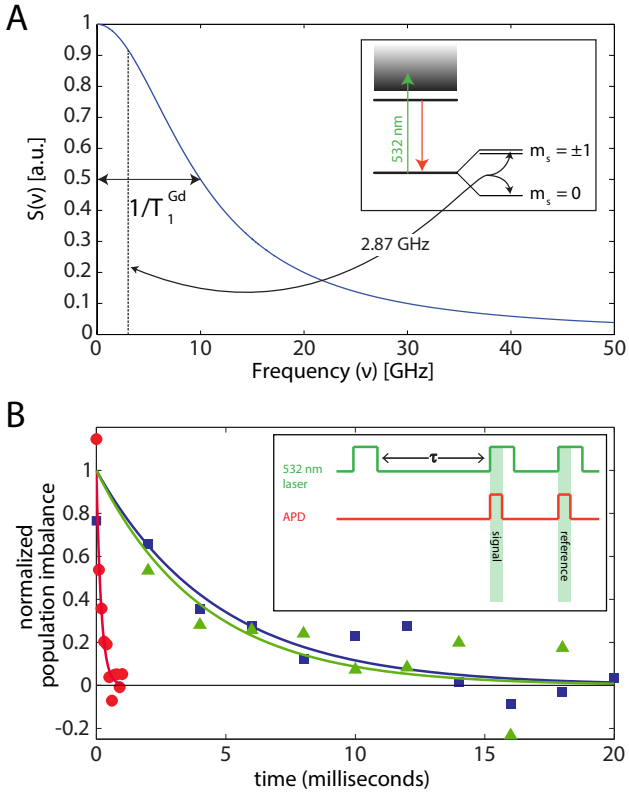

Figure 3.3: Measurement of magnetic noise from a single Gd^{3+} molecule attached to a diamond surface using a single shallow NV center. (A) Schematic power spectrum of the fluctuating magnetic field due to relaxation of the Gd^{3+} electronic spin (inset: NV-center electronic excited and ground states, with ground-state spin sublevels). Fourier components of this spectrum near the frequency resonant with the NV center zero-magnetic-field splitting lead to an increase in the NV center spin-state population relaxation rate. (B) Demonstration of NV magnetic sensing of a single Gd^{3+} molecule on the surface of bulk diamond. Measurements of the NV center spin-state population difference relaxation and exponential fits. Clean diamond surface: blue squares and blue line. Gd^{3+} molecules attached to the diamond surface: red circles and red line. Re-cleaned diamond surface: green triangles and green line. The AFM image for this NV center is shown in Fig. 3.2C, where it is demonstrated that it is in proximity to a single Gd^{3+} molecule. The scatter of the experimental data points is consistent with photon shot noise, with total averaging time on the order of an hour (not including the time needed to correct for setup drifts). Inset: Pulse measurement scheme for measuring the NV center spin-state relaxation rate. An avalanche photodiode (APD) was used for NV-center red fluorescence detection.

increase of the relaxation rate in presence of a single Gd^{3+} molecule. Once the molecule was removed (Fig. 3.2D), the relaxation returned to the intrinsic rate (green triangles in Fig. 3.3B).

3.5 Magnetic noise measurements in the single Gd^{3+} molecule sensing regime

The inset of Figure 3.4 summarizes the measured Gd-induced relaxation rates of for multiple NV-Gd^{3+} molecule pairs, with varying NV-molecule separations. We performed a total of 23 co-localization experiments, together with population relaxation measurements of the corresponding NV centers. In 14 of the 23 co-localization experiments, we could reliably identify single Gd^{3+} molecules and extract the separation between an NV center and a Gd^{3+} molecule; while in the remaining 9 experiments, we could not do so because of finite AFM tip resolution or rough surface topography. Seven of the data points exhibit a significant (greater than two standard deviation) increase in NV spin relaxation, and the corresponding co-localization measurements show the presence of a single Gd^{3+} molecule near the NV center position. As noted above, removal of the Gd^{3+} molecules from the diamond surface resulted in the relaxation rate returning to its intrinsic value in all cases.

A comparison of these data with Monte Carlo simulations (shown as background color plot in the inset of Fig. 3.4) provides further evidence of NV magnetic detection of a single-molecule electron spin. In the simulation, we calculated the probability density of obtaining a particular NV spin relaxation rate for a given NV-Gd^{3+}

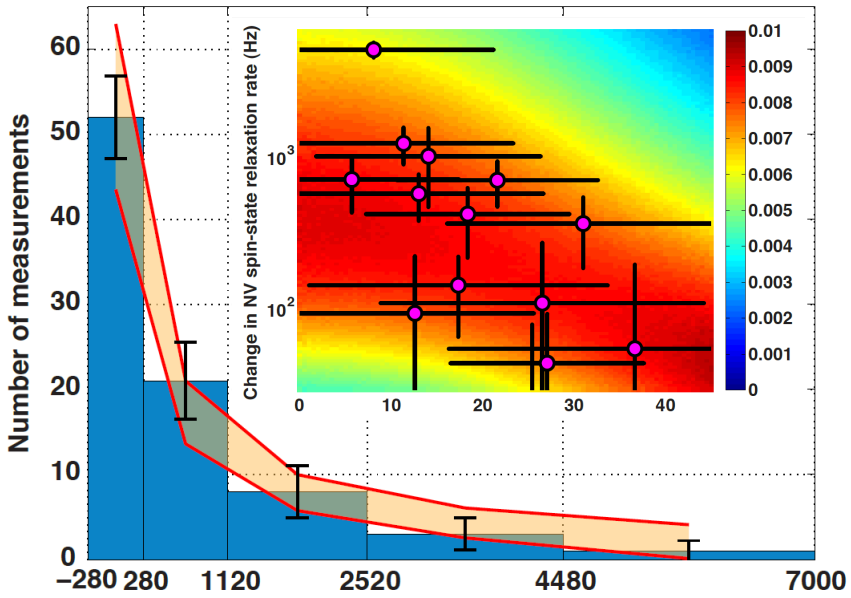

Figure 3.4: Magnetic noise measurements in the single Gd^{3+} molecule sensing regime. Results of 85 Gd-induced NV center spin-state relaxation rate measurements, along with a Monte-Carlo simulation band. The experimental data are grouped into five bins, with the error bars calculated by combining bin sampling uncertainty and relaxation rate fitting uncertainty (see Appendix A). The theoretical band was obtained from Monte Carlo simulations of the experiment, with parameters given in the text. Inset: results of 14 co-localization and NV center spin-state relaxation rate measurements in which a single Gd^{3+} molecule was identified near a single shallow NV center. The background displays the results of Monte Carlo simulations of the experiment, with the color scale indicating the probability density of obtaining a particular NV center spin-state relaxation rate for a given separation between the NV center and the proximal Gd^{3+} molecule. The simulation was performed for 20 nm separation between Gd^{3+} molecules, and NV center co-localization uncertainty of 15 nm. For a quantitative comparison, we performed a two-variable Kolmogorov-Smirnov statistical test, resulting in the Z-statistic value of 1.1, which indicates that the data points are consistent with the simulated distribution (see Appendix A).

molecule separation (see Appendix A) within experimental uncertainties. We used an NV center depth of 6 nm, derived from calculations for 3 keV nitrogen ion implanta-

tion energy, a mean Gd^{3+} molecule spacing of 20 nm, derived from the AFM and Cy3 measurements described above, and a Gd^{3+} spin-relaxation rate of 10 GHz [76, 77]. As seen in the inset of Fig. 3.4, the experimental data points are consistent with the simulated probabilities (see Appendix A).

Additional evidence for magnetic detection of single-molecule electron spins is provided by an independent set of 85 spin relaxation rate measurements that we performed on 26 shallow NV-centers over several cycles of Gd^{3+} molecule attachment and removal. As shown in the main plot of Fig. 3.4, the resulting data are grouped into five bins with the error bars calculated by combining the bin sampling and relaxation rate fitting uncertainties (see Appendix A). Also shown in this figure is a band of theoretically calculated NV spin relaxation rates, which we obtained from Monte Carlo simulations of the experiment, with the NV center depth of 6 nm, Gd^{3+} spin-flip rate varying in the range 10 to 20 GHz, and mean Gd^{3+} surface density varying in the range $1/(20\text{ nm})^2$ to $1/(25\text{ nm})^2$. These parameters yield simulated NV center spin relaxation rate distributions that are consistent with experimental data, again confirming that the observed NV spin relaxation rate increase is due to the proximity of a single-molecule electron spin. While other sets of model parameters in principle can be fit to the experimental data, all realistic model fit parameters correspond to regimes in which only a single Gd^{3+} spin contributes to increased NV center spin-state relaxation rate (see Appendix A). The "sensing radius" of an NV center (defined as the NV-Gd^{3+} molecule separation for which the change in NV center spin relaxation rate is equal to the measurement uncertainty) is determined to be approximately 12 nm. This means that with probability over 80% only a single Gd^{3+} molecule can

substantially contribute to the induced NV center spin relaxation rate even for highest Gd^{3+} molecule densities used.

The detection sensitivity of our experiment is limited by photon shot noise. By monitoring NV center fluorescence after optical pumping and a relaxation-in-the-dark period of ≈ 2 ms, chosen to be on the order of the NV center intrinsic T_1 time, a single Gd^{3+} molecule spin at a distance of 10 nm can be detected after approximately five minutes of averaging (see Appendix A). The sensitivity to other paramagnetic species depends on their magnetic moments and the magnitude of their fluctuating magnetic fields at the frequency corresponding to the $m_s = 0 \rightarrow m_s = \pm 1$ transition (see Appendix A), which can be varied by applying a constant magnetic field. In order to detect radicals with long relaxation times, such as some nitroxides, NV spin coherence relaxation (affecting the measured T_2 time) may be most suitable [78].

3.6 Conclusions and outlook

Our method for all-optical magnetic sensing of single paramagnetic molecules using shallow NV centers in diamond has potential implications to studies of a wide range of bio-chemical molecules and processes. Together with recent experiments demonstrating NV magnetic sensing of nanoscale ensembles of nuclear spins [74, 75], the combination of single-molecule covalent attachment, co-localization, and magnetic sensing techniques is an important step towards magnetic imaging measurements on individual biological molecules attached to the diamond surface [79]. Our magnetic measurement scheme directly detects the magnetic field created by a paramagnetic molecule, without the need for fluorescent tagging and can be applied to detect and

study small molecules without suffering from blinking or photo-bleaching [80]. Since NV center-based magnetometry was recently shown to be bio-compatible [81], our approach can also be used for *in vivo* magnetic sensing with single-molecule sensitivity. Specifically, our covalent attachment scheme can be extended to nanodiamonds, functionalizing them to target certain cellular organelles, as well as functionalizing with chemical species (spin traps) that react with short-lived free radicals to produce persistent paramagnetic molecules, which can then be magnetically detected. Because radicals are thought to play a key role in biochemical processes such as cellular signaling, aging, mutations, and death [63–66], the ability to detect small concentrations (approaching 100 μM, corresponding to mean separation of approximately 25 nm) of short-lived radicals inside living cells could be a powerful tool in studying these processes with possible applications for disease detection and drug development. Finally, our methods could also find applications in nanoscale and materials science, for example, in studies of molecular magnets on a diamond surface, and when combined with the recently demonstrated scanning probe techniques [82] they could enable imagining of rapidly fluctuating magnetic fields near the surfaces of materials such as superconductors [83], topological insulators [23,84], and others (ferromagnets, multi-ferroics, and so-forth).

center

Chapter 4

Time-resolved detection of single electronic spins in solution

4.1 Introduction

The ability to dynamically sense small concentrations of electronic spins *in vitro* could lead to new insights into processes involving reactive oxygen species such as cancer, cellular signalling, mutation, and aging [63–66]. Combined with site-directed spin labeling, single electronic spin detection with nanometer spatial resolution could enable characterization of the intracellular magnetic environment and its effect on biological molecular dynamics [85]. Additionally, the use of individual electronic spins as ancillary sensors could enable single-molecule nuclear magnetic resonance *in vitro* [86]. While many conventional magnetic field sensors, including superconducting quantum interference devices [23], semiconductor Hall effect sensors [24], spin exchange relaxation-free atomic magnetometers [25], and bulk electron spin res-

onance [67] offer exquisite sensitivity, their macroscopic size prevents their use with nanoscale samples. Magnetic resonance force microscopy offers single spin sensitivity but typically operates under vacuum and at cryogenic temperatures [21, 22].

Several experiments have shown the potential of NV centers for magnetometry applications [68–71, 81, 87], and these capabilities have been demonstrated in nano-diamonds [72, 73, 78, 88, 89]. Additionally, there has been significant work in demonstrating the practical realization of magnetometry for biological applications, such as for electron [71, 87] and nuclear spin sensing [74, 75], including detection of single electronic spins [82, 90] and single protons [86] using bulk diamond. To date, NV-based measurements of electronic spins in solution at biologically-relevant concentrations (on the order of 100 nM) have only been achieved using large ensembles of NV centers in bulk diamond [87]. Nano-diamonds, although more challenging to work with, are better suited for certain biological applications (e.g. sensing of native radical concentrations in living cells). Here, we make use of nano-diamonds that contain single NV centers to detect the adsorption of individual Gd^{3+} ions onto the diamond surface in solution (Fig. 4.1A) and observe a strong dependence of the adsorption rate on the Gd^{3+} concentration, under ambient conditions at room-temperature.

4.2 Measurement of magnetic noise from Gd^{3+} ions attached to the nano-diamond surface

We detect individual Gd^{3+} ions by monitoring the magnetic field fluctuations they create at the locations of proximal individual NV centers, similar to the scheme

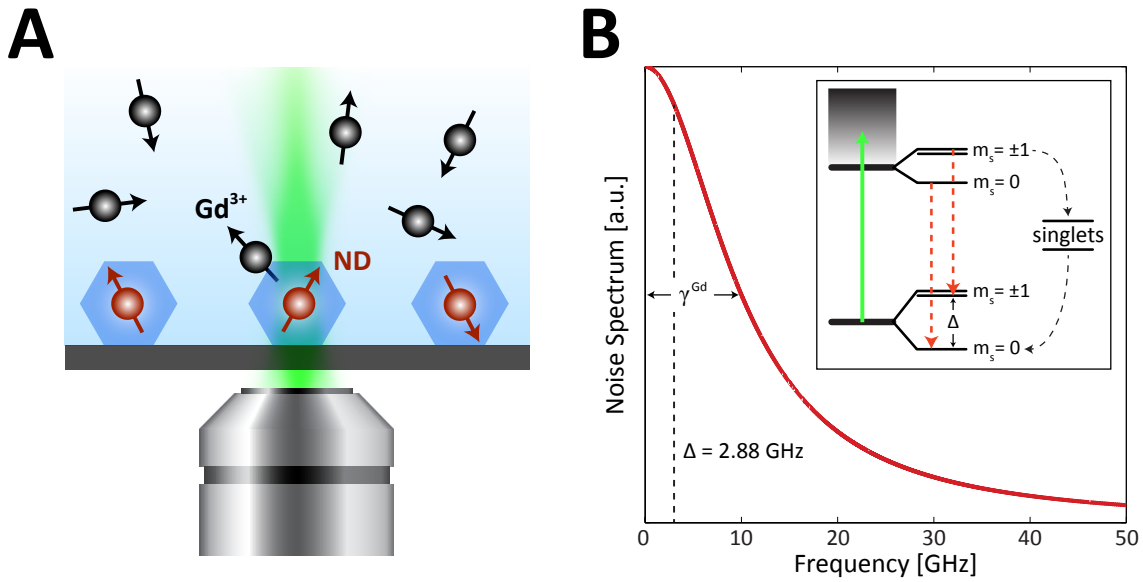

Figure 4.1: Schematic of measurement setup, Gd^{3+} magnetic noise spectrum, and NV center level-structure at room temperature. (A) Single Gd^{3+} spin detection using an NV center contained in a nano-diamond. Gd^{3+} ions attach to the surface of the nano-diamond crystal. (B) Schematic power spectrum of the fluctuating magnetic field due to relaxation of the Gd^{3+} electronic spin. Inset: NV center electronic level structure, showing the characteristic $\Delta = 2.88$ GHz zero-field splitting (ZFS) in the ground state. The singlet states provide a non-fluorescent method of converting from $m_s = \pm 1$ to $m_s = 0$, allowing for state initialization and read-out. Fourier components of the power spectrum near the NV center ZFS lead to an increase in the relaxation rate of the NV center electronic ground states.

employed in [71, 73, 87, 90]. Given that aqueous Gd^{3+} spins have relaxation rates, γ^{Gd}, of approximately 10 GHz [76, 77], they create a corresponding magnetic noise spectrum that overlaps with the zero-field splitting of the NV center (Fig. 4.1B). The magnetic noise of the Gd^{3+} ions is sensed by measuring their effect on the relaxation rate, γ^{NV}, of the electronic ground state spin sub-levels of a single NV center (see Appendix B for method of determining single NV centers). In order to measure this relaxation rate, we first polarize the NV center into its $m_s = 0$ sub-level, wait for time τ, and then read out the $m_s = 0$ population (pulse sequence is shown in the inset of

Fig. 4.2A). By sweeping over various values of τ, we can map out the full T_1 curve and thus determine the relaxation rate γ^{NV}. When there are no nearby Gd^{3+} ions, i.e. when the nano-diamond is immersed in water, the NV center exhibits its intrinsic relaxation rate γ_0^{NV} (blue data points, fit by blue curve, in Fig. 4.2A).

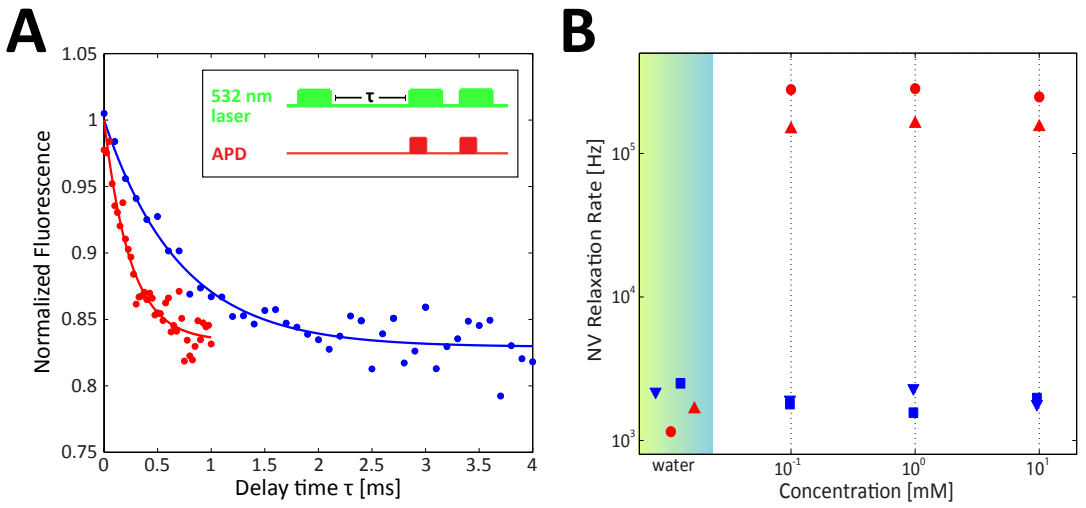

Figure 4.2: Measurement of magnetic noise from Gd^{3+} ions adsorbed onto the nano-diamond surface. (A) Magnetic sensing of Gd^{3+} ions on the surface of a nano-diamond. Measurements of the NV center normalized fluorescence contrast for different values of τ (to give full relaxation curves) and exponential fits. Blue points and curve: clean nano-diamond surface. Red circles and curve: Gd^{3+} ions attached to the nano-diamond surface. Inset: Pulse sequence used for measuring the relaxation rate of the NV center's electronic ground states. (B) Equilibrium relaxation rates of NV centers at different concentrations of $GdCl_3$ (signal) and $LaCl_3$ (control). Red points: NV centers immersed in $GdCl_3$; blue points: NV centers immersed in $LaCl_3$. Different shapes represent different NV centers (four different NV-containing nano-diamonds in total).

In the presence of Gd^{3+} ions, i.e. when the nano-diamond is immersed in a solution of $GdCl_3$ and Gd^{3+} ions have adsorbed on the nano-diamond surface, there is a clear increase in relaxation rate caused by the additional magnetic noise introduced into the NV center's environment (red data points, fit by red curve, in Fig. 4.2A). In

the presence of a single Gd^{3+} ion, the NV center's relaxation rate is the sum of its intrinsic relaxation rate and the induced relaxation rate caused by the magnetic noise stemming from the Gd^{3+} ion, namely $\gamma^{NV} = \gamma_0^{NV} + \gamma_{Gd}^{NV}$. As derived in the SI of [90], $\gamma_{Gd}^{NV} = 2\frac{S(S+1)g^4\mu_B^4}{r^6}\frac{\gamma^{Gd}}{(\gamma^{Gd})^2+\Delta^2}$, where $S = 7/2$ for a Gd^{3+} ion, $g \approx 2$ is the electron g-factor, μ_B is the Bohr magneton, r is the distance between the NV center and the Gd^{3+} ion, and $\Delta \approx 2.88$ GHz is the zero-field splitting of the NV center.

Magnetic noise drops off with r^6 dependence, therefore only Gd^{3+} ions that are within several nanometers of the NV center can be detected [90]. The nano-diamonds that we use have a median size of approximately 25 nm, thus we expect a significant fraction of the NV centers will be within several nanometers of the surface. We measured the relaxation rates of 14 NV centers and found that 13 of them exhibit a significant increase in relaxation rate when immersed in a solution containing Gd^{3+} ions. We also observe that when the nano-diamonds are subsequently immersed back into a pure water solution, the relaxation rates do not return to their previous values, suggesting that the measured signal is dominated by Gd^{3+} ions adsorbing onto the diamond surface.

In order to show that the Gd^{3+} ions are indeed adsorbing onto the surface of the nano-diamond, we immersed nano-diamonds in different concentrations of $GdCl_3$ and measured equilibrium relaxation rates. To ensure that the equilibrium relaxation rates were reached, we used high concentrations of $GdCl_3$ (100 μM, 1 mM, and 10 mM). As shown in Fig. 4.2B, the equilibrium relaxation rates of NV centers are independent of the concentration, indicating that the process responsible for the increase in NV relaxation rate is irreversible. We verify that the measured increase in relaxation

rate is indeed created by magnetic field fluctuations of Gd^{3+} spins by repeating the experiment with non-paramagnetic La^{3+} ions (using $LaCl_3$ instead of $GdCl_3$). Even at 10 mM $LaCl_3$ concentration, we observe no measurable increase in relaxation rate.

4.3 Time-resolved sensing of the adsorption of single Gd^{3+} ions onto the nano-diamond surface

The adsorption rate, in contrast to the equilibrium induced relaxation rate, is strongly dependent on the $GdCl_3$ concentration. Fig. 4.3A shows the measured relaxation rate of the NV centers by repeatedly probing a single delay time τ. This allows for a large increase in temporal resolution at the expense of signal-to-noise ratio. At low concentration of $GdCl_3$ (25 nM, top panel of Fig. 4.3A) we observe that the relaxation rate begins to increase on the timescale of hours. When the concentration of the $GdCl_3$ used is increased to 100 nM (middle panel of Fig. 4.3A), we notice that the relaxation rate begins to increase on the timescale of tens of minutes. Finally, at high concentration (100 μM $GdCl_3$, bottom panel of Fig. 4.3A) the increase happens faster than can be detected in our experiment (less than 4 minutes). This measurement reveals that the adsoprtion rate of Gd^{3+} ions on the surface of the nano-diamond strongly depends on the concentration of $GdCl_3$, as expected.

We repeat the measurement of the relaxation rate of NV centers in 100 nM of $GdCl_3$ by repeatedly probing a single delay time τ while immersing NV centers. Capitalizing on the increased temporal resolution of this measurement, we observe discrete steps in the relaxation rate for some NV centers, indicating the attachment

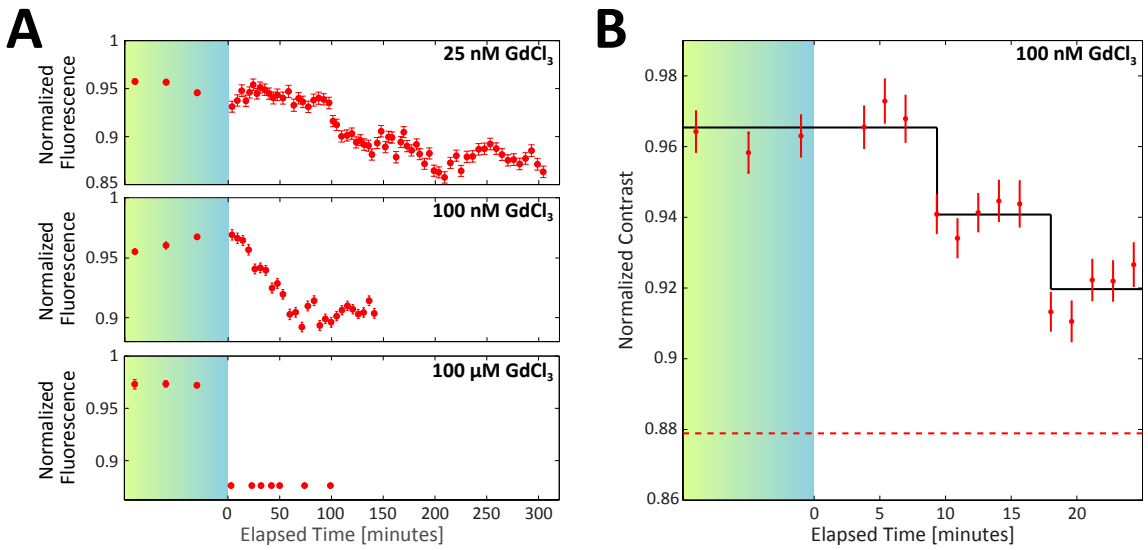

Figure 4.3: Time-resolved sensing of the adsorption of single Gd^{3+} ions onto the nano-diamond surface using a single delay time, $\tau = 150$ μs, of the relaxation curve. (A) Concentration dependence of the Gd^{3+} adsorption time (and thus NV center relaxation rate). Shaded region before time 0: three points taken in water. At time 0, the water was removed and 25 nM (top panel), 100 nM (middle panel), or 100 μM of $GdCl_3$ was pipetted on top of the nano-diamond being observed. (B) Adsorption of single Gd^{3+} ions onto the nano-diamond surface. Shaded region before time 0: three points taken in water. At time 0, 100 nM of $GdCl_3$ was pipetted on top of the nano-diamond being observed. Black curve is a numerical fit to the red data points using a model which assumes discrete Gd^{3+} attachment events. Dashed red line is the contrast once the equilibrium relaxation rate is reached for this particular NV center.

of individual Gd^{3+} ions to the diamond surface (Fig. 4.3B). The data was numerically fit using a model that assumes a discrete number of Gd^{3+} attachment events (black line). The steps in this fit correspond to induced relaxation rates γ_{Gd}^{NV} of (2.2 ± 0.5) kHz and (3 ± 1) kHz, which are similar to the relaxation rates of shallow NV centers in bulk diamond sensing the magnetic noise from single Gd-molecule electron spins, as demonstrated in [90]. Signatures of these steps were observed for 3 out of 5 nano-diamonds that were immersed in 100 nM of $GdCl_3$, and step sizes and timescales were

consistent with each other (see Appendix B).

4.4 Conclusions and outlook

Our observations represent an important step toward the development of *in vitro* magnetic sensors for dynamic imaging of biological processes at the single spin level. In the current measurement scheme, we rely on the natural adsorption of Gd^{3+} ions to the nano-diamond surface in order to dynamically sense single electron spins in solution. However, this could be extended to reactive oxygen species (ROS) in living cells by attaching stable spin traps to the nano-diamond surface before targeting the nano-diamonds within cells. The nano-diamonds could be targeted to important biomolecules in order to sense their magnetic environment, or to specific organelles/sites within cells to determine the flow of electrons and provide information on different ROS processes [63–66]. Our methods could be extended to sensing the whole magnetic noise spectrum by varying a static magnetic field (and thus the separation between the $m_s = 0$ and $m_s = \pm 1$ spin states) as opposed to measuring a single point of the magnetic noise spectrum as demonstrated here. This could provide the information necessary to identify the magnetic species that is the root cause of the magnetic noise, and/or to discriminate between multiple different magnetic species. Finally, combined with scanning probe magnetometry [82, 91], this approach could be used for time-resolved sensing of fluctuating magnetic fields near the surfaces of complex materials [92, 93].

Chapter 5

Conclusions and outlook

Precision magnetometry at room temperature is an important challenge that could lead to revolutionary advances. While there have been many advances in quantum technologies using other systems, the NV center in particular is well-poised to be the optimal choice for magnetometry under ambient conditions. This is due to the fact that the electronic ground state of the NV center retains its quantum properties at room temperature, unlike many other quantum systems that need to be cooled. Another distinct advantage is the solid-state, diamond nature of the substrate in which the NV center is embedded. This makes the NV center in diamond particularly well-suited for biomedical magnetometry applications. Finally, given the fact that the NV center is exceptionally small (i.e. a point defect), it is an ideal choice for applications requiring high spatial resolution, or that require the magnetometer to be embedded inside the sample.

This thesis represents our progress towards the goal of precision magnetometry at room temperature using NV centers. Although there have been many previous

proof-of-principle experiments demonstrating the magnetometry capabilities of NV centers [57, 68–70, 94, 95], in this thesis we have applied these methods to exhibit their potential for real-world applications. In Chapter 3, we have shown that we can reliably implant NV centers close to the diamond surface, allowing them to interact with the environment outside the diamond lattice. Even more importantly, we showed that we can control the diamond surface such that the properties of these shallow NV centers are very similar to those observed for deeply implanted NV centers. Retaining sensitivity while also coming into closer contact with the environment was key to being able to sense the single-molecule electron spins that we covalently attached to the diamond surface. In Chapter 4, we demonstrated that with proper surface preparation, nano-diamonds could contain NV centers with properties similar to those exhibited in bulk diamond. By probing the relaxation rate of NV centers at a single delay time, we were able to dynamically sense individual Gd^{3+} ions adsorbing onto the surface of nano-diamonds. This allowed us to do time-resolved magnetic sensing of single electron spins at room temperature, paving the way for high temporal resolution magnetometry. Again, the key to this experiment was demonstrating control of the nano-diamond surface in order to harness the NV center as a precision magnetometer.

There have been many notable contributions to the field of NV center magnetometry from a variety of groups. Initial demonstration of NV-magnetometry in living cells has shown the biocompatibility of nano-diamonds [88], although there remains work to be done to use these methods for actual biomedical applications. Diamond scanning probe magnetometry shows incredible promise, and single (polarized) electron spin detection has already been demonstrated with this method [82].

Combined with our methods, one could envision sitting at one point on a surface and measuring small magnetic noise with high temporal resolution. There have also been other demonstrations of magnetic sensing of paramagnetic ions, both fixed [73] and in solution [71]. However, the only other demonstration of magnetic sensing of paramagnetic ions at biologically relevant concentrations (on the order of 100 nm) was done using an ensemble of NV centers (limiting the spin and spatial resolution) in bulk diamond (limiting the applicability to *in vitro* magnetometry) [87]. More recently, there have been exciting results on the measurement of nuclear spins on the surface of bulk diamonds [74, 75], and even single proton spin resolution has been achieved [86]. Due in large part to all of this recent progress, the field of NV magnetometry remains a particularly active field.

There are many exciting avenues that our work is currently being extended to. For example, within our own group, there are ongoing efforts to perform magnetometry on the nuclear spins of individual proteins by attaching the proteins to bulk diamonds containing shallow-implanted NV centers. In particular, it has already been demonstrated that single proteins can be magnetically sensed on the bulk diamond surface [96]. To be useful for biomedical applications, however, one must find a way to determine the structure of single molecules. One example of how this could potentially be achieved is through the use of a large magnetic field gradient, thereby splitting the magnetic resonance frequency of individual nuclear spins within the molecule. That, however, has the challenge of having a large, stable magnetic field gradient that is known with very high precision. Our work could be extended to probing any surface that has a poorly understood magnetic field noise spectrum,

as by applying an external static magnetic field to our NV center, we could split the electronic ground state energy levels, thus allowing us to probe the entire noise spectrum. This could allow for better determination of the source of magnetic noise for complex systems, or to distinguish between different species creating magnetic noise. Additionally, the increased time resolution demonstrated in nano-diamonds could pave the way for time-resolved sensing of dynamic magnetic fields near the surfaces of complex systems [23, 83, 84, 92, 93].

Given the surface chemistry and bio-compatibility of diamond, the NV center is uniquely positioned to be an important magnetometer for biological and medical applications in the future. NV centers in bulk diamond, as discussed above, offer the potential of performing NMR spectroscopy on individual molecules attached to the diamond surface. This could be revolutionary for biopharmaceutical research: knowing the exact structure of any molecule, particularly those that are pathogenic, could provide enormous insight in drug development. While many approaches currently rely on quite a bit of guesswork, single molecule NMR could enable a more structured approach to the identification of drug candidates. Additionally, with increased time resolution, one could use our methods to watch chemical reactions between different molecules, showing exactly which reaction sites are important so that we can prevent unwanted (or promote desired) reactions in the future. Another exciting biomedical application is *in vitro* magnetic field sensing with time resolution. One could imagine visualizing a network of targeted nano-diamonds inside of a cell using a wide-field microscope and watching individual electron spins (radicals) make their way through the cell during different biochemical processes. Some of these processes are physiological,

such as cellular signalling, whereas others are pathological, such as cancer, aging, and death [63–66]. The ability to perform single electron spin magnetometry with high spatial resolution could open the door to a better understanding of these processes. And, of course, with better understanding comes better control, potentially leading to better diagnosis and treatment.

NV centers in diamond have emerged as one of the most promising new quantum technologies. This thesis offers a modest advance on the control of this system as a magnetometry device, but there exist many other exciting applications that the NV center community is continuing to develop. Whether it be quantum computing, quantum communication, or metrology, the nitrogen-vacancy center in diamond has the potential to revolutionize the way we interact with each other and the world around us.

Appendix A

Supporting material for Chapter 3

A.1 Materials and methods

A.1.1 Diamond samples

The samples used in this work were polished, single-crystal electronic grade diamonds grown by chemical vapor deposition (Element Six). The diamonds were {100}-cut, and contained substitutional nitrogen and boron in concentrations less than 5 parts per billion (ppb) and 1 ppb respectively. Prior to implantation, the diamond surface was etched approximately 1 μm, using an Ar-Cl_2 plasma etch (25 sccm Ar, 40 sccm Cl_2, ICP RF 400 W, bias RF 250 W, duration 150 s), followed by an O_2 plasma etch (30 sccm O_2, ICP RF 700 W, bias RF 100 W, duration 150 s). Nitrogen implantation was done by INNOViON Corporation using a $^{15}N^+$ dosage of 10^9 cm^{-2} and an implantation energy of 3 keV, corresponding to a SRIM calculated depth of (5.3 $\pm$ 2.2) nm. The implanted diamonds were annealed in vacuum using

the following procedure: (a) 2 hour ramp to 400°C, (b) 4 hours at 400°C, (c) 2 hour ramp to 800°C, (d) 8 hours at 800°C and (e) 4 hour ramp to room temperature. After annealing, the diamonds were cleaned in a 3-acid mixture (equal volumes of concentrated H_2SO_4, concentrated HNO_3, and 1 M $HClO_4$) for two hours under reflux conditions, followed by air annealing for 10 hours at 420°C.

A.1.2 Optical setup

We used a home-built scanning confocal microscope to optically address and read out single NV centers. The diamond was placed with NV-side down on top of a No. 0 glass coverslip. The inverted Nikon Plan Fluor 100x oil immersion objective (NA = 1.3) was positioned under the coverslip. Its vertical position was controlled with a piezoelectric scanner (Physik Instrumente P-721 PIFOC) and the lateral position of the laser beam focus was controlled with a closed-loop scanning galvanometer (Thorlabs GVS012). Optical excitation was performed with a 532 nm laser (Information Unlimited, MLLIII532-200-1) modulated with an acousto-optic modulator (Isomet Corporation, 1250C-974) in a double-pass configuration. NV center fluorescence was filtered with a 532 nm notch filter (Semrock, NF03-532E) and a 633 nm long-pass filter (Semorck, LP02-633RU) and collected using an avalanche photodiode (PerkinElmer, SPCM-AQRH-14-FC). The TTL voltage pulses used in our measurements were produced using a 400 MHz PulseBlasterESR-PRO pulse generator from Spincore Technologies.

A.2 Sample preparation

A.2.1 Diamond surface cleaning procedure

The diamond cleaning procedure was optimized to minimize background fluorescence and to ensure that the surface was terminated with carboxyl groups. The samples were cleaned in a 3-acid mixture (equal volumes of concentrated H_2SO_4, concentrated HNO_3, and 1 M $HClO_4$) for 4 hours under reflux conditions, followed by concentrated ultrapure (99.999%) HNO_3 at 90°C for 1 hour, 1.0 M of NaOH at 90°C for one hour and 1.0 M of HCl at 90°C for one hour. The diamonds were washed with ultrapure water after each step.

A.2.2 Gd^{3+}-molecule attachment procedure

Gd^{3+} molecules were synthesized and purified using methods discussed in [97]. To activate the surface carboxyl groups, the diamonds were treated in a solution of 1-ethyl-3-(3-dimethylaminopropyl)carbodiimide (EDC; 100 μM) and *N*-hydroxysuccinimide (NHS; 100 μM) at room temperature for 12 hours. After rinsing with ultrapure water, the diamonds were placed in a 1 mM Gd^{3+}-molecule solution and reacted at room temperature for 2 hours. The diamonds were then rinsed with ultrapure water. The surface density of attached molecules could be decreased by diluting the Gd-ligand solution.

A.2.3 Gd^{3+}-molecule removal procedure

We repeated the cleaning procedure described above to hydrolyze the peptide bonds and remove the Gd^{3+} molecules from the diamond surface.

A.3 Determination of Gd^{3+}-molecule surface density

A.3.1 Atomic force microscopy

We used an Asylum MFP-3D atomic force microscope (AFM) in AC mode to image the surfaces of our diamond samples, in air. The probes (Nanosensors SSM-FMR) had a spike radius of (3 ± 2) nm and a resonant frequency between 45 and 115 Hz. Samples were mounted onto cover slides using SPI die-cut nonconductive double-sided adhesive discs. The AFM trace and retrace data were averaged together linearly.

A typical AFM height image of a diamond surface after Gd^{3+} molecule attachment is shown in Fig. A.1A. We determined the mean separation between the surface molecules to be in the range 20 nm to 25 nm. The radii of the circular features (see Fig. A.1C) are consistent with the lateral resolution limit imposed by the AFM tip while the height (see Fig. A.1B) is consistent with that expected for single Gd^{3+} molecules, estimated from bond lengths and angles. The orientation of the molecules on the surface in ambient conditions is unknown, and the variation of orientations likely contributes to the range of AFM spot heights.

To confirm that these surface features are indeed single Gd^{3+} molecules, we attached to each molecule a single Cy3 fluorescent dye, attached the resulting Cy3-Gd^{3+}

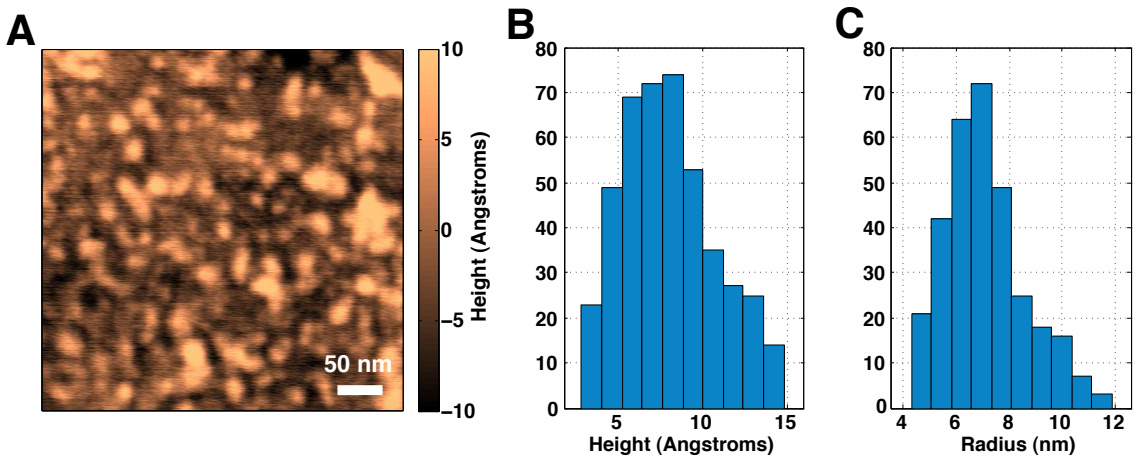

Figure A.1: Determination of the size of a single Gd^{3+} molecule. (A) 350 nm $\times$ 350 nm AFM height image of a diamond surface with Gd^{3+} molecules attached. (B) Histogram of the heights of the circular features in a larger AFM image, of approximate size 3 μm $\times$ 3 μm. The mean height of a single Gd^{3+} molecule is determined to be (8 $\pm$ 3) Å. (C) Histogram of the radii of these features. The mean radius of a feature that corresponds to a single Gd^{3+} molecule is found to be (7 $\pm$ 2) nm.

molecule to the diamond surface, and correlated the Cy3 fluorescence rate observed in our confocal microscope with the surface density observed in the AFM images. We calibrated the fluorescence rate of a single Cy3-Gd^{3+} molecule by attaching an optically resolvable concentration (achieved by diluting the stock ligand solution) of these molecules to the diamond surface and monitoring the fluorescence rate in the 542 - 633 nm band, filtering out fluorescence from NV centers (Fig. A.2A). A typical fluorescence time trace of a single Cy3-Gd^{3+} molecule under CW 532 nm illumination (2 μW) is shown in Fig. A.2B and displays a photo-bleaching pattern characteristic of a single-molecule emitter. We detected a mean fluorescence rate of 1200 photons/second from a single fluorescent Cy3-Gd^{3+} molecule. At high concentration, the surface molecules were no longer optically-resolvable (Fig. A.2C) but the fluorescence rate in a diffraction-limited focal spot suggested a mean surface density in the range

$1/(20\text{ nm})^2$ to $1/(25\text{ nm})^2$, consistent with that obtained in AFM measurements described above. Finally, inspection of this area of the surface in the AFM revealed circular features with height, radius and density that were in good agreement with those found after attaching Gd^{3+} molecules (see Fig. A.2D).

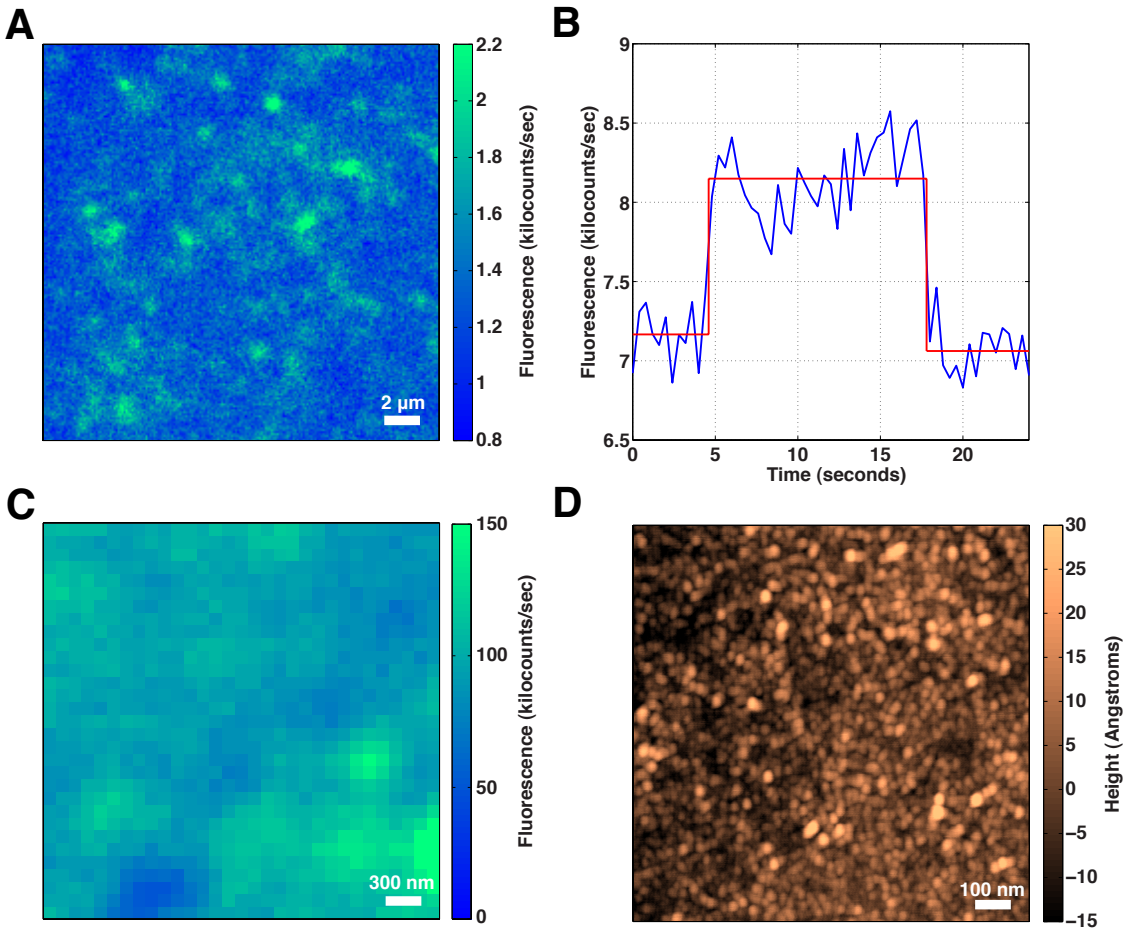

Figure A.2: Determination of Gd^{3+} molecule surface density. (A) 20 μm $\times$ 20 μm fluorescence image of single Cy3-ligand molecules. (B) Photobleaching of a single Cy3-ligand molecule under CW 532 nm laser illumination (2 μW). (C) 3 μm $\times$ 3 μm fluorescence image of a diamond surface saturated with Cy3-ligand molecules. (D) 1 μm $\times$ 1 μm AFM height image of the same diamond surface as in Fig. A.2C.

We conclude that the observed features are indeed single Gd^{3+} molecules. We

note that the surface concentration could be controlled by diluting the ligand solution and our attachment procedure resulted in a uniform distribution of molecules, with little aggregation.

These molecules are attached to the diamond via surface carboxylic groups. Some surface carboxylic groups may be chemically unreactive (due, for example, to steric hindrance by neighbouring surface groups, or other surface structure considerations [98–100]) and do not attach the Gd^{3+} molecules. From our measurements we conclude that the surface density of the "reactive" carboxylic groups is in the range $1/(20\text{ nm})^2$ to $1/(25\text{ nm})^2$.

A.4 Co-localization procedure

A.4.1 AFM drift correction

It took on the order of an hour to acquire each of the AFM scans used in our measurements. During that time, the AFM image underwent lateral drift, with typical magnitude of 10 nm per hour to 100 nm per hour. This introduced a shift in the relative positions of the features at the top of an AFM image, taken near the beginning of a scan, relative to the features at the bottom of an AFM image, taken near the end of the scan. In order to correct for the drift, we always acquired two consecutive AFM scans of the same area of the diamond surface, and, using numerical image processing, extracted the magnitude of the drift. We then corrected each of the two images for this drift, and averaged them together.

A.4.2 Co-localization steps

We determined the separation between an NV centre and the nearest Gd^{3+} molecule in a three-step co-localization procedure. First, the diamond surface was coated (via electrostatic attachment) with an optically resolvable density of 100 nm-diameter gold nanoparticles. These nanoparticles fluoresce in the same spectral region as the NV centres, and thus could be observed simultaneously with NV centers in our scanning confocal microscope. We compiled a map of the surface positions of these nanoparticles, together with a map of the NV centers in the same region (Fig. 3.2A). In the second step, the surface topography of this diamond was measured using the AFM (Fig. 3.2B). The gold nanoparticles could be clearly seen, together with a number of topographic features (pits and scratches) in the diamond surface, thus enabling us to compile a map of the positions of these surface features relative to the nanoparticles. Finally, after cleaning off the nanoparticles, we attached Gd^{3+} molecules to the diamond surface, and the diamond surface topography was measured using the AFM, yielding a map of the positions of the Gd^{3+} molecules in relation to the surface features. We used these three maps to deduce the positions of the Gd^{3+} molecules relative to the NV centers (Fig. 3.2C).

A.4.3 Co-localization uncertainty

The uncertainty in the position of an NV center relative to the Gd^{3+} molecules on the diamond surface was estimated by combining the uncertainties in each of the co-localization steps in quadrature. The dominant uncertainty, on the order of 10 nm, arose when matching the fluorescence and AFM maps of the nanoparticle posi-

tions. We used between 9 and 15 nanoparticles in this step. Their coordinates were extracted from Gaussian fits to the fluorescent spots in the confocal scan, and from spherical-dome fits to the corresponding features in the AFM scan. We deduced the position of the NV center in the AFM image by finding the transformation (scaling + rotation) that most accurately maps the fluorescence-scan coordinates of the nanoparticles to their coordinates in the AFM image and applying this transformation to the NV center fluorescence-scan coordinates. In order to estimate the associated uncertainty in the NV center AFM-scan coordinates, we ran Monte Carlo simulations that shifted each of the nanoparticles by a randomly-oriented normally distributed vector with a standard deviation equal to the mean distance between the transformed fluorescence-scan coordinates and the AFM-scan coordinates of the nanospheres, and then calculated the resultant NV center AFM positions. We set the uncertainty in the NV center AFM coordinates to be equal to the standard deviation of the resulting Gaussian distribution of the NV positions, see Fig. A.3. A similar procedure was implemented to estimate the uncertainties arising from the other two co-localization steps. The resulting total uncertainty was typically 15 nm.

A.5 Derivation of $\Gamma_{induced}$

We describe an NV center interacting with a bath of Gd^{3+} molecules by the Hamiltonian ($\hbar = 1$)

$$H = \frac{\Delta}{2}\sigma_z + \frac{1}{2}g\mu_B \left[B_x(t)\sigma_x + B_y(t)\sigma_y\right] \tag{A.1}$$

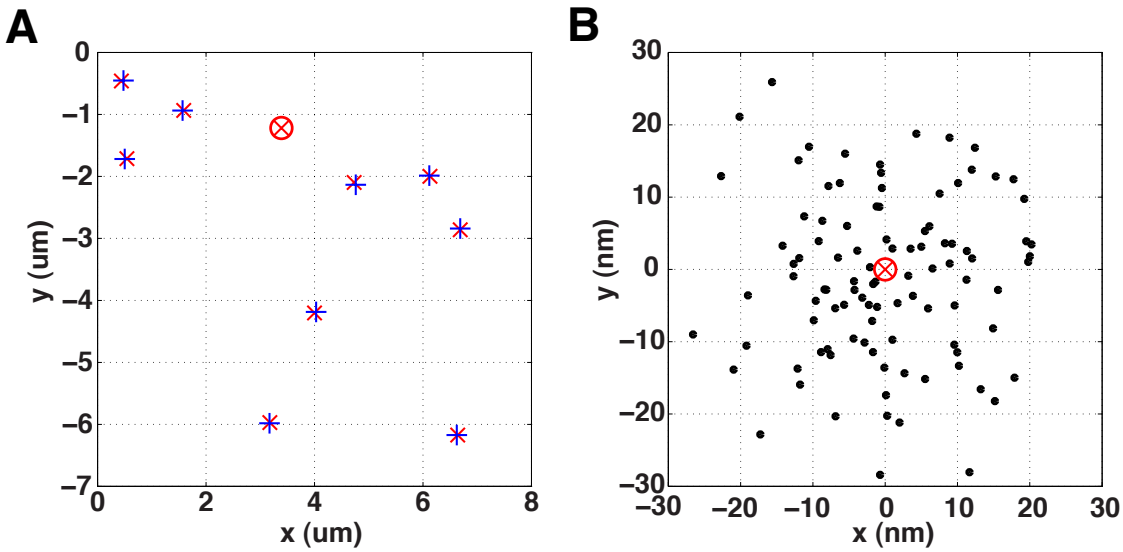

Figure A.3: Determination of co-localization uncertainty. (A) The transformed fluorescence image coordinates of an NV center (red circle with a cross) and the gold nanoparticles (all the other red crosses) overlayed on the AFM image coordinates of the same gold nanoparticles (blue crosses). (B) Monte Carlo simulation used to determine the error on the NV center position in Fig. A.3A. The red circle with a cross shows the most probable position of the NV center (normalized to the origin) while the blue dots show the distribution of possible positions that arise from the imperfect overlap of the fluorescence and AFM coordinates in Fig. A.3A. We take the standard deviation of the distribution of these positions to be the co-localization uncertainty. For the NV center shown this is approximately 10 nm, and the average value for all the NV centers is 15 nm.

where $\Delta \approx 2.87$ GHz is the zero-field splitting of the NV center, $g \approx 2$ is the electron g-factor, μ_B is the Bohr magneton, $\sigma_{x,y,z}$ are the Pauli spin operators, and $B_{x,y}(t)$ are the transverse components of the fluctuating magnetic field created at the NV center by the proximal Gd^{3+} spins. Here we consider the dynamics within the two-level subspace spanned by the states $|0\rangle$ and $|1\rangle$ of the NV center ground state triplet and treat $B(t)$ as a classical variable. The z-axis is chosen to be along the symmetry axis of the NV center and we ignore the term $\frac{1}{2}g\mu_B B_z(t)\sigma_z$ since its effect is suppressed by the large zero-field splitting. We take the state of the effective two-level system to

be

$$|\psi(t)\rangle = \alpha(t)|0\rangle + \beta(t)|1\rangle. \tag{A.2}$$

For an NV center initially prepared in the $|0\rangle$ state, first-order time-dependent perturbation theory in the interaction pictures gives [101]

$$\beta(t) = \frac{-i}{2} g\mu_B \int_0^t d\tau [\langle 1|\sigma_x(\tau)|0\rangle B_x(\tau) + \langle 1|\sigma_y(\tau)|0\rangle B_y(\tau)] = \frac{-i}{2} g\mu_B \int_0^t d\tau e^{i\Delta\tau} B_\perp(\tau) \tag{A.3}$$

for the amplitude of state $|1\rangle$. Here $B_\perp$ is the transverse component of the fluctuating magnetic field. Averaging over the classical variable $B_\perp(\tau)$, the transition probability is given by

$$P_1(t) = |\beta(t)|^2 = \frac{1}{4} g^2 \mu_B^2 \int_0^t d\tau_1 \int_0^t d\tau_2 e^{-i\Delta(\tau_1 - \tau_2)} \langle B_\perp(\tau_1) B_\perp(\tau_2)\rangle. \tag{A.4}$$

Using the Wiener-Khinchin theorem, the transition rate becomes

$$\Gamma_{0\to 1} = \frac{1}{4} g^2 \mu_B^2 S_B(-\Delta), \tag{A.5}$$

where $S_B(-\Delta)$ is the power spectral density of $B_\perp(\tau)$. Similarly, if we start with the NV center in state $|1\rangle$, the transition rate is given by

$$\Gamma_{1\to 0} = \frac{1}{4} g^2 \mu_B^2 S_B(\Delta) \tag{A.6}$$

Treating the fluctuating field as a classical variable imposes the condition that $\langle B_\perp(\tau) B_\perp(0)\rangle$ is real and thus $\Gamma_{1\to 0} = \Gamma_{0\to 1} = \Gamma$. For the specific case of the NV center interacting with a bath of Gd^{3+} spins, we assume a telegraph noise spectrum given by

$$S_B(\Delta) = \frac{2\langle B_\perp^2\rangle \gamma}{\gamma^2 + \Delta^2} \tag{A.7}$$

where $\langle B_\perp^2 \rangle$ is the time-averaged magnetic field component, perpendicular to the NV axis, produced at the NV center by the Gd^{3+} spin and $\gamma = 1/T_1^{Gd}$ is the characteristic spectral width (see Fig. 3.3A of Chapter 3) given by the Gd^{3+} relaxation rate.

To calculate the induced relaxation rate in our experiment we must account for the 3-level structure of the NV center and consider the transition rates between levels $|0\rangle$ and $|-1\rangle$ of the ground state manifold. Because our measurements of the relaxation rates are done in earth magnetic field, levels $|1\rangle$ and $|-1\rangle$ are approximately degenerate and we assume that

$$\Gamma_{0\to-1} \approx \Gamma_{0\to1} = \Gamma. \tag{A.8}$$

Accounting for the 3-level structure, the $|0\rangle$ state population evolves in time according to

$$P_0(t) = \frac{1}{3} + \frac{2}{3}e^{-3\Gamma t} = \frac{1}{3} + \frac{2}{3}e^{-\Gamma_{induced}t} \tag{A.9}$$

where the effective induced relaxation rate is $\Gamma_{induced} = 3\Gamma$.

A single fluctuating Gd^{3+} magnetic dipole moment μ a distance r away from the NV center creates the magnetic field $\langle B_\perp^2 \rangle = 4\mu^2/3r^6$. For a Gd^{3+} ion with spin $S = 7/2$, the dipole moment is $\mu = g\mu_B\sqrt{S(S+1)}$.

Combining the above expressions, we obtain the scaling of the NV center sublevel population relaxation rate induced by a single fluctuating Gd^{3+} ion a distance r away:

$$\Gamma_{induced} = 2\frac{S(S+1)g^4\mu_B^4}{r^6}\frac{\gamma}{\gamma^2+\Delta^2}. \tag{A.10}$$

The NV center sublevel population relaxation rate induced by other paramagnetic species (such as other lanthanide ions) can also be calculated using this expression.

A.6 Co-localization simulation

The Monte Carlo simulations of the experiment, shown in Fig. 3.4, were performed as follows. For a random distribution of Gd^{3+} molecules on the diamond surface, the separation between the NV center and the proximal Gd^{3+} molecule was computed, together with the induced NV center relaxation rate. The mean spacing between Gd^{3+} molecules was taken to be 20 nm, to be consistent with the AFM measurements, and the AFM co-localization uncertainty was taken to be 15 nm. The Gd^{3+} electron spin relaxation rate has been measured in a number of MRI contrast agents [77], and depends on several factors, such as the local crystal field environment of the Gd^{3+} ion, and the rotational correlation time for solution-phase measurements. Given the range of values quoted in Ref. [77], this relaxation rate in our experiments is likely to be between 1 and 100 GHz. For the Monte-Carlo simulations we took a value of 10 GHz, which produced the best agreement between the simulation and the data points, as measured by the Kolmogorov-Smirnov Z-statistic test (see below). The simulations contain 10^9 realizations of the experiment. The color scale in Fig. 3.4 (inset) shows the probability density of obtaining a particular NV center relaxation rate for a given measured separation between the NV center and the proximal Gd^{3+} molecule.

In order to quantify the agreement between the experimental data points and the expected Gd^{3+}-induced NV center relaxation, we calculated reduced chi-squared statistic for the experimental data and the model presented in Appendix A.5: $\chi_r^2 = 0.8$. The agreement between the data points and the Monte Carlo simulations is hard to quantify rigorously. A commonly used nonparametric technique is the Kolmogorov-

Smirnov test, which quantifies the discrepancy between two statistical distributions [102]. Whereas this test is not distribution-independent for multivariate datasets, it is still a useful measure of the goodness-of-fit [103]. The value of the two-variable Kolmogorov-Smirnov Z-statistic for the data shown in Fig. 3.4 (inset) is 1.1, which indicates that the data points are consistent with the simulated distribution. The agreement deteriorated when the simulation was done for other values of NV depth, Gd^{3+} relaxation rate, Gd^{3+} molecule spacing, and co-localization uncertainty. We note that the average NV center depth has the largest effect on the simulation results at small radial separations between the NV center and the Gd^{3+} position ($\lesssim 10$ nm).

A.7 Detecting Gd^{3+}-molecules by measuring NV center relaxation

A.7.1 Range of parameters consistent with experimental data

The binned experimental data presented in Fig. 3.4 were consistent with a range of parameters (average NV-center depth, Gd^{3+} relaxation rate, and Gd^{3+} molecule surface concentration). These parameters were strongly constrained by the experimental data in the inset in Fig. 3.4. However, we can argue that the NV center interacts, on average, with a single Gd^{3+} molecule, based solely on the data presented in Fig. 3.4. For each NV center depth, Monte Carlo simulations were performed to determine which values of the Gd^{3+} relaxation rate and surface concentration resulted

in the best least-squares fit to the data shown in Fig. 3.4. These best-fit values are shown as blue points in Fig. A.4.

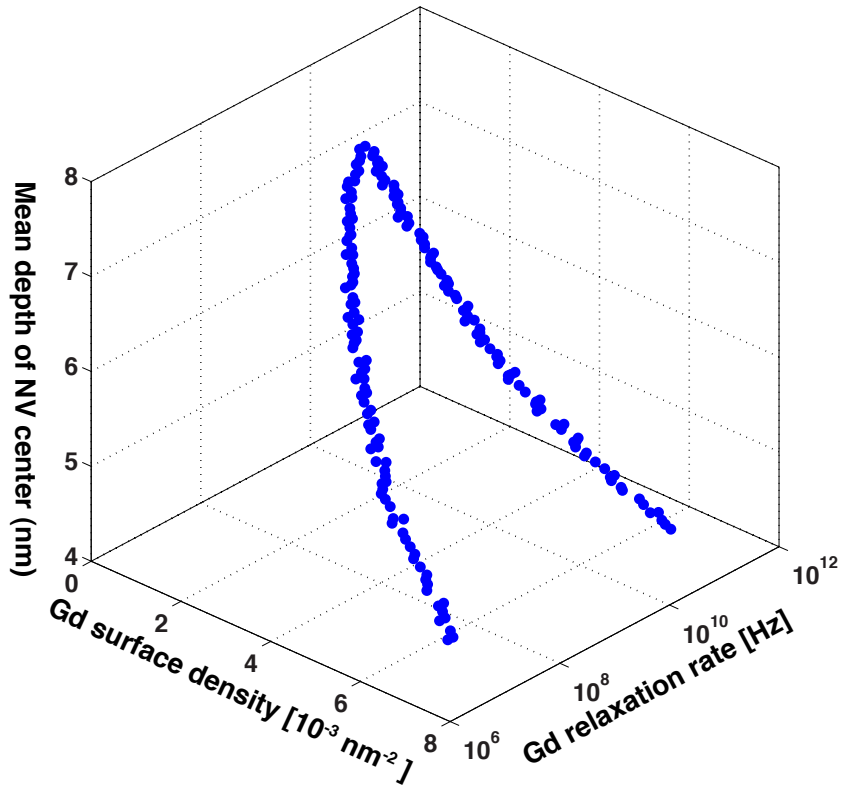

Figure A.4: The range of experimental parameters that are consistent with the data. The points show parameter combinations that are consistent with the measured distribution of Gd^{3+}-induced NV center relaxation rates shown in Fig. 3.4B. All the parameter combinations shown by the points result in $\chi_r^2 < 0.7$.

For NV depths greater than approximately 8 nm, all sets of parameters resulted in chi-squared values greater 5 and are therefore inconsistent with the experimental data. NV center depths less than 4 nm required a Gd^{3+} relaxation rate above 1 THz, well outside the range of values for this rate found in literature. We note that every suitable combination of parameters (every point on the plot) corresponds to a regime where the induced relaxation rate of the NV center is caused by interaction with a

single Gd^{3+} spin (the NV center depth is smaller than the mean spacing between the Gd^{3+} molecules).

A.7.2 Experimental data uncertainty analysis

For the binned experimental data shown in Fig. 3.4, the uncertainties were determined by adding in quadrature the uncertainties resulting from the experimental fitting errors and the bin sampling uncertainties. Each of the 85 measurements (see Fig. 3.3C) was fit with an exponential decay model, yielding the most likely relaxation rate and a one sigma error bar. These errors allow us to determine the probability that a particular measurement lies in a particular histogram bin. We considered all possible ways the 85 measurements can be distributed among the five bins and assign probability values to each distribution. This procedure yielded the most likely number of measurements in each bin and the associated one sigma error bar. Additionally, the probability of getting a particular number of measurements in any bin was related to the stochastic distribution of Gd^{3+} molecules on the diamond surface and was binomially distributed. In particular, given a total of N measurements of the relaxation rate, a bin containing n points would have an associated variance given by $n(1 - n/N)$.

A.7.3 Photon shot noise-limited detection sensitivity

A possible paramagnetic molecule detection strategy would be to monitor NV center fluorescence after optical pumping into the $m_s = 0$ sublevel and a relaxation-in-the-dark period of approximately 2 ms, chosen to be approximately equal to the

NV center intrinsic T_1 time, which we assume to be 5 ms. The photon count rate from a single NV center is typically 5 x 10^4 s^{-1}. With the 300 ns-long APD photon acquisition window, in such an experiment we can detect approximately 8 photons per second. Given the 30% contrast between the "bright" $m_s = 0$ state and the "dark" $m_s = \pm 1$ states, a 300 Hz change in NV relaxation rate (which corresponds to detecting a single Gd^{3+} molecule spin at a distance of 10 nm) would result in a photon "signal" of approximately $0.06N_p$, while the "noise" is approximately $\sqrt{N_p}$, where N_p is the detected number of photons. In order to detect this change in NV center relaxation rate at 3σ confidence level, we need $N_p \approx 2500$ detected photons, which takes approximately five minutes of averaging.

A.8 Control experiments with La^{3+} containing molecules and bare ligand molecules

In order to demonstrate that the surface chemistry had negligible effect on the relaxation rate of the NV center, we attached bare ligand molecules to the diamond surface. We used the same procedure as for the Gd^{3+} molecules [97], except in this case we never included gadolinium into the 1 mM solution of ligand molecules. After attaching the bare ligand molecules to the diamond surface, it was clear that no significant increase in relaxation rate was observed for the 16 relaxation measurements taken, as expected (Figure A.5). Additionally, we attached La^{3+}-containing molecules to the surface of the diamond. We created La^{3+}-containing molecules in the same way we made Gd^{3+} molecules [97], but instead replaced Gd^{3+} with La^{3+} to create a 1

mM solution of La^{3+}-containing molecules. La^{3+} is chemically identical to Gd^{3+}, but it has no unpaired electron spins and thus we expect to see no enhanced relaxation rate. Indeed, we observed no enhanced relaxation rate for the 8 NV center relaxation measurements taken (Figure A.5).

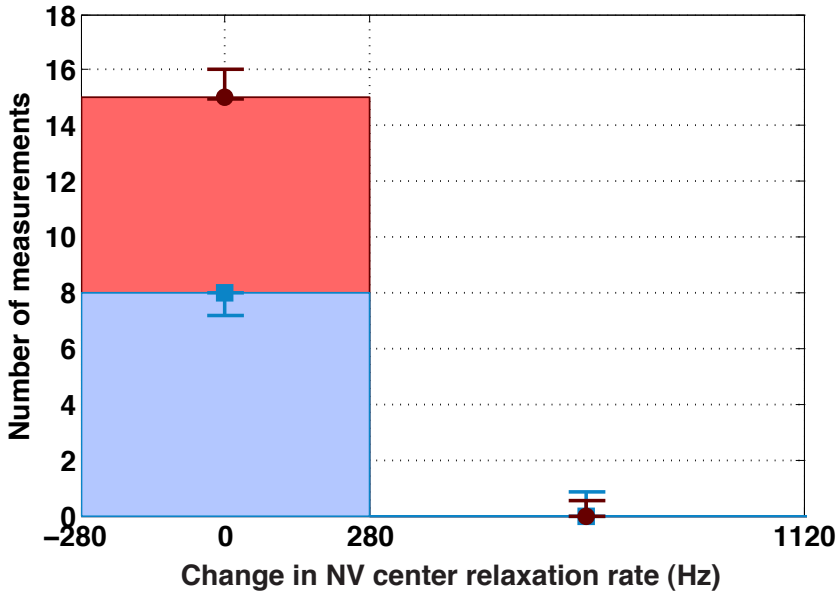

Figure A.5: Control experiments with bare ligand and La^{3+} molecules. Experimental results of 16 NV center relaxation rate measurements with bare ligand molecules covalently attached to the diamond surface (red) and 8 NV center relaxation rate measurements with La^{3+} molecules covalently attached to the diamond surface (blue). Within statistical error, the results are consistent with $\Gamma_{induced} = 0$.

center

Appendix B

Supporting material for Chapter 4

B.1 Materials and Methods

B.1.1 Nano-diamond samples

The samples used in this work were monocrystalline synthetic $0-0.05$ micron diamonds (contained in a diamond slurry) produced by high-pressure, high-temperature (HPHT) synthesis (Microdiamant AG, MSY 0-0.05 GAF). The nano-diamond samples were prepared for measurements by the following procedure: (a) 300 μL of diamond slurry and 700 μL of deionized and distilled water were put into 1.5 mL centrifuge tubes (x8), (b) the 8 tubes were centrifuged at $10,000$ RPM for 45 minutes, (c) the top 800 mL of solution was pipetted out and discarded, (d) 800 mL of deionized and distilled water was pipetted into each tube, (e) the tubes were sonicated for 15 minutes, (f) steps (b)-(e) were repeated an additional 6 times, (g) steps (b)-(e) were repeated 3 times with acetone instead of deionized and distilled water,

(g) steps (b)-(e) were repeated 5 times, (h) the 8 mL of resulting solution (1 mL x 8 tubes) were combined into a single glass centrifuge vial and spun down at $1,000$ RPM for 2 hours, (i) the top 7 mL of solution was removed by pipette, (j) 1 mL of deionized and distilled water was added to the solution, (k) the 2 mL solution was sonicated for 15 minutes, (l) the 2 mL was added to 18 mL of a 3-acid mixture (equal volumes of concentrated H_2SO_4, HNO_3, and $HClO_4$), (m) the 20 mL solution spent 4 hours under reflux conditions, (l) after 2 hours of cooling, the solution was split into 4 centrifuge vials containing 5 mL each, (m) the 4 vials were spun down at $1,000$ RPM for 2 hours, (n) the top 4 mL of each vial were removed, (o) the remaining 4 mL (1 mL x 4 centrifuge vials) were combined into one centrifuge vial, (p) the vial was spun at $1,000$ RPM for 2 hours, (q) the top 3 mL of solution was removed, (r) 3 mL of demonized and distilled water was added to the vial, (s) steps (p)-(r) were repeated an additional 3 times, (t) steps (p)-(q) were repeated, (u) 1 mL of deionized water was added to the vial.

The nano-diamonds were prepared for optical interrogation by depositing them onto a No. 0 glass coverslip (Ted-Pella, Inc, #260320). The following procedure was used for deposition: (a) No. 0 glass coverslip was cut to the appropriate length for our optical setup using a diamond cutter, (b) the coverslip with was rinsed with acetone, (c) the coverslip was rinsed with isopropanol, (d) the coverslip was rinsed with deionized and distilled water, (e) the coverslip was dried using an N_2 gun, (f) the coverslip was plasma cleaned for 10 minutes, (g) 20 μL of the prepared nano-diamond solution (as prepared above) was pipetted onto the coverslip, (h) the coverslip was left to dry overnight (approximately 12 hours), (i) the coverslip was mounted onto

our home-built mount using tape and silver paint (the latter for increased stability).

B.1.2 Optical setup

The optical setup used to optically polarize and read out the NV centers was a home-built scanning confocal microscope. The No. 0 glass coverslip was placed on top of an inverted Nikon Plan Fluor 100x oil immersion objective (NA = 1.3), with the nano-diamonds facing upwards. This objective was used to focus light from a 532 nm laser (Information Unlimited, MLLIII532-200-1), which in turn was used to optically polarize and read out the NV center electronic spin state. This laser was switched on and off using an acoustic-optic modulator (Isomet Corporation, 1250C-974) in a double-pass configuration. The vertical position of the oil immersion objective was controlled by a piezeoelectric scanner (Physik Instrumente, P-721 PIFOC), while the lateral position of the laser focus was controlled by a closed-loop scanning galvanometer (Thorlabs, GVS012). The NV center fluorescence was filtered using a 532 nm notch filter (Semrock, NF03-532E) and a 633 nm long-pass filter (Semorck, LP02-633RU). Finally, the fluorescence was collected using an avalanche photodiode (PerkinElmer, SPCM-AQRH-14-FC). The acousto-optic modulator and avalanche photodiode were controlled using TTL voltage pulses from a 400 MHz PulseBlasterESR-PRO pulse generator (Spincore Technologies, PBESR-PRO-400). The piezoelectric scanner and galvanometer were controlled by a multifunction data acquisition unit (National Instruments, NI PCI-6229).

B.1.3 Microwave setup

The microwave-frequency fields used to determine the optically detected magnetic resonance (ODMR) of the NV center in Fig. B.1 was generated by a Rohde & Schwartz SMC100A signal generator. The pulses were formed by a switch (Mini-Circuits ZASWA-2-50DR+) that was controlled using the TTL pulses from the PulseBlasterESR-PRO. These microwave pulses were amplified by a power amplifier (Mini-Circuits ZHL-16W-43-S+) and delivered to the NV centers via a coplanar waveguide (fabrication described below). The coplanar waveguide was mounted onto a home-built mount with two SMA connectors on either side; the waveguide was connected to the SMA connectors using colloidal silver liquid (Ted Pella #16031).

B.1.4 Coplanar waveguide fabrication

The coplanar waveguide used to deliver the microwave-frequency fields were fabricated on a No. 0 glass coverslip (Ted-Pella, Inc, #260320) by the following procedure: (a) rinse the coverslip with acetone, (b) rinse the coverslip with methanol, (c) rinse the coverslip with deionized water, (d) dry the coverslip with an N_2 gun, (e) deposit 50 nm of titanium (adhesion layer), (f) deposit 1 μm of copper (conductance layer), (g) deposit 400 nm of gold (conductance layer), (h) coat the coverslip with Shipley S1813 positive photoresist, (i) expose the resist using a SUSS MicroTech MJB4 mask aligner using a mask with gaps of 70 μm and central conductor of width 2 mm, (j) develop the Shipley S1813 using Microposit MF CD-26 for 2.5 minutes, (k) etch the exposed metal using gold etchant (Transene, TFA) for 4 minutes followed by Buffered Oxide Etch (7:1)) for 5 seconds, (l) rinse with acetone to remove the

unexposed resist, (m) rinse with deionized water, (n) dry with N_2 gun, (o) coat with 20 nm of aluminum oxide (Al_2O_3) using atomic layer deposition (Cambridge NanoTech S200) to prevent the nano-diamonds from coming into contact with the metal. The depositing of the titanium, copper, and gold were done using a Sharon Thermal Evaporator.

B.1.5 Distinguishing single NV centers

We conduct optically-detected magnetic resonance (ODMR) measurements to confirm that the surface-treated nano-diamonds we performed measurements on contain mostly individual NV centers rather than ensembles. The initialization, manipulation, and readout of the electronic ground state of the NV center is possible due to its electronic level structure (Fig. 4.1B, inset) [26]. We first initialize an NV center into the $m_s = 0$ sub-level and detect the spin-dependent fluorescence after driving spin flips with a microwave-frequency field. Sweeping the carrier frequency of the drive field yields the ODMR spectrum. A typical zero-field spectrum is shown in Fig. B.1 (top panel). When we apply an external magnetic field, we observe a pair of Zeeman-shifted resonances (Fig. B.1, bottom panel) corresponding to the $m_s = \pm 1$ spin sub-levels. Since the Zeeman splitting of an NV center depends on the orientation of its symmetry axis with respect to the external field, we expect the ODMR spectrum of an ensemble of NV centers to exhibit broad resonances with low ODMR contrast. On the contrary, the observed spectrum exhibits no inhomogeneous broadening expected for an ensemble of randomly-oriented NV centers while the ODMR contrast is consistent with that of the zero-field spectrum, confirming the presence of

an individual NV center.

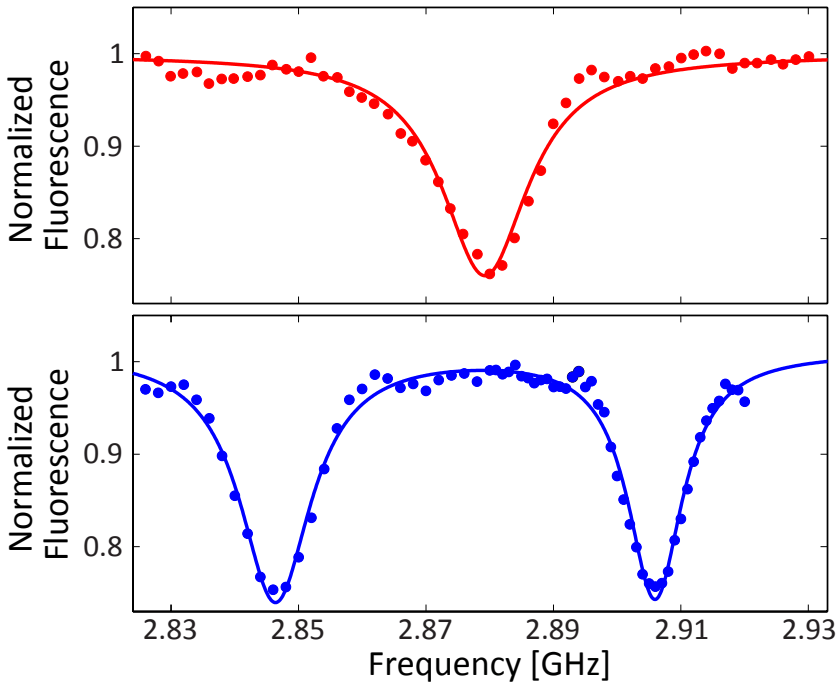

Figure B.1: Optically-detected magnetic resonance (ODMR) of an NV center in a nano-diamond. At zero magnetic field, the the $m_s = \pm 1$ states are not resolvable (top panel). In the presence of a small magnetic field, the $m_s = \pm 1$ become resolvable (bottom panel) and their narrow width demonstrate that this is a single NV center.

B.1.6 $GdCl_3$ and $LaCl_3$ solutions

To create the $GdCl_3$ solutions, we immersed approximately 0.5 mmol of gadolinium (III) chloride hexhydrate (Sigma Aldrich, 203289) into 5 mL of water to form a 100 mM solution. This solution was then diluted six times by a factor of ten to make 10 mM, 1 mM, 100 μM, 10 μM, 1 μM, and 100 nM concentrations of $GdCl_3$. The same process was done for the $LaCl_3$ solution, except we instead used lanthanum chloride heptahydrate (Sigma Aldrich, 203521).

B.2 Additional Single Gd^{3+} Detection Result

We performed the experiment shown in Fig. 3B a total of 5 times, and 3 times we observed signatures of discrete steps corresponding to single Gd^{3+} ions adsorbing to the nano-diamond surface. The data and fit for the experiment that demonstrated these signatures, but is not shown in the main text (the other 2 data sets are in Fig. 4.3A (middle panel) and Fig. 4.3B), is shown in Fig. B.2.

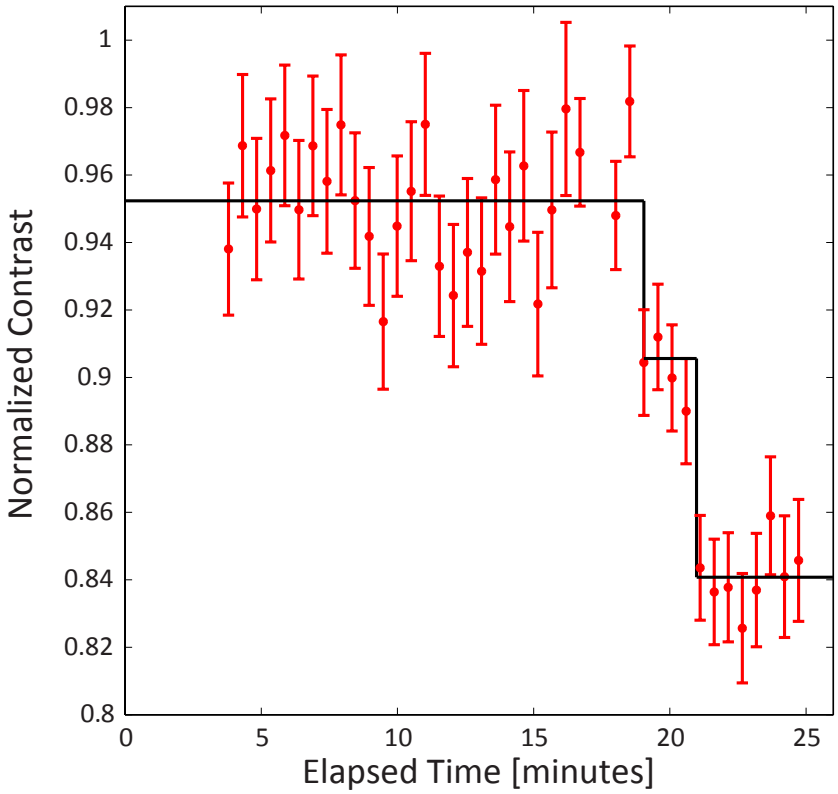

Figure B.2: Time-resolved sensing of the adsorption of single Gd^{3+} ions onto the nano-diamond surface using a single delay time, $\tau = 100$ μs, of the relaxation curve. At time 0, 100 nM of $GdCl_3$ was pipetted on top of the nano-diamond being observed. Black curve is a numerical fit to the red data points using a model which assumes discrete Gd^{3+} attachment events.

Appendix C

Magnetic resonance detection of individual proton spins using quantum reporters

C.1 Introduction

Nuclear magnetic resonance and magnetic resonance imaging are essential tools for both the physical and life sciences [10,104], but have been limited to the detection of large ensembles of spins due to their low sensitivity [105,106], or the macroscopic nature of sensors [23,25]. Over the past decades, significant efforts [21,22,68,74,75] have been directed toward pushing this sensitivity to its ultimate physical limit, the detection of individual nuclear spin signals localized in a small volume. Our approach to magnetic sensing and imaging makes use of electronic spin-1/2 qubits on the surface of a high purity diamond crystal, coupled to a nearby single nitrogen vacancy (NV)

color center a few nanometers below the diamond surface (Fig. C.1a) [107]. Clean {100} diamond surfaces in ambient conditions are known to host stable electron spins with $S = 1/2$ and a g-factor of 2 [108, 109]. These spins have been considered to be deleterious because they are thought to cause decoherence of NV electronic spins within a few nanometers of the diamond surface [110, 111]. However, with proper quantum control, the surface electron spins can be turned into a useful resource. They can be coherently manipulated and measured, thereby forming a network of quantum "reporters" [112,113] that probe and report the local magnetic environment. The key advantage of such surface spins is their proximity to sensing targets in samples placed on or near the diamond surface. As suggested in recent theoretical work [107], surface electron spins coupled to NV centers can also effectively "amplify" small magnetic field signals, allowing for sub-nanometer localization of individual nuclear spins.

C.2 Characterization of the surface quantum reporter spin network

To measure the quantum states of surface electron reporter spins through the NV-reporter magnetic dipole interaction, the nearby shallow NV center is initialized into the $m_s = 0$ sublevel using an optical pumping laser pulse at 532 nm; the spin states of the NV center and of the reporter spins are independently manipulated using pulsed magnetic resonance frequencies, and the final quantum state of the NV center is measured using its spin-state-dependent fluorescence (Fig. C.1b). The $m_s = 0 \leftrightarrow m_s = -1$ NV spin transition is addressed at the angular frequency

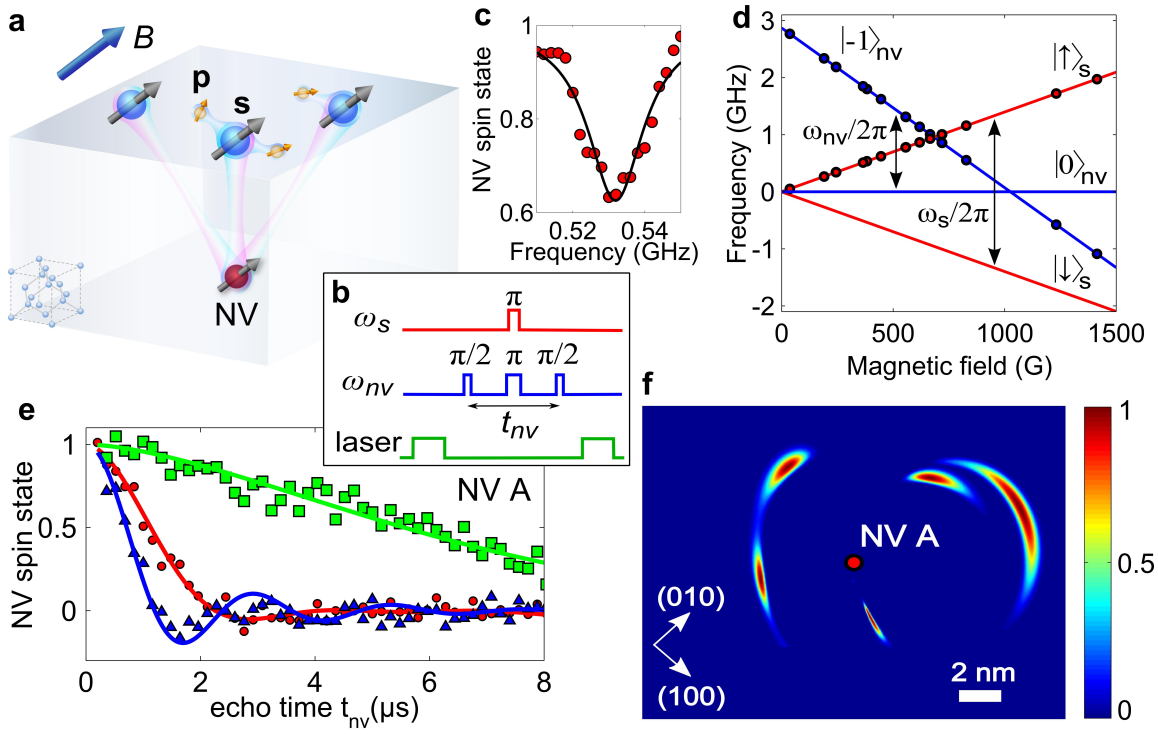

Figure C.1: Characterization of surface reports spins using a shallow NV center. (a) Schematic of a network of reporter electron spins s on the surface of a diamond crystal, that can be used to detect and localize surface proton spins p. (b) DEER pulse sequence. (c) Measured DEER signal as a function of reporter spin frequency ($\omega_s/2\pi$) for fixed $t_{\rm NV}$. (d) Measured and calculated Zeeman shifts of NV (blue) and reporter (red) spin states. (e) Results of DEER experiment with varying echo delay time $t_{\rm NV}$. Green squares and line: NV center spin echo decay data and fit. Red circles: DEER measurements. Blue triangles: DEER measurements after oxidizing acid treatment. Red and blue lines are fits using a model with positions of reporter spins on the diamond surface as fitting parameters. In this and subsequent figures, spin state populations are scaled to range between -1 and +1. (f) Probability density map for surface reporter spins near NV A (depth (3.3 ± 0.2) nm), marked by the red dot. Arrows mark diamond crystallographic axes; NV center is aligned along {111}.

$\omega_{nv} = \Delta - \gamma_e B$, and the $m_s = +1/2 \leftrightarrow m_s = -1/2$ surface reporter spin transition is driven at frequency $\omega_s = \gamma_e B$. Here, $\Delta = 2\pi \times 2.87$ GHz is the NV zero-field splitting, B is the magnitude of the static magnetic field applied along the NV axis,

and $\gamma_e = 2\pi \times 2.8$ MHz/G is the electron gyromagnetic ratio (Figs. C.1c and C.1d).

The magnetic dipole coupling between the NV center and the surface electron reporter spins is characterized using a generalized spin echo (double electron-electron resonance or DEER) sequence, shown in Fig. C.1b. Figure C.1e shows that for one typical shallow NV center (NV A) the measured spin echo decays on a time scale $T_2^{(nv)} \approx 5$ μs (Fig. C.1e). However, when a π pulse flips the surface reporter spin population simultaneously with the NV center π pulse, the NV-reporter magnetic dipole interaction causes NV spin echo collapse (Fig. C.1e, red circles), with a form that depends on the locations of the surface spins around the NV center. Because the magnetic dipole interaction is long range, the NV center can be coupled to multiple surface reporter spins, with the coupling strengths dependent on their positions on the diamond surface. When we treat the diamond with a strongly oxidizing reflux mixture of concentrated nitric, sulfuric, and perchloric acids (see Appendix D), and repeat the DEER experiment on the same NV center, the DEER signal is clearly modified (Fig. C.1e, blue triangles), suggesting that this surface treatment "resets" the positions of the electron reporter spins and confirming that they indeed reside on the diamond surface.

To determine the reporter spin positions, we repeat the DEER measurements while changing the direction of the applied magnetic field $\boldsymbol{B}$. The magnetic dipole interaction between the NV center and a surface spin depends on their separation and the angle that the vector between them makes with the vector $\boldsymbol{B}$. By rotating $\boldsymbol{B}$, we change this angle, and thus the strength of this interaction (similar methods have been employed to localize ^{13}C spins and other NV centers inside the diamond

lattice [56, 114]). By combining the results of the DEER experiments at 7 different magnetic field angles, we reconstruct the positions of the 4 reporter spins, constrained to be on the diamond surface, that are nearby to NV A. The positions of these 4 reporter spins relative to NV A are shown in Fig. C.1f, where the color scale represents the reporter spin position probability density (normalized to unity), corresponding to the best-fit chi-squared statistic, performed with each reporter spin position fixed at the associated map coordinate (see Appendix D). In particular, the surface reporter spin closest to the NV center can be localized with nanometer-level uncertainty.

C.3 Coherent control and dynamics of the reporter spins

The DEER pulse sequence is a useful tool for characterizing the surface reporter spins on the diamond surface, but it is limited by the decoherence time of the shallow NV center $T_2^{(nv)}$, which is usually on the order of several microseconds. In order to manipulate and probe the reporter spins on time scales longer than $T_2^{(nv)}$, we implement a new "reporter pulse sequence", shown in Fig. C.2a, inset. This protocol, inspired by Ramsey interferometry in atomic physics [115], consists of two "probe" segments, in which the NV center probes the quantum state of the reporter spin network, separated by an "evolution" segment, in which this state can be manipulated. In essence, this protocol enables the comparison of the reporter-spin quantum states before and after the evolution segment. Importantly, the duration of the evolution segment is limited by the NV center $T_1^{(nv)}$ time (typically milliseconds), rather than

its $T_2^{(nv)}$, thereby extending the evolution timescale by orders of magnitude [116]. In the measurements described below, the duration of the probe segments is kept short (≈ 0.9 μs) to ensure that the NV readout signal is dominated by the coupling to the proximal (most strongly coupled) reporter spin (see Appendix D).

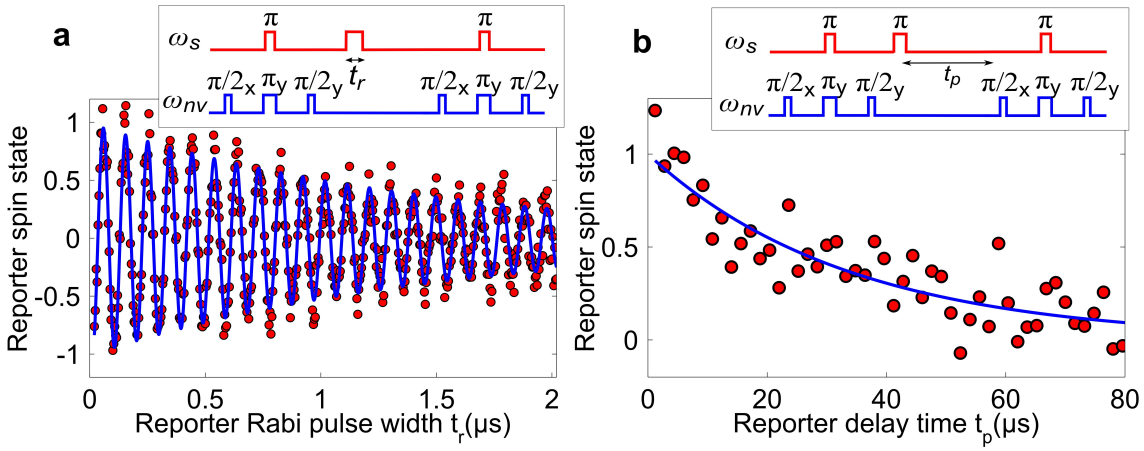

Figure C.2: (a) Coherent control of reporter spins. Rabi oscillations between spin states with a variable-width pulse (red points) with an exponentially damped fit (blue line). Inset: RF pulse sequence. (b) Population relaxation dynamics of the reporter spins (red points) with an exponential decay fit (blue line). Inset: RF pulse sequence.

To demonstrate coherent control of the surface reporter spins, we vary the length of the radiofrequency (RF) pulse applied at the reporter spin resonance frequency, as shown in Fig. C.2a. We observe Rabi oscillations with decay time of ≈ 1 μs, which is much longer than the reporter-spin Rabi period, indicating that the pulses can be used for coherent control of the reporter spins. Next, the population relaxation time $T_1^{(s)}$ of the surface spin network is measured by varying the delay time t_p between the two probe segments in the pulse sequence, Fig. C.2b. The extracted value of $T_1^{(s)} = (29.4 \pm 2.3)$ μs can be used to place a lower limit of ≈ 5 nm on the mean separation between the surface reporter spins: if they were closer together, their

mutual magnetic dipole flip-flop interaction would give rise to a shorter population relaxation time (see Appendix D). Note that this observation is consistent with the reconstructed spin locations shown in Fig. C.1f.

C.4 Detection of the magnetic field created by protons using reporter spins

We next use the reporter electron spins to perform measurements of the magnetic fields on the diamond surface, using the RF pulse sequence shown in Fig. C.3a. The time-varying magnetic field at the site of a reporter spin gives rise to a phase shift during its spin echo precession time t_s, which is converted to a change in its spin state population, and is then detected by the NV center. By varying the time t_s, we implement a frequency filter, whereby the measurement is sensitive to magnetic field Fourier components at angular frequencies ω on the order of $2\pi/t_s$, showing up as reporter spin echo collapses at delay times $t_s = 2\pi k/\omega$, where $k = 1, 3, ...$ [68]. The experimental data exhibit collapses and revivals characteristic of a time-varying magnetic field created by nuclear spins on the diamond surface, precessing in the applied magnetic field B with Larmor frequency $\omega_n = \gamma_n B$, where γ_n is the nuclear spin gyromagnetic ratio. Figure C.3a shows example results for a particular NV center (NV A), and the data are consistent with the reporter spin coupled to an oscillating magnetic field created by surface protons with root-mean-squared amplitude of $B_n = 0.3$ G and angular frequency of $\omega_n = 10.6\ \mu\text{s}^{-1}$. In order to determine the nature of these nuclear spins, we repeat the measurements and analysis at several magnetic fields,

and find that the reporter spin echo modulation frequency scales with the applied magnetic field in agreement with the proton gyromagnetic ratio of $2\pi \times 4.26$ kHz/G (Fig. C.3b, blue points).

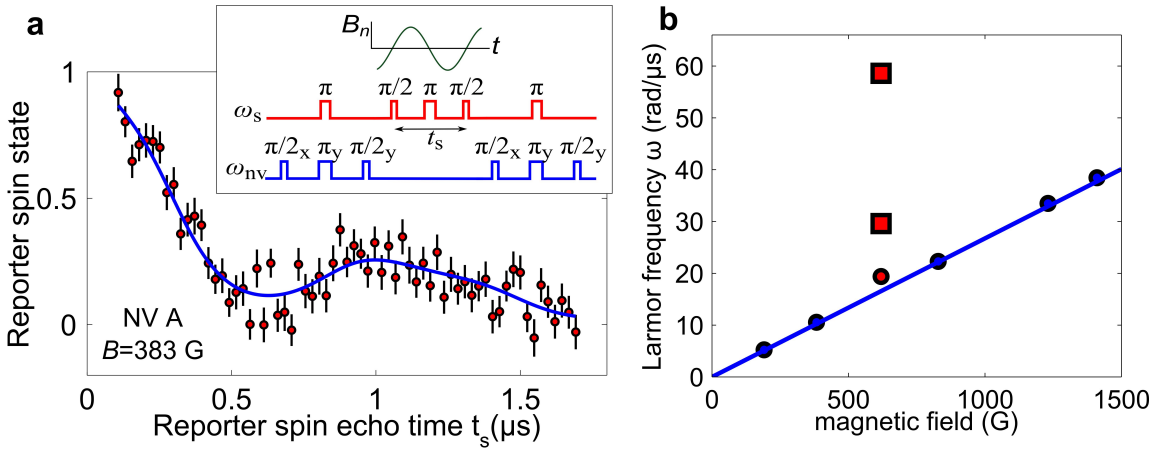

Figure C.3: Detection of the magnetic field created by protons, using the surface electron reporter spins. (a) Measurement with NV A of the reporter spin echo modulation at $B = 383$ G (red points), fit with a model for echo modulation of a reporter spin coupled to a nuclear spin bath (see Appendix D) (fit shown by blue line, reduced chi-squared value is 1.2). The error bars on this and subsequent plots show standard deviations of the data points obtained from averaging approximately 5 million repetitions of the pulse sequence, and are consistent with photon shot noise. Inset: reporter echo pulse sequence. (b) Measured values for ω_n at 5 different settings of the applied static magnetic field (blue points), consistent with the proton gyromagnetic ratio of $2\pi \times 4.26$ kHz/G (blue line). The red points mark the ω_n, ω^-, and ω^+ oscillation frequencies, see text.

C.5 Coherent dynamics between individual reporter and proton spins

Remarkably, however, this simple scaling is not observed at all values of the magnetic field. For example, the data taken with NV A at the magnetic field of 619 G

show modulation at frequencies very different from the Larmor frequency expected for the coupling of the reporter spin with a semiclassical proton spin bath (Fig. C.3b, red points). This high-frequency modulation, seen in the data plotted in Fig. C.4a, indicates the presence of coherent dynamics between the reporter and proximal proton spins. In order to reproduce and further explore this coherent coupling, another NV center (NV B) is studied at a similar magnetic field. The experimental points, shown in Fig. C.4b, again display strong modulation, crossing the abscissa axis. This signals coherent population transfer between the proton spin states, mediated by the interaction with a single reporter spin, which cannot occur in the absence of reporter-proton entanglement.

To understand these observations, we analyze the coherent dynamics of a reporter electron spin interacting with proximal proton spins on the diamond surface. The hyperfine interaction between them can be described by the Hamiltonian $H = \hbar a J_z I_z + \hbar b J_z I_x$, where J is the spin operator of the reporter spin, I is the nuclear spin operator, and the z-axis is along the applied magnetic field [117] (see Appendix D). This Hamiltonian can be interpreted as an effective hyperfine field, created by the reporter spin at the site of the proton spin (Fig. C.4c), which in turn gives rise to splitting of the reporter electron spin states, $\omega^{\pm} = \sqrt{(\pm a/2 - \omega_n)^2 + b^2/4}$, as shown in Fig. C.4d. This level splitting causes reporter spin echo modulation at frequencies ω^+ and ω^-, with the modulation depth scaling as $2b\omega_n/\omega^+\omega^-$ [117]. When the proton Larmor frequency ω_n is close to half of the hyperfine interaction strength, the reporter spin echo signal is strongly modulated at ω^+ and ω^-, whereas the signal modulation decreases when ω_n is substantially different from a, b. Data taken at such

off-resonance magnetic fields can, within their signal-to-noise ratio, be successfully described with a semiclassical nuclear spin bath model (see Appendix D).

To analyze the experimental data quantitatively, we compare our measurements with a model that includes coherent hyperfine coupling of a reporter electron spin with a proximal proton, as well as the semiclassical spin bath of protons on the diamond surface (see Appendix D). For NV A, the fit to the experimental data shown in Fig. C.4a yields spin echo modulation frequencies of $\omega^+ = 30\ \mu\text{s}^{-1}$ and $\omega^- = 59\ \mu\text{s}^{-1}$, shown as red squares in Fig. C.3b, from which we extract hyperfine coupling parameters $a = (66 \pm 18)\ \mu\text{s}^{-1}$ and $b = (52 \pm 20)\ \mu\text{s}^{-1}$. Both the point magnetic dipole interaction and the contact hyperfine interaction contribute to the parameters a and b: $a = a_0 + (\hbar\gamma_e\gamma_n/r_n^3)\,(1 - 3\cos^2\theta_n)$, and $b = (\hbar\gamma_e\gamma_n/r_n^3)\,(3\cos\theta_n \sin\theta_n)$, where a_0 is the contact hyperfine interaction, r_n is the separation between the reporter spin and the proton spin, θ_n is the angle that the vector between them makes with the applied magnetic field (see Appendix D). The low chemical reactivity of the reporter spins (see discussion below) suggests that the direct overlap between the reporter spin wave function and a surface proton is likely minimal, implying that the magnitude of a_0 is small. If we neglect a_0, the position of the proximal proton with respect to the reporter spin most strongly coupled to NV A is $r_n = (2.2 \pm 0.2)$ Å and $\theta_n = (26 \pm 15)^\circ$, with the azimuthal angle not quantified by the data. The data for NV B (Fig. C.4b) are consistent with the presence of two proximal protons, coherently coupled to the reporter spin: their best-fit positions are $r_n^{(1)} = (2.6 \pm 0.2)$ Å, $\theta_n^{(1)} = (47 \pm 3)^\circ$ and $r_n^{(2)} = (3.2 \pm 0.2)$ Å, $\theta_n^{(2)} = (19 \pm 4)^\circ$, as shown in Fig. C.4e in a probability density map. In order to quantify the uncertainty in the proton positions due to our lack of

information about the magnitude of the contact interaction, we use 40 μs^{-1} as the range of possible values for a_0, since this is the measured contact hyperfine interaction with the OH-group proton in a hydroxylated carbon-centered radical [118], similar to our presumed bonding configuration (see below). For this range of a_0, the locations of the detected protons are constrained to be within the contours shown in Fig. C.4e. We note that in diamond a_0 is likely to be much smaller due to positive electron affinity of the oxidized diamond surface.

While the origin of the reporter spins cannot be unambiguously determined from this study alone, they are likely unsaturated (or "dangling") bonds, localized near the top two carbon atom layers. We observe that they are stable in ambient conditions over time scales of many days, which indicates that they are sterically protected from direct chemical reactions with species outside the diamond lattice. Nevertheless, the reporter spins are close to the surface, since they experience strong hyperfine coupling with surface protons, and their positions change when exposed to the strongly oxidizing 3-acid mixture (this surface treatment also modifies the results of the reporter echo experiments, see Appendix D). Furthermore, they are absent from the diamond surface (no DEER signals) after the diamond is annealed at 465°C in an O_2 atmosphere [51] (see Appendix D). The detected protons are likely from covalently bound hydroxyl (OH) and carboxyl (COOH) groups terminating the clean diamond surface under ambient conditions [119]. Their relative locations are consistent with density-functional-theory calculations of these groups on an oxidized diamond surface [120].

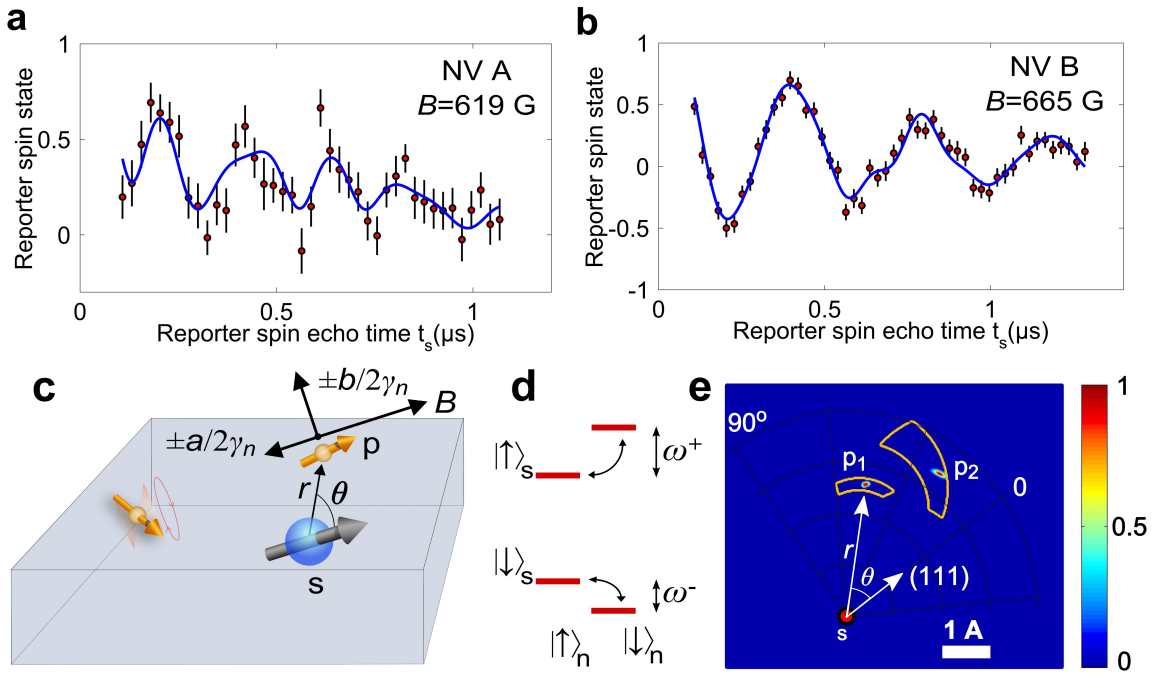

Figure C.4: Coherent dynamics between individual surface electron and proton spins. (a) Reporter spin echo modulation for NV A at $B = 619$ G (red points), and fit using a model with the reporter qubit, proximal to the NV center, coupled to one proton spin (blue line). (b) Reporter spin echo modulation with NV B at $B = 665$ G (red points). The best-fit (blue line, reduced chi-squared value of 1.1) corresponds to a model with the reporter qubit, proximal to the NV center, coupled to two proton spins. (c) Schematic illustrating hyperfine coupling between the reporter electron spin s and the proton spins (gold arrows). The weakly coupled protons far from the reporter spin precess in the applied magnetic field B at the Larmor frequency. The proximal proton spin p experiences the vector sum of B and the effective hyperfine fields $\pm a/2\gamma_n$ and $\pm b/2\gamma_n$, whose signs depend on the reporter spin state. (d) Energy level diagram for the coupled system of the reporter spin and proximal proton spin. (e) Localization of the two proximal proton spins (p_1 and p_2) relative to the reporter spin s, that is most strongly coupled to NV B. The color scale shows the probability density for each proton location, extracted from a fit to the data shown in (b) (see Appendix D).

C.6 Conclusions and outlook

NV centers in diamond have emerged as a nanoscale magnetic-field sensor with exquisite sensitivity under ambient conditions [68–70], enabling magnetic sensing

and imaging of single electron spins [71, 90, 121] and nanoscale ensembles of nuclear spins [74,75,122,123]. Our method extends these recent advances into a new domain, enabling magnetic resonance detection and imaging on surfaces with single nuclear spin resolution. Several paths towards further improving the sensitivity and the broad applicability of our approach should be noted. It may be possible to extend the reporter spin coherence times using decoupling pulse sequences, together with dilution of the proton magnetic moments on the diamond surface, e.g. by deuteration. Individual addressing of the reporter spins may be achievable with a careful choice of the duration of the "reporter pulse sequence" readout intervals, as described above, or via frequency separation of different reporter qubits using a practical magnetic field gradient (less than 1 G/nm) [109]. Polarization transfer from the NV center to the reporter spins [124], and possibly to strongly coupled surface nuclear spins, may allow initialization and entanglement of the surface spin network [125] and hyperpolarization of target nuclei. The hyperfine field gradient, produced by the reporter spins, may also be used to encode spatial information for magnetic imaging. Finally, other reporter spin candidates, such as stable nitroxide radicals, can be explored, possibly providing a more flexible route for sensing applications because they can be directly attached to a reactive site of interest on a molecule under study.

Our approach, with improvements in the coherence properties and robust control of the reporter spins, can enable a number of unique applications. Nuclear magnetic resonance and magnetic resonance imaging of individual molecules and proteins under ambient conditions is one direction that can be pursued. Reporter-based sensing may also find applications in measurements of magnetic fields near complex materials, such

as superconductors and topological insulators. Beyond applications in sensing and imaging, our approach provides a powerful new platform for coherent manipulation of coupled electronic and nuclear spins on surfaces or in 2D materials, which can be used to realize and explore new classes of self-assembled quantum systems [126].

Appendix D

Supporting material for Appendix C

D.1 Materials and measurement apparatus

D.1.1 Diamond sample

The sample used in this work is a polished, single-crystal electronic grade diamond grown by chemical vapor deposition (Element Six), containing substitutional nitrogen and boron in concentrations less than 5 parts per billion (ppb) and 1 ppb respectively. Prior to implantation, the {100} diamond surface was etched approximately 2 μm, using an Ar-Cl_2 plasma etch (25 sccm Ar, 40 sccm Cl_2, ICP RF 400 W, bias RF 250 W, duration 150 s), followed by an O_2 plasma etch (30 sccm O_2, ICP RF 700 W, bias RF 100 W, duration 150 s). Nitrogen implantation was done by INNOViON Corporation using a $^{15}N^+$ dosage of 10^9 cm^{-2} and an implantation energy of 2.5 keV. The implanted diamond was annealed in vacuum using the following procedure: (a) 6 hour ramp to 400°C, (b) 6 hours at 400°C, (c) 6 hour ramp to

800°C, (d) 8 hours at 800°C and (e) 6 hour ramp to room temperature. After annealing, the diamond was cleaned in a 3-acid mixture (equal volumes of concentrated H_2SO_4, HNO_3, and $HClO_4$) for two hours under reflux conditions. The same cleaning procedure was used to re-set the locations of the reporter spins on the diamond surface.

D.1.2 Optical setup

A home-built scanning confocal microscope was used to optically address and read out single NV centers. An RF transmission line was fabricated on the surface of a glass coverslip, and the diamond was placed NV-side down on top of this coverslip. The inverted Nikon Plan Fluor 100x oil immersion objective (NA = 1.3) was positioned under the coverslip. Its vertical position was controlled with a piezoelectric scanner (Physik Instrumente P-721 PIFOC) and the lateral position of the laser beam focus was controlled with a closed-loop scanning galvanometer (Thorlabs GVS012). Optical excitation was performed with a 532 nm laser (Information Unlimited, MLLIII532-200-1) modulated with an acousto-optic modulator (Isomet Corporation, 1250C-974) in a double-pass configuration. NV center fluorescence was filtered with a 532 nm notch filter (Semrock, NF03-532E) and a 633 nm long-pass filter (Semorck, LP02-633RU) and collected using a single-photon counting module (PerkinElmer, SPCM-AQRH-14-FC). The acousto-optic modulator and the single-photon counting module were gated using TTL pulses produced by a 500 MHz PulseBlasterESR-PRO pulse generator from Spincore Technologies. Typical NV center fluorescence count rate was 20 kHz, and photon counter acquisition window for

each sequence repetition was 500 ns.

D.1.3 RF setup

The RF tones, used to address the NV centers and the surface reporter spins, were generated by two Stanford Research SG384 signal generators. The IQ modulation inputs were used to control the x and y quadrature amplitudes of the generator that addressed the NV center. The RF pulses in each channel were generated by the switches (MiniCircuits ZASWA-2-50DR+), controlled by the TTL pulses from the PulseBlasterESR-PRO, and power boosted by an amplifier (three amplifiers were used, depending on the frequency: MiniCircuits ZHL-20W-13+, ZHL-30W-252-S+, and ZHL-16W-43-S+). The two RF channels were combined using an MCLI PS2-109 power splitter, and coupled into the 50 Ω-terminated RF transmission line with the diamond sample on top.

D.2 NV centers and depth measurements

The DEER experiments were performed on a total of 16 NV centers. 12/16 showed clear DEER collapse due to reporter spins, on the time scale shorter than their $T_2^{(nv)}$, 2/16 showed DEER collapse on the order of $T_2^{(nv)}$, and 2/16 showed no DEER collapse. NVs A and B were selected for their fastest DEER collapse, which likely means they are among the most shallow of the NV centers. Reporter sequence experiments were performed only with NVs A and B.

The depths of each of these two NV centers were determined by covering the diamond surface with immersion oil, and measuring the amplitude of the magnetic

field created at the location of the NV center by the immersion oil proton magnetic moments, precessing at the Larmor frequency. The dynamical decoupling XY-k sequence was used to perform this ac magnetometry experiment, see data shown in Fig. D.1. The details of the measurement and fitting procedure are described in a manuscript in preparation [127]. This method yielded the following depths: NV A $\rightarrow (3.3 \pm 0.2)$ nm, and NV B $\rightarrow (3.6 \pm 0.3)$ nm.

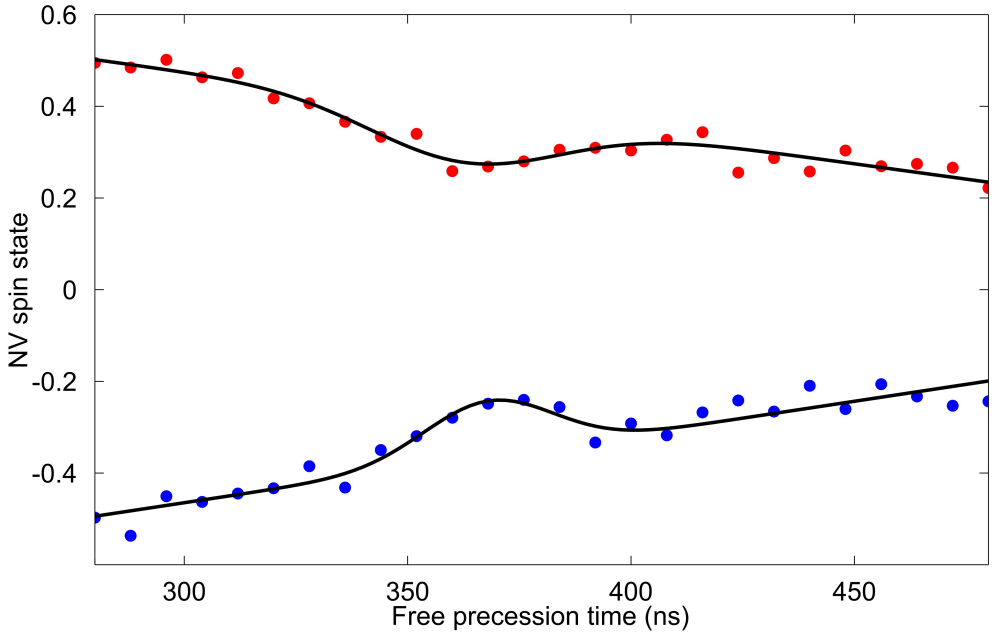

Figure D.1: The results of dynamical decoupling experiment (XY-16 pulse sequence) on NV A, from which we extract its depth.

When a separate diamond sample, with an unpolished surface, implanted and annealed with the same parameters as the one used in our work, was treated at 465°C in an O_2 atmosphere [51], we found that the DEER signals were absent for 11 out of the 12 NV centers for which measurements were taken, and one NV center showed a "weak" DEER signal with the DEER collapse on the order of NV decoherence time

$T_2^{(nv)}$. We concluded that this treatment removed the reporter spins from the diamond surface.

D.3 Localizing reporter spins on the diamond surface

D.3.1 The double electron-electron resonance experiment

The strength of the magnetic dipole coupling between the NV center and the surface spin network was characterized using the double electron-electron resonance (DEER) pulse sequence.

The dipole-dipole interaction Hamiltonian between the NV center spin $\boldsymbol{S}$ and the surface reporter spin $\boldsymbol{J}$ is:

$$H_d = \frac{\hbar^2\gamma_e^2}{r_s^3}\left[\boldsymbol{S}\cdot\boldsymbol{J} - 3\frac{(\boldsymbol{S}\cdot\boldsymbol{r}_s)(\boldsymbol{J}\cdot\boldsymbol{r}_s)}{r_s^2}\right], \tag{D.1}$$

where $\boldsymbol{r}_s$ is the vector from the NV center to the reporter spin. When the magnetic field B is aligned with the NV center axis, we can neglect all non-secular terms, and consider only the terms that commute with S_z and J_z:

$$H_d = \frac{\hbar^2\gamma_e^2}{r_s^3}\left(1 - 3\cos^2\theta_s\right) S_z J_z = \hbar k_s S_z J_z, \tag{D.2}$$

where θ_s is the angle that vector $\boldsymbol{r}_s$ makes with the magnetic field, and the coupling strength is

$$k_s = \frac{\hbar\gamma_e^2}{r_s^3}\left(1 - 3\cos^2\theta_s\right). \tag{D.3}$$

The NV center $|m_s = 0\rangle$ state population after the DEER sequence with duration t_{nv} is given by

$$S = \frac{1}{2}\left[1 + \cos(k_s J_z t_{nv})\right] = \frac{1}{2}\left[1 + \cos(k_s \sigma^z t_{nv}/2)\right], \tag{D.4}$$

where $\sigma^z = \pm 1$ denotes the sign of the initial projection of the reporter spin.

We have to trace over all the reporter spin projections, and, for several reporter spins, we have to add up the contributions, resulting in

$$S = \frac{1}{2}(1 + \langle \cos \phi_1 \rangle), \tag{D.5}$$

where $\langle\rangle$ denotes averaging over many runs of the experiment (reporter spin projections), and the phase in each run is given by the sum over all reporter spins:

$$\phi_1 = \frac{t_{nv}}{2} \sum_s k_s \sigma_s^z. \tag{D.6}$$

To perform this average, we use $\langle \sigma_s^z \rangle = 0$, $\langle \sigma_s^z \sigma_{s'}^z \rangle = 0$ for $s \neq s'$, $\langle (\sigma_s^z)^2 \rangle = 1$, which yields

$$S = \frac{1}{2}\left[1 + \prod_s \cos(k_s t_{nv}/2)\right]. \tag{D.7}$$

D.3.2 Localizing the reporter spins with DEER at several magnetic field directions

In order to map the locations of the surface reporter spins, we performed DEER experiments with varying orientation of the magnetic field, using the $\cos^2\theta$ dependence of the dipole interaction. The full Hamiltonian for the system of NV spin-reporter spin coupled via the magnetic dipole interaction is given by:

$$H = \hbar \Delta S_{z'}^2 + \hbar \gamma_e \boldsymbol{B} \cdot \boldsymbol{S} + \hbar \gamma_e \boldsymbol{B} \cdot \boldsymbol{J} + \frac{\hbar^2 \gamma_e^2}{r_s^3}\left[\boldsymbol{S} \cdot \boldsymbol{J} - 3\frac{(\boldsymbol{S} \cdot \boldsymbol{r}_s)(\boldsymbol{J} \cdot \boldsymbol{r}_s)}{r_s^2}\right], \tag{D.8}$$

where $\Delta = 2\pi \times 2.87$ GHz is the zero-field splitting, and the z'-axis points along the NV center symmetry axis.

The zero-field splitting is the largest energy in the problem, therefore we can make the secular approximation, retaining only the terms that commute with $S_{z'}$. This amounts to fixing the direction of the vector $\boldsymbol{S}$ to be along the NV center symmetry axis. The next-largest energy term is the reporter-spin Zeeman energy $\hbar\gamma_e \boldsymbol{B} \cdot \boldsymbol{J}$. Once again we make the secular approximation, retaining only the terms that commute with $J_{z''}$, where z'' points along the direction of the magnetic field. This amounts to fixing the direction of the vector $\boldsymbol{J}$ to be along the static magnetic field. The magnetic dipole interaction can now be calculated for an abritrary magnetic field angle. We define the coordinate axes with the z-axis pointing normal to the diamond surface, and the x axis chosen so that the NV symmetry axis is in the x-z plane. Thus the unit vector along the NV axis is $(\sqrt{2}, 0, 1)/\sqrt{3}$. In order to map the location of the surface reporter spins, we perform DEER experiments for magnetic field $\boldsymbol{B}$ rotating in the x-y plane by angle ϕ, relative to the "aligned" direction. Thus the unit vector along the magnetic field is $(\sqrt{2}\cos\phi, \sqrt{2}\sin\phi, 1)/\sqrt{3}$. The vector from the NV to the reporter spin is $\boldsymbol{r} = (x, y, z)$, where z is the depth of the NV center, measured as described above.

We can now evaluate the terms in the dipole interaction Hamiltonian in eqn. (D.8):

$$\boldsymbol{S} \cdot \boldsymbol{J} = \frac{2\cos\phi + 1}{3} S_{z'} J_{z''}, \tag{D.9}$$

$$\boldsymbol{S} \cdot \boldsymbol{r}_s = \left(x\sqrt{\frac{2}{3}} + z\sqrt{\frac{1}{3}} \right) S_{z'}, \tag{D.10}$$

$$\boldsymbol{J} \cdot \boldsymbol{r}_s = \left(x\sqrt{\frac{2}{3}}\cos\phi + y\sqrt{\frac{2}{3}}\sin\phi + z\sqrt{\frac{1}{3}} \right) J_{z''}, \tag{D.11}$$

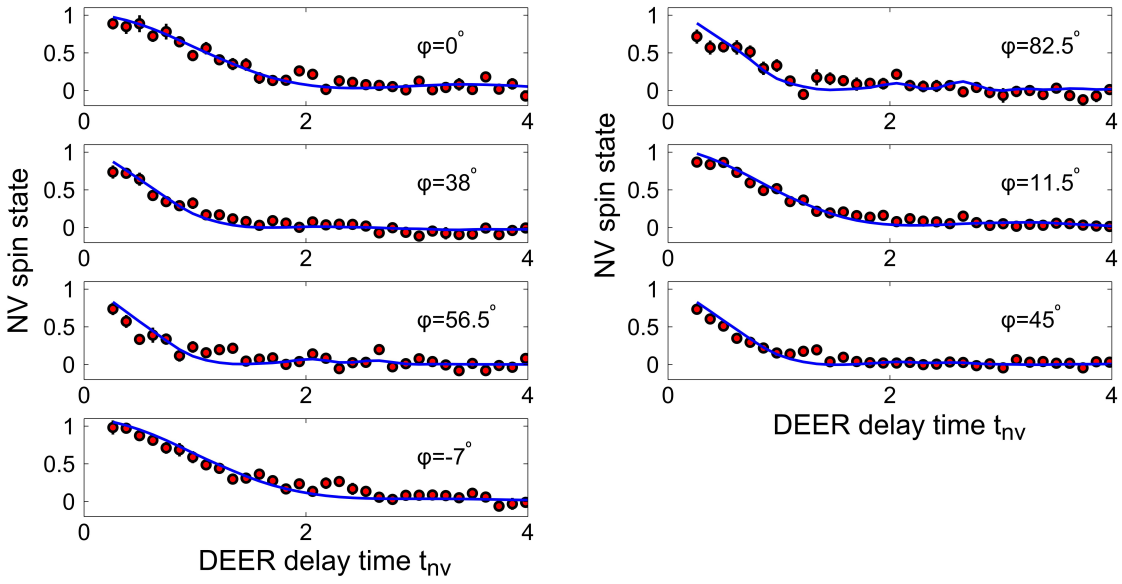

Figure D.2: DEER data taken at 7 different magnetic field angles, indicated in each plot. The magnetic field magnitude was ≈ 37 G.

and the dipole interaction Hamiltonian:

$$H_d = \frac{\hbar^2\gamma_e^2}{r_s^3}\left[\frac{2\cos\phi+1}{3} - \frac{\left(x\sqrt{2}+z\right)\left(x\sqrt{2}\cos\phi + y\sqrt{2}\sin\phi + z\right)}{x^2+y^2+z^2}\right] S_{z'}J_{z''} \quad \text{(D.12)}$$

Therefore, for a number of reporter spins located at positions (x_s, y_s) on the diamond surface, the NV center spin-state population after a DEER pulse sequence is given by eq. (D.7), with the coupling strengths

$$k_s = \frac{\hbar\gamma_e^2}{r_s^3}\left[\frac{2\cos\phi+1}{3} - \frac{\left(x_s\sqrt{2}+z\right)\left(x_s\sqrt{2}\cos\phi + y_s\sqrt{2}\sin\phi + z\right)}{x_s^2+y_s^2+z^2}\right] \quad \text{(D.13)}$$

The DEER experimental data at 7 different magnetic field angles ϕ are shown in Fig. D.2. These data were used to produce the probability density map, shown in Fig. C.1f of Appendix C, for the positions of 4 proximal reporter spins on the diamond surface near NV A.

D.3.3 Limits on the separation between surface reporter spins from their population relaxation

We can use the reporter-spin population relaxation measurements (Fig. C.2b) to confirm that the reporter spins are well separated on the diamond surface. The rate of flip-flops between neighbor spins, due to magnetic dipole interaction, is given by [128]

$$w \approx \frac{\hbar\gamma_e^2}{4s^3}\frac{1}{4}, \tag{D.14}$$

where s is the separation between them, and we approximate the angular factor, that depends of the magnetic field direction, by unity. For random reporter spin positions there is likely to be a single closest neighbor that dominates the magnetic dipole interaction. If the depth of the NV center $z \lesssim s$, then the NV center interacts the strongest with a single proximal reporter spin, and the measured population relaxation time $T_1^{(s)}$ corresponds to the time scale for a single spin flip of this proximal reporter:

$$T_1^{(s)} \approx 2\pi/w \approx 32\pi\frac{s^3}{\hbar\gamma_e^2}. \tag{D.15}$$

If the experimentally-measured $T_1^{(s)} \approx 30$ μs is caused by the magnetic dipole interaction between surface reporter spins, then their separation is $s \approx 5$ nm. If another relaxation process limits $T_1^{(s)}$, then $s > 5$ nm.

Another possibility is $z \gg s$, so that the NV center is coupled to many reporter spins. In this case we have to consider spin diffusion, and the population relaxation time $T_1^{(s)}$, as measured by the NV center, would correspond to the time scale for spin diffusion over distance $\approx z$. This can be estimated as follows. The time scale for

a single spin flip-flop is given by eq. (D.15), thus the time scale for diffusion over distance z is:

$$T_1^{(s)} \approx \frac{z^2}{s^2} 32\pi \frac{s^3}{\hbar\gamma_e^2}. \tag{D.16}$$

If the experimentally-measured $T_1^{(s)} \approx 30$ μs were caused by spin diffusion in a bath of closely-spaced reporter spins, then, from eq. (D.16), we extract their spacing to be $s \approx 10$ nm. However, for the ≈ 3.5 nm deep NV centers that we study, this is inconsistent with the assumption $z \gg s$, and we conclude that in our experiments $z \lesssim s$, and $s \gtrsim 5$ nm, as estimated above.

D.4 The reporter pulse sequence

In order to manipulate and probe the reporter spin network we use a "reporter" pulse sequence, inspired by Ramsey interferometry in atomic physics, Fig. D.3. The pulse sequence is separated into two parts: the initial state readout, and the final state readout. During the initial state readout, the phase acquired by the NV center due to the surface sensor spins is ϕ_1, and during the final state readout this phase is ϕ_2. Note that these phases flip sign during the first and second halves of the NV echos, since we apply a π-pulse to the surface sensor spins simultaneously with the π-pulse on the NV. During the period between the initial and the final readout intervals, the NV acquires a phase χ, but, if we keep this time interval longer than NV T_2^*, then $\langle\chi\rangle = \langle\sin\chi\rangle = 0$, and χ does not, on average, affect the NV population. The population readout of the NV center at the end of the pulse sequence is then given

by

$$S = \frac{1}{4}\left(2 + \cos(\phi_1 + \phi_2) - \cos(\phi_1 - \phi_2)\right) \tag{D.17}$$

$$= \frac{1}{2}\left(1 - \sin\phi_1 \sin\phi_2\right). \tag{D.18}$$

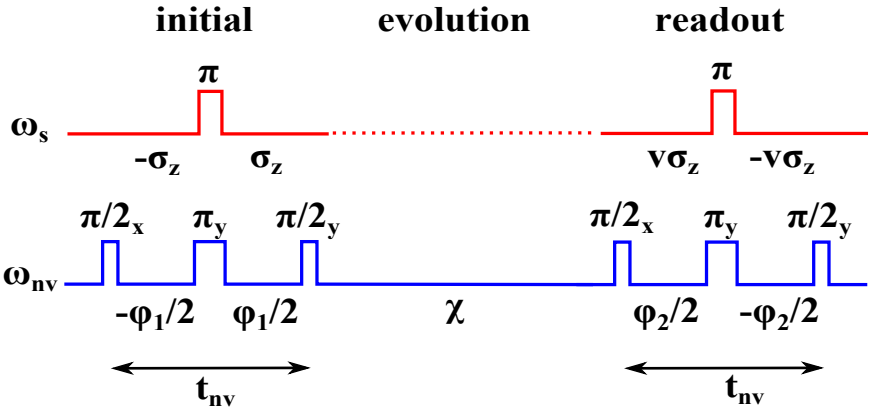

Figure D.3: Pulse sequence for NV readout of surface sensors.

Let us assume that the spin projection of a surface sensor spin s at the start of the sequence is σ_s^z, and the coupling to the NV center is k_s, as given in eq. (D.3). Then the NV phase ϕ_1 is given by the sum over all surface sensor spins:

$$\phi_1 = \frac{t_{nv}}{2}\sum_s k_s \sigma_s^z. \tag{D.19}$$

where t_{nv} is the duration of the echo.

During the surface sensor spin evolution, the projection of the surface sensor spin changes: $\sigma_s^z \to v_s^{(i)}\sigma_s^z$, where, for each run i of the experiment $v_s^{(i)} = \pm 1$ (since the spin projection can only take values $\pm 1/2$). After averaging over many experimental runs, we can average $v_s = \langle v_s^{(i)} \rangle$. For example, if we apply a π-pulse to all surface

sensor spins, all $v_s^{(i)} = -1$, and $v_s = -1$. The NV phase ϕ_2 is given by

$$\phi_2 = \frac{t_{nv}}{2} \sum_s v_s^{(i)} k_s \sigma_s^z. \tag{D.20}$$

In this way the NV readout provides information about the surface sensor spin evolution v_s. Note that we have to average the NV population signal over all projections σ_s^z of the surface spin sensors.

We perform this average by using

$$\langle \sigma_s^z \rangle = 0,\ \langle \sigma_s^z \sigma_{s'}^z \rangle = 0 \text{ for } s \neq s',\ \langle (\sigma_s^z)^2 \rangle = 1,\ v_s = \langle v_s^{(i)} \rangle, \tag{D.21}$$

to obtain

$$S = \frac{1}{2} - \frac{1}{4} \prod_s v_s \sin^2 \frac{k_s t_{nv}}{2}. \tag{D.22}$$

D.5 Sensing nuclear spins using the reporter echo sequence

D.5.1 Semiclassical spin bath

In order to measure the surface sensor coupling to proton spins, we use the pulse sequence shown in Fig. C.3a, with the surface reporter spin echo. A surface reporter spin may be strongly coupled some proximal protons, and weakly coupled to many other protons that are present on the diamond surface. We describe these weakly-coupled protons as a semiclassical spin bath, whose magnetic moment precesses at the proton Larmor frequency $\omega_n = \gamma_n B$, where $\gamma_n = g_n \mu_N / \hbar$ is the nuclear gyromagnetic ratio. The magnetic moments create a fluctuating magnetic field at the location of

the surface sensor spin, and the reporter spin echo modulation due to this fluctuating field is described by the factor

$$v_s(t_s) = \exp\left[-8(\gamma_n^2 B_n^2/\omega_n^2)\sin^4(\omega_n t_s/4)\right], \tag{D.23}$$

where B_n is the root-mean-squared amplitude of this magnetic field [56, 74, 75].

The extracted magnitude of B_n is 0.3 G, which is consistent with the magnitude of the fluctuating magnetic field created by a bath of proton spins, randomly-located on the diamond surface, with mean separation of ≈ 5.5 Å. The separation between surface OH groups for a (001)-(2×1) hydroxylated diamond surface is predicted to be approximately 2.6 Å [120], therefore our measurements are consistent with approximately 1/4 of the surface sites filled with protons.

D.5.2 Coherent hyperfine coupling to individual nuclear spins

The hyperfine interaction between a reporter electronic spin and a proton spin can be described by the Hamiltonian

$$H = a_0 \boldsymbol{J}\cdot\boldsymbol{I} + \frac{\hbar\gamma_e\gamma_n}{r_n^3}\left[\boldsymbol{J}\cdot\boldsymbol{I} - 3\frac{(\boldsymbol{J}\cdot\boldsymbol{r}_n)(\boldsymbol{I}\cdot\boldsymbol{r}_n)}{r_n^2}\right], \tag{D.24}$$

where $\boldsymbol{J}$ is the spin operator of the reporter qubit, $\boldsymbol{I}$ is the proton spin operator, r_n is the separation between the surface sensor spin and the nuclear spin, and a_0 is the contact hyperfine interaction. In the secular approximation the oscillating terms with J_x and J_y can be neglected, and the Hamiltonian reduces to $H = \hbar a J_z I_z + \hbar b J_z I_x$, where

$$a = a_0 + \frac{\hbar\gamma_e\gamma_n}{r_n^3}\left(1 - 3\cos^2\theta_n\right), \tag{D.25}$$

$$b = \frac{\hbar\gamma_e\gamma_n}{r_n^3}\left(3\cos\theta_n\sin\theta_n\right), \tag{D.26}$$

where θ_n is the angle between the vector between them and the applied magnetic field B. The spin projection of the reporter spin s, coupled to a nuclear spin n, after the echo sequence is described by the expression [117]:

$$v_{s,n}(t_s) = 1 - 2\left(\frac{b\omega_n}{\omega^+\omega^-}\right)\sin^2(\omega^+ t_s/4)\sin^2(\omega^- t_s/4), \tag{D.27}$$

where

$$\omega^{\pm} = \sqrt{(\pm a/2 - \omega_n)^2 + b^2/4}. \tag{D.28}$$

If the surface sensor is coupled to several proximal nuclear spins, as well as the weakly-coupled nuclear spin bath, then

$$v_s(t_s) = \exp\left[-8(\gamma_n^2 B_n^2/\omega_n^2)\sin^4(\omega_n t_s/4)\right]\prod_n v_{s,n}(t_s). \tag{D.29}$$

D.5.3 Fitting experimental data

In addition to the interaction with nuclear spins, the reporter spin decoherence rate Γ_s is a fitting parameter. The final expression used for fitting surface spin sensor echo modulation is:

$$v_s(t_s) = e^{-\Gamma_s t_s}\exp\left[-8(\gamma_n^2 B_n^2/\omega_n^2)\sin^4(\omega_n t_s/4)\right]\prod_n v_{s,n}(t_s), \tag{D.30}$$

where the product is over the strongly-coupled nuclear spins.

Finally, if the NV center is coupled to several surface sensor spins,

$$S = \frac{1}{2} - \frac{1}{4}\prod_s v_s \sin^2\frac{k_s t_{nv}}{2}, \tag{D.31}$$

as in eq. (D.22).

The fits shown in Fig. C.4a and C.4b were performed by first using the DEER data to extract the magnetic dipole coupling constant k_s of the NV center to the proximal reporter spin, and fitting the reporter spin echo data using eqn. (D.30), with one or two coherently-coupled protons, and a proton spin bath, see Table D.1 for relevant best-fit parameters for the fits shown Fig. C.3a and Fig. C.4a,b of Appendix C.

NV center	magnetic field	parameter	best-fit value
NV A	383 G	k_s	1.6 μs^{-1}
		Γ_s	1.3 μs^{-1}
		ω_n	10.6 μs^{-1}
		reduced χ^2	1.2
NV A	619 G	k_s	1.6 μs^{-1}
		Γ_s	1.8 μs^{-1}
		ω_n	19 μs^{-1}
		reduced χ^2	1.3
NV B	665 G	k_s	1.4 μs^{-1}
		Γ_s	1.3 μs^{-1}
		ω_n	17.1 μs^{-1}
		reduced χ^2	1.1

Table D.1: Best-fit parameters.

In order to calibrate the reporter spin state, we performed two measurements using the reporter sequence: (i) with no pulse in the evolution segment, and (ii) with a π-pulse in the evolution segment. These were taken to correspond to (i) no reporter

spin state change $\rightarrow +1$, and (ii) reporter spin flip $\rightarrow -1$. The reporter sequence measurements in this work were done in pairs, with the reporter evolution sequences differing by a reporter π-pulse. For example, the reporter echo measurement was done first with the reporter pulses $\pi/2$-π-$\pi/2$, immediately followed by a sequence $\pi/2$-π-$3\pi/2$. We confirmed that these measurements resulted in opposite final reporter spin populations.

D.6 Control experiment: acid-cleaning the diamond surface

Treatment of the diamond crystal surface with the strongly-oxidizing 3-acid mixture (equal volumes of concentrated H_2SO_4, HNO_3, and $HClO_4$) for two hours resets the locations of the surface reporter qubits (Fig. C.1e of Appendix C). We also repeated the reporter spin echo experiment on NV A after this surface treatment, see Fig. D.4. The data are clearly modified, indicating that this measurement is sensitive to the interaction between the reporter spin at a new, post-clean, location, with protons in its vicinity on the diamond surface.

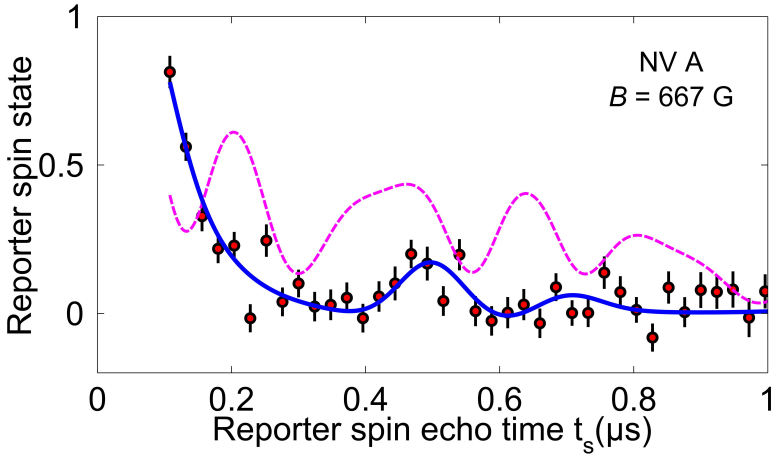

Figure D.4: The NV A reporter spin echo measurement after 3-acid surface treatment. The best-fit curve for the measurement before the surface treatment is shown as a dashed magenta line (see also Fig. C.4a of Appendix C).

Bibliography

[1] T. Kanai, M. Miyauchi, Y. Sugi, Y. Makino, and T. Maruyama. Compatible optical system for three optical disc systems (HD-DVD/DVD/CD). In *Optical Data Storage*, 2007.

[2] E. Murphy. The semiconductor laser: Enabling optical communication. *Nature Photonics*, 4:287–287, 2010.

[3] S. Mueller, B. Kruck, and P. Baudisch. LaserOrigami : Laser-Cutting 3D Objects. In *Proceedings of the SIGCHI Conference on Human Factors in Computing Systems*, pages 2585–2592, 2013.

[4] M. Ono, Y. Shinbo, A. Yoshitake, and M. Ohmura. Development of Laser-arc Hybrid Welding. *Nkk Technical Review*, 86:8–12, 2002.

[5] R. N. Wlodawsky and R. A. Strauss. Intraoral laser surgery. *Oral and Maxillofacial Surgery Clinics of North America*, 16:149–163, 2004.

[6] M. Koslin. Laser applications in temporomandibular joint arthroscopic surgery. *Oral and Maxillofacial Surgery Clinics of North America*, 16:269–275, 2004.

[7] T. Sakimoto, M. I. Rosenblatt, and D. T. Azar. Laser eye surgery for refractive errors. *Lancet*, 367:1432–1447, 2006.

[8] D. J. Wineland and W. M. Itano. Laser cooling of atoms. *Physical Review A*, 20:1521–1540, 1979.

[9] H. Goto, H. Katsuki, H. Ibrahim, H. Chiba, and K. Ohmori. Strong-laser-induced quantum interference. *Nature Physics*, 7:383–385, 2011.

[10] N. K. Logothetis. What we can do and what we cannot do with fMRI. *Nature*, 453:869–878, 2008.

[11] I. M. Ross. The invention of the transistor. *Proceedings of the IEEE*, 86:7–28, 1998.

[12] N. Gisin and R. Thew. Quantum communication. *Nature Photonics*, 1:165–171, 2007.

[13] D. P. Divincenzo. Quantum Computation. *Science*, 270:255–261, 1995.

[14] V. Giovannetti, S. Lloyd, and L. MacCone. Quantum metrology. *Physical Review Letters*, 96, 2006.

[15] W. D. Phillips, J. V. Prodan, and H. J. Metcalf. Laser cooling and electromagnetic trapping of neutral atoms. *Journal of the Optical Society of America B*, 2:1751, 1985.

[16] C. Wieman, D. Pritchard, and D. Wineland. Atom cooling, trapping, and quantum manipulation. *Reviews of Modern Physics*, 71:S253–S262, 1999.

[17] J. J. García-Ripoll, P. Zoller, and J. I. Cirac. Quantum information processing with cold atoms and trapped ions. *Journal of Physics B: Atomic, Molecular and Optical Physics*, 38:S567–S578, 2005.

[18] J. T. Barreiro, M. Müller, P. Schindler, D. Nigg, T. Monz, M. Chwalla, M. Hennrich, C. F. Roos, P. Zoller, and R. Blatt. An open-system quantum simulator with trapped ions. *Nature*, 470:486–491, 2011.

[19] R. Blatt and C. F. Roos. Quantum simulations with trapped ions. *Nature Physics*, 8:277–284, 2012.

[20] Z.-S. Yuan, X.-H. Bao, C.-Y. Lu, J. Zhang, C.-Z. Peng, and J.-W. Pan. Entangled photons and quantum communication. *Physics Reports*, 497:1–40, 2010.

[21] D. Rugar, R. Budakian, H. J. Mamin, and B. W. Chui. Single spin detection by magnetic resonance force microscopy. *Nature*, 430(6997):329–332, 2004.

[22] C. L. Degen, M. Poggio, H. J. Mamin, C. T. Rettner, and D. Rugar. Nanoscale magnetic resonance imaging. *Proceedings of the National Academy of Sciences of the United States of America*, 106:1313–1317, 2009.

[23] K. C. Nowack, E. M. Spanton, M. Baenninger, M. König, J. R. Kirtley, B. Kalisky, C. Ames, P. Leubner, C. Brüne, H. Buhmann, L. W. Molenkamp, D. Goldhaber-Gordon, and K. a. Moler. Imaging currents in HgTe quantum wells in the quantum spin Hall regime. *Nature materials*, 12:787–91, 2013.

[24] S. J. Bending. Local magnetic probes of superconductors. *Advances in Physics*, 48:449–535, 1999.

[25] J. C. Allred, R. N. Lyman, T. W. Kornack, and M. V. Romalis. High-sensitivity atomic magnetometer unaffected by spin-exchange relaxation. *Physical Review Letters*, 89:130801, 2002.

[26] M. W. Doherty, N. B. Manson, P. Delaney, F. Jelezko, J. Wrachtrup, and L. C. L. Hollenberg. The nitrogen-vacancy colour centre in diamond. *Physics Reports*, 528:1–45, 2013.

[27] M. V. G. Dutt, L. Childress, L. Jiang, E. Togan, J. Maze, F. Jelezko, A. S. Zibrov, P. R. Hemmer, and M. D. Lukin. Quantum register based on individual electronic and nuclear spin qubits in diamond. *Science*, 316:1312–1316, 2007.

[28] T. D. Ladd, F. Jelezko, R. Laflamme, Y. Nakamura, C. Monroe, and J. L. O'Brien. Quantum computers. *Nature*, 464:45–53, 2010.

[29] N. Y. Yao, L. Jiang, A. V. Gorshkov, P. C. Maurer, G. Giedke, J. I. Cirac, and M. D. Lukin. Scalable Architecture for a Room Temperature Solid-State Quantum Information Processor. *Nature Communications*, 3:15, 2010.

[30] A. Beveratos, R. Brouri, T. Gacoin, A. Villing, J.-P. Poizat, and P. Grangier. Single photon quantum cryptography. *Physical Review Letters*, 89:187901, 2002.

[31] P. C. Maurer, G. Kucsko, C. Latta, L. Jiang, N. Y. Yao, S. D. Bennett, F. Pastawski, D. Hunger, N. Chisholm, M. Markham, D. J. Twitchen, J. I. Cirac, and M. D. Lukin. Room-Temperature Quantum Bit Memory Exceeding One Second. *Science*, 336:1283–1286, 2012.

[32] J. S. Hodges, N. Y. Yao, D. Maclaurin, C. Rastogi, M. D. Lukin, and D. Englund. Timekeeping with electron spin states in diamond. *Physical Review A - Atomic, Molecular, and Optical Physics*, 87, 2013.

[33] F. Dolde, H. Fedder, M. W. Doherty, T. Nöbauer, F. Rempp, G. Balasubramanian, T. Wolf, F. Reinhard, L. C. L. Hollenberg, F. Jelezko, and J. Wrachtrup. Electric-field sensing using single diamond spins. *Nature Physics*, 7:459–463, 2011.

[34] V. M. Acosta, E. Bauch, M. P. Ledbetter, A. Waxman, L. S. Bouchard, and D. Budker. Temperature dependence of the nitrogen-vacancy magnetic resonance in diamond. *Physical Review Letters*, 104, 2010.

[35] G. Kucsko, P. C. Maurer, N. Y. Yao, M. Kubo, H. J. Noh, P. K. Lo, H. Park, and M. D. Lukin. Nanometre-scale thermometry in a living cell. *Nature*, 500:54–8, 2013.

[36] M. H. M. Devoret, A. Wallraff, and J. M. Martinis. Superconducting Qubits: A Short Review. *arXiv cond-mat/0411174*, 2004.

[37] H. Mooij. Superconducting quantum bits. *Physics World*, 17:29–33, 2004.

[38] A. Zagoskin, A. Zagoskin, A. Blais, and A. Blais. Superconducting qubits. *Physics in Canada*, 63:215–217, 2008.

[39] L. Kouwenhoven and C. Marcus. Quantum dots. *Physics World*, 11:35–39, 1998.

[40] D. Loss and D. P. DiVincenzo. Quantum computation with quantum dots. *Physical Review A*, 57:120–126, 1998.

[41] A. M. Smith and S. Nie. Next-generation quantum dots. *Nature biotechnology*, 27:732–733, 2009.

[42] J. H. N. Loubser and J. A. van Wyk. Electron spin resonance in the study of diamond. *Reports on Progress in Physics*, 41:1201, 1978.

[43] A. Gali, M. Fyta, and E. Kaxiras. Ab initio supercell calculations on nitrogen-vacancy center in diamond: Electronic structure and hyperfine tensors. *Physical Review B - Condensed Matter and Materials Physics*, 77:1–12, 2008.

[44] D. A. Redman, S. Brown, R. H. Sands, and S. C. Rand. Spin dynamics and electronic states of N-V center in diamond by EPR and four-wave-mixing spectroscopy. *Physical Review Letters*, 64:3420–3423, 1991.

[45] G. Davies and M. F. Hamer. Optical Studies of the 1.945 eV Vibronic Band in Diamond. *Proceedings of the Royal Society A: Mathematical, Physical and Engineering Sciences*, 348:285–298, 1976.

[46] L. J. Rogers, S. Armstrong, M. J. Sellars, and N. B. Manson. Infrared emission of the NV centre in diamond: Zeeman and uniaxial stress studies. *New Journal of Physics*, 10, 2008.

[47] R. Schirhagl, K. Chang, M. Loretz, and C. L. Degen. Nitrogen-vacancy centers in diamond: nanoscale sensors for physics and biology. *Annual Review of Physical Chemistry*, 65:83–105, 2014.

[48] I. I. Vlasov, V. G. Ralchenko, A. V. Khomich, S. V. Nistor, D. Shoemaker, and R. A. Khmelnitskii. Relative abundance of single and vacancy-bonded substitutional nitrogen in CVD diamond. *Physica Status Solidi (A) Applied Research*, 181:83–90, 2000.

[49] J. Meijer, B. Burchard, M. Domhan, C. Wittmann, T. Gaebel, I. Popa, F. Jelezko, and J. Wrachtrup. Generation of single color centers by focused nitrogen implantation. *Applied Physics Letters*, 87:1–3, 2005.

[50] J. F. Ziegler, M. D. Ziegler, and J. P. Biersack. SRIM - The stopping and range of ions in matter (2010). *Nuclear Instruments and Methods in Physics Research, Section B: Beam Interactions with Materials and Atoms*, 268:1818–1823, 2010.

[51] Y. Chu, N. P. De Leon, B. J. Shields, B. Hausmann, R. Evans, E. Togan, M. J. Burek, M. Markham, A. Stacey, A. S. Zibrov, A. Yacoby, D. J. Twitchen, M. Loncar, H. Park, P. Maletinsky, and M. D. Lukin. Coherent optical transitions in implanted nitrogen vacancy centers. *Nano Letters*, 14:1982–1986, 2014.

[52] F. Jelezko, T. Gaebel, I. Popa, A. Gruber, and J. Wrachtrup. Observation of coherent oscillations in a single electron spin. *Physical Review Letters*, 92:076401, 2004.

[53] F. Jelezko, T. Gaebel, I. Popa, M. Domhan, A. Gruber, and J. Wrachtrup. Observation of coherent oscillation of a single nuclear spin and realization of a two-qubit conditional quantum gate. *Physical Review Letters*, 93, 2004.

[54] N. B. Manson, J. P. Harrison, and M. J. Sellars. Nitrogen-vacancy center in diamond: Model of the electronic structure and associated dynamics. *Physical Review B - Condensed Matter and Materials Physics*, 74, 2006.

[55] A. Gruber. Scanning Confocal Optical Microscopy and Magnetic Resonance on Single Defect Centers. *Science*, 276:2012–2014, 1997.

[56] L. Childress, M. V. Gurudev Dutt, J. M. Taylor, A. S. Zibrov, F. Jelezko, J. Wrachtrup, P. R. Hemmer, and M. D. Lukin. Coherent dynamics of coupled electron and nuclear spin qubits in diamond. *Science*, 314:281–285, 2006.

[57] L. T. Hall, C. D. Hill, J. H. Cole, and L. C. L. Hollenberg. Ultrasensitive diamond magnetometry using optimal dynamic decoupling. *Physical Review B - Condensed Matter and Materials Physics*, 82, 2010.

[58] G. de Lange, Z. H. Wang, D. Ristè, V. V. Dobrovitski, and R. Hanson. Universal dynamical decoupling of a single solid-state spin from a spin bath. *Science*, 330:60–63, 2010.

[59] B. Naydenov, F. Dolde, L. T. Hall, C. Shin, H. Fedder, L. C. L. Hollenberg, F. Jelezko, and J. Wrachtrup. Dynamical Decoupling of a single electron spin at room temperature. *Physical Review B*, 83:081201, 2010.

[60] C. A. Ryan, J. S. Hodges, and D. G. Cory. Robust decoupling techniques to extend quantum coherence in diamond. *Physical Review Letters*, 105, 2010.

[61] K.-i. Matsumoto, S. Subramanian, R. Murugesan, J. B. Mitchell, and M. C. Krishna. Spatially resolved biologic information from in vivo EPRI, OMRI, and MRI. *Antioxidants & Redox Signaling*, 9(8):1125–1141, 2007.

[62] E. T. Ahrens and J. W. M. Bulte. Tracking immune cells in vivo using magnetic resonance imaging. *Nature Reviews: Immunology*, 13:755–63, 2013.

[63] N. Netzer, J. M. Goodenbour, A. David, K. A. Dittmar, R. B. Jones, J. R. Schneider, D. Boone, E. M. Eves, M. R. Rosner, J. S. Gibbs, A. Embry, B. Dolan, S. Das, H. D. Hickman, P. Berglund, J. R. Bennink, J. W. Yewdell, and T. Pan. Innate immune and chemically triggered oxidative stress modifies translational fidelity. *Nature*, 462:522–526, 2009.

[64] B. Halliwell. Oxidative stress and cancer: have we moved forward? *The Biochemical Journal*, 401:1–11, 2007.

[65] M. Valko, D. Leibfritz, J. Moncol, M. T. D. Cronin, M. Mazur, and J. Telser. Free radicals and antioxidants in normal physiological functions and human disease. *The International Journal of Biochemistry & Cell Biology*, 39:44–84, 2007.

[66] S. J. James, P. Cutler, S. Melnyk, S. Jernigan, L. Janak, D. W. Gaylor, and J. A. Neubrander. Metabolic biomarkers of increased oxidative stress and impaired methylation capacity in children with autism. *American Journal of Clinical Nutrition*, 80:1611–1617, 2004.

[67] A. Blank, C. R. Dunnam, P. P. Borbat, and J. H. Freed. Pulsed three-dimensional electron spin resonance microscopy. *Applied Physics Letters*, 85:5430–5432, 2004.

[68] J. M. Taylor, P. Cappellaro, L. Childress, L. Jiang, D. Budker, P. R. Hemmer, A. Yacoby, R. Walsworth, and M. D. Lukin. High-sensitivity diamond magnetometer with nanoscale resolution. *Nature Physics*, 4(10):810–816, September 2008.

[69] J. R. Maze, P. L. Stanwix, J. S. Hodges, S. Hong, J. M. Taylor, P. Cappellaro, L. Jiang, M. V. G. Dutt, E. Togan, A. S. Zibrov, A. Yacoby, R. L. Walsworth, and M. D. Lukin. Nanoscale magnetic sensing with an individual electronic spin in diamond. *Nature*, 455(7213):644–7, October 2008.

[70] G. Balasubramanian, I. Y. Chan, R. Kolesov, M. Al-Hmoud, J. Tisler, C. Shin, C. Kim, A. Wojcik, P. R. Hemmer, A. Krueger, T. Hanke, A. Leitenstorfer, R. Bratschitsch, F. Jelezko, and J. Wrachtrup. Nanoscale imaging magnetometry with diamond spins under ambient conditions. *Nature*, 455(7213):648–651, October 2008.

[71] S. Steinert, F. Ziem, L. T. Hall, A. Zappe, M. Schweikert, N. Götz, A. Aird, G. Balasubramanian, L. Hollenberg, and J. Wrachtrup. Magnetic spin imaging

under ambient conditions with sub-cellular resolution. *Nature Communications*, 4:1607, 2013.

[72] J. P. Tetienne, T. Hingant, L. Rondin, A. Cavaillès, L. Mayer, G. Dantelle, T. Gacoin, J. Wrachtrup, J. F. Roch, and V. Jacques. Spin relaxometry of single nitrogen-vacancy defects in diamond nanocrystals for magnetic noise sensing. *Physical Review B - Condensed Matter and Materials Physics*, 87, 2013.

[73] S. Kaufmann, D. A. Simpson, L. T. Hall, V. Perunicic, P. Senn, S. Steinert, L. P. McGuinness, B. C. Johnson, T. Ohshima, F. Caruso, J. Wrachtrup, R. E. Scholten, P. Mulvaney, and L. Hollenberg. Detection of atomic spin labels in a lipid bilayer using a single-spin nanodiamond probe. *Proceedings of the National Academy of Sciences of the United States of America*, 110(27):10894–8, 2013.

[74] T. Staudacher, F. Shi, S. Pezzagna, J. Meijer, J. Du, C. a. Meriles, F. Reinhard, and J. Wrachtrup. Nuclear magnetic resonance spectroscopy on a (5-nanometer)3 sample volume. *Science*, 339:561–3, 2013.

[75] H. J. Mamin, M. Kim, M. H. Sherwood, C. T. Rettner, K. Ohno, D. D. Awschalom, and D. Rugar. Nanoscale nuclear magnetic resonance with a nitrogen-vacancy spin sensor. *Science*, 339:557–60, 2013.

[76] R. W. Bierig, M. J. Weber, and S. I. Warshaw. Paramagnetic resonance and relaxation of trivalent rare-earth ions in calcium fluoride. II. Spin-lattice relaxation. *Physical Review*, 134, 1964.

[77] H. K. Kim, G. H. Lee, T. J. Kim, and Y. Chang. Determination of correlation times of new paramagnetic gadolinium MR contrast agents by EPR and 17O NMR. *Bulletin of the Korean Chemical Society*, 30(4):849–852, 2009.

[78] L. T. Hall, C. D. Hill, J. H. Cole, B. Städler, F. Caruso, P. Mulvaney, J. Wrachtrup, and L. C. L. Hollenberg. Monitoring ion-channel function in real time through quantum decoherence. *Proceedings of the National Academy of Sciences of the United States of America*, 107:18777–18782, 2010.

[79] V. S. Perunicic, L. T. Hall, D. A. Simpson, C. D. Hill, and L. C. L. Hollenberg. Towards single-molecule NMR detection and spectroscopy using single spins in diamond. *Physical Review B - Condensed Matter and Materials Physics*, 89, 2014.

[80] B. N. G. Giepmans, S. R. Adams, M. H. Ellisman, and R. Y. Tsien. The fluorescent toolbox for assessing protein location and function. *Science*, 312:217–224, 2006.

[81] D. Le Sage, K. Arai, D. R. Glenn, S. J. DeVience, L. M. Pham, L. Rahn-Lee, M. D. Lukin, A. Yacoby, A. Komeili, and R. L. Walsworth. Optical magnetic imaging of living cells. *Nature*, 496(7446):486–489, April 2013.

[82] M. S. Grinolds, S. Hong, P. Maletinsky, L. Luan, M. D. Lukin, R. L. Walsworth, and A. Yacoby. Nanoscale magnetic imaging of a single electron spin under ambient conditions. *Nature Physics*, 9:215–219, 2013.

[83] J. R. Kirtley. Fundamental studies of superconductors using scanning magnetic imaging. *Reports on Progress in Physics*, 73(126501):59, 2010.

[84] H. Zhang, C.-X. Liu, X.-L. Qi, X. Dai, Z. Fang, and S.-C. Zhang. Topological insulators in Bi2Se3, Bi2Te3 and Sb2Te3 with a single Dirac cone on the surface. *Nature Physics*, 5:438–442, 2009.

[85] E. Bordignon and H.-J. Steinhoff. Membrane Protein Structure and Dynamics Studied by Site-Directed Spin-Labeling ESR. *Biomedical Magnetic Resonance*, 27:129, 2007.

[86] A. O. Sushkov, I. Lovchinsky, N. Chisholm, R. L. Walsworth, H. Park, and M. D. Lukin. Magnetic Resonance Detection of Individual Proton Spins Using Quantum Reporters. *Physical Review Letters*, 113:197601, 2014.

[87] F. C. Ziem, N. S. Götz, A. Zappe, S. Steinert, and J. Wrachtrup. Highly sensitive detection of physiological spins in a microfluidic device. *Nano Letters*, 13(9):4093–4098, 2013.

[88] L. P. McGuinness, Y. Yan, A. Stacey, D. A. Simpson, L. T. Hall, D. Maclaurin, S. Prawer, P. Mulvaney, J. Wrachtrup, F. Caruso, R. E. Scholten, and L. C. L. Hollenberg. Quantum measurement and orientation tracking of fluorescent nanodiamonds inside living cells. *Nature Nanotechnology*, 6:358–363, 2011.

[89] M. E. Trusheim, L. Li, A. Laraoui, E. H. Chen, H. Bakhru, T. Schröder, O. Gaathon, C. A. Meriles, and D. Englund. Scalable fabrication of high purity diamond nanocrystals with long-spin-coherence nitrogen vacancy centers. *Nano Letters*, 14(1):32–36, 2014.

[90] A. O. Sushkov, N. Chisholm, I. Lovchinsky, M. Kubo, P. K. Lo, S. D. Bennett, D. Hunger, A. Akimov, R. L. Walsworth, H. Park, and M. D. Lukin. All-optical sensing of a single-molecule electron spin. *Nano Letters*, 2014.

[91] L. Rondin, J. P. Tetienne, P. Spinicelli, C. Dal Savio, K. Karrai, G. Dantelle, A. Thiaville, S. Rohart, J. F. Roch, and V. Jacques. Nanoscale magnetic field mapping with a single spin scanning probe magnetometer. *Applied Physics Letters*, 100, 2012.

[92] T. Hattori, Y. Ihara, Y. Nakai, K. Ishida, Y. Tada, S. Fujimoto, N. Kawakami, E. Osaki, K. Deguchi, N. K. Sato, and I. Satoh. Superconductivity induced by longitudinal ferromagnetic fluctuations in UCoGe. *Physical Review Letters*, 108:1–5, 2012.

[93] L. Chotorlishvili, A. Ernst, V. K. Dugaev, A. Komnik, M. G. Vergniory, E. V. Chulkov, and J. Berakdar. Magnetic fluctuations in topological insulators with ordered magnetic adatoms: Cr on Bi 2 Se 3 from first principles. *Physical Review B - Condensed Matter and Materials Physics*, 89:1–6, 2014.

[94] A. Laraoui, J. S. Hodges, and C. a. Meriles. Magnetometry of random ac magnetic fields using a single nitrogen-vacancy center. *Applied Physics Letters*, 97:2008–2011, 2010.

[95] G. Balasubramanian, P. Neumann, D. Twitchen, M. Markham, R. Kolesov, N. Mizuochi, J. Isoya, J. Achard, J. Beck, J. Tissler, V. Jacques, P. R. Hemmer, F. Jelezko, and J. Wrachtrup. Ultralong spin coherence time in isotopically engineered diamond. *Nature Materials*, 8(5):383–387, May 2009.

[96] I. Lovchinsky, A. O. Sushkov, E. Urbach, N. de Leon, K. De Greve, R. Evans, E. Bersin, F. Jelezko, R. L. Walsworth, H. Park, and M. D. Lukin. Nuclear Magnetic Resonance Detection and Spectroscopy of Single Proteins using Quantum Logic. *submitted to Nature*, 2015.

[97] J. Henig, I. Mamedov, P. Fouskova, E. Tóth, N. K. Logothetis, G. Angelovski, and H. A. Mayer. Influence of calcium-induced aggregation on the sensitivity of aminobis(methylenephosphonate)-containing potential MRI contrast agents. *Inorganic Chemistry*, 50(14):6472–6481, 2011.

[98] P. E. Pehrsson and T. W. Mercer. Oxidation of heated diamond C(100):H surfaces. *Surface Science*, 460(1-3):74–90, 2000.

[99] P. Strobel, J. Ristein, and L. Ley. Controlled hydroxylation of diamond for covalent attachment of fullerene molecules. *Diamond and Related Materials*, 17(7-10):1362–1366, 2008.

[100] R. Masel. *Principles of Adsorption and Reaction on Solid Surfaces*. Wiley, 1996.

[101] A. A. Clerk, S. M. Girvin, F. Marquardt, and R. J. Schoelkopf. Introduction to quantum noise, measurement, and amplification. *Reviews of Modern Physics*, 82(2):1155–1208, 2010.

[102] E. D. Feigelson and G. J. Babu. *Modern Statistical Methods for Astronomy: With R Applications*. Cambridge University Press, 2012.

[103] J. A. Peacock. Two-dimensional goodness-of-fit testing in astronomy. *Monthly Notices of the Royal Astronomical Society*, 202, 1983.

[104] N. N. Jarenwattananon, S. Glöggler, T. Otto, A. Melkonian, W. Morris, S. R. Burt, O. M. Yaghi, and L.-S. Bouchard. Thermal maps of gases in heterogeneous reactions. *Nature*, 502(7472):537–40, 2013.

[105] R. Ernst, G. Bodenhausen, and A. Wokaun. *Principles of Nuclear Magnetic Resonance in One and Two Dimensions*. Oxford University Press, 1987.

[106] D. Sakellariou, G. Le Goff, and J.-F. Jacquinot. High-resolution, high-sensitivity NMR of nanolitre anisotropic samples by coil spinning. *Nature*, 447:694–697, 2007.

[107] M. Schaffry, E. M. Gauger, J. J. L. Morton, and S. C. Benjamin. Proposed spin amplification for magnetic sensors employing crystal defects. *Physical Review Letters*, 107, 2011.

[108] B. Grotz, J. Beck, P. Neumann, B. Naydenov, R. Reuter, F. Reinhard, F. Jelezko, J. Wrachtrup, D. Schweinfurth, B. Sarkar, and P. Hemmer. Sensing external spins with nitrogen-vacancy diamond. *New Journal of Physics*, 13(5):055004, 2011.

[109] M. S. Grinolds, M. Warner, K. De Greve, Y. Dovzhenko, L. Thiel, R. L. Walsworth, S. Hong, P. Maletinsky, and A. Yacoby. Subnanometre resolution in three-dimensional magnetic resonance imaging of individual dark spins. *Nature Nanotechnology*, 9:279–284, 2014.

[110] B. A. Myers, A. Das, M. C. Dartiailh, K. Ohno, D. D. Awschalom, and A. C. Bleszynski Jayich. Probing surface noise with depth-calibrated spins in diamond. *Physical Review Letters*, 113, 2014.

[111] T. Rosskopf, A. Dussaux, K. Ohashi, M. Loretz, R. Schirhagl, H. Watanabe, S. Shikata, K. M. Itoh, and C. L. Degen. Investigation of surface magnetic noise by shallow spins in diamond. *Physical Review Letters*, 112, 2014.

[112] H. R. Herschman. Molecular imaging: looking at problems, seeing solutions. *Science*, 302:605–608, 2003.

[113] M. Scanziani and M. Häusser. Electrophysiology in the age of light. *Nature*, 461:930–939, 2009.

[114] P. Neumann, R. Kolesov, B. Naydenov, J. Beck, F. Rempp, M. Steiner, V. Jacques, G. Balasubramanian, M. L. Markham, D. J. Twitchen, S. Pezzagna, J. Meijer, J. Twamley, F. Jelezko, and J. Wrachtrup. Quantum register

based on coupled electron spins in a room-temperature solid. *Nature Physics*, 6(4):249–253, 2010.

[115] N. F. Ramsey. A molecular beam resonance method with separated oscillating fields. *Physical Review*, 78:695–699, 1950.

[116] A. Laraoui, F. Dolde, C. Burk, F. Reinhard, J. Wrachtrup, and C. A. Meriles. High-resolution correlation spectroscopy of 13C spins near a nitrogen-vacancy centre in diamond. *Nature Communications*, 4:1651, 2013.

[117] L. Rowan, E. Hahn, and W. Mims. Electron-Spin-Echo Envelope Modulation. *Physical Review*, 137:A61–A71, 1965.

[118] M. J. Rao and R. S. Anderson. Electron Spin Resonance in Gamma-Irradiated Single Crystals of Hydroxylated Organic Compounds. *The Journal of Chemical Physics*, 42:2899, 1965.

[119] V. N. Mochalin, O. Shenderova, D. Ho, and Y. Gogotsi. The properties and applications of nanodiamonds, 2011.

[120] S. J. Sque, R. Jones, and P. R. Briddon. Structure, electronics, and interaction of hydrogen and oxygen on diamond surfaces. *Physical Review B - Condensed Matter and Materials Physics*, 73, 2006.

[121] H.-J. Wang, C. S. Shin, S. J. Seltzer, C. E. Avalos, A. Pines, and V. S. Bajaj. Optically detected cross-relaxation spectroscopy of electron spins in diamond. *Nature Communications*, 5:4135, 2014.

[122] S. J. DeVience, L. M. Pham, I. Lovchinsky, A. O. Sushkov, N. Bar-Gill, C. Belthangady, F. Casola, M. Corbett, H. Zhang, M. Lukin, H. Park, A. Yacoby, and R. L. Walsworth. Nanoscale NMR spectroscopy and imaging of multiple nuclear species. *Nature Nanotechnology*, 10(2):129–134, 2015.

[123] C. Müller, X. Kong, J.-M. Cai, K. Melentijević, a. Stacey, M. Markham, D. Twitchen, J. Isoya, S. Pezzagna, J. Meijer, J. F. Du, M. B. Plenio, B. Naydenov, L. P. McGuinness, and F. Jelezko. Nuclear magnetic resonance spectroscopy with single spin sensitivity. *Nature Communications*, 5:4703, 2014.

[124] C. Belthangady, N. Bar-Gill, L. M. Pham, K. Arai, D. Le Sage, P. Cappellaro, and R. L. Walsworth. Dressed-state resonant coupling between bright and dark spins in diamond. *Physical Review Letters*, 110, 2013.

[125] G. Goldstein, P. Cappellaro, J. R. Maze, J. S. Hodges, L. Jiang, A. S. Sø rensen, and M. D. Lukin. Environment-assisted precision measurement. *Physical Review Letters*, 106, 2011.

[126] J. Cai, A. Retzker, F. Jelezko, and M. B. Plenio. A large-scale quantum simulator on a diamond surface at room temperature. *Nature Physics*, 9(3):1–6, 2013.

[127] L. M. Pham, S. J. DeVience, F. Casola, I. Lovchinsky, A. O. Sushkov, E. Bersin, E. Urbach, J. Lee, P. Cappellaro, H. Park, A. Yacoby, M. D. Lukin, and R. L. Walsworth. Technique for Measuring Depth of Shallow Nitrogen-Vacancy Centers in Diamond. *in preparation*, 2015.

[128] A. Abragam. *The Principles of Nuclear Magnetism.* Oxford University Press, 1961.